TRENDS IN SCIENCES 2026; 23(4): 11805
https://doi.org/10.48048/tis.2026.11805 REVIEW ARTICLE

Recent Advancements in Metal Ferrite Hybrid Photocatalysts for Wastewater Treatment

Yogesh Kumar[1], Vidushi Karol[2], Abhishek Awasthi[3], Anshu Sharma[1,*], Vineet Kumar[4] and Kulvinder Singh[5]

[1]Department of Physics, School of Basic and Applied Sciences, Maharaja Agrasen University, Himachal Pradesh 174103, India
[2]Department of Physics, Department of Applied Sciences, Chandigarh Engineering College, Punjab, India
[3]Department of Biotechnology, School of Basic and Applied Sciences, Maharaja Agrasen University, Baddi 174103, India
[4]Department of Biotechnology, School of Bioengineering and Biosciences, Lovely Professional University, Punjab India
[5]Department of Chemistry, DAV College, Chandigarh 160011, India

([*]Corresponding author's e-mail: anshu.hpu@gmail.com)

Received: 6 September 2025, Revised: 23 October 2025, Accepted: 1 November 2025, Published: 25 December 2025

Abstract

Environmental pollution, especially water contamination, presents significant challenges to ecosystems, public health, and sustainability. Ferrite-based nanomaterials, specifically hybrids combining ferrites with several materials, have emerged as promising photocatalysts for wastewater treatment. These hybrids leverage ferrites' unique structural, optical, and magnetic properties while addressing challenges such as electron-hole recombination, limited visible light absorption, and agglomeration. Recent advancements in synthesis techniques, including sol-gel, co-precipitation, and green methods, have enabled precise control over ferrite hybrid properties, enhancing photocatalytic efficiency and scalability. The integration of ferrites introduces synergistic effects, such as enhanced charge carrier separation, expanded light absorption into the visible spectrum, and enhanced surface area. Innovations like doping, plasmonic enhancement, and Z-scheme heterojunctions have further optimized these materials for efficient pollutant degradation. Studies have demonstrated their potential to degrade dyes, pharmaceuticals, and other emerging contaminants under visible and solar light. Despite their promise, challenges remain in understanding the mechanisms of charge transfer, optimizing synthesis for large-scale production, and ensuring stability in real wastewater conditions. This review highlights the transformative potential of ferrite-based hybrids as scalable, cost-effective, and environmentally friendly solutions for advanced wastewater treatment. Their development marks a crucial step toward mitigating water pollution and achieving global water sustainability goals.

Keywords: Photocatalysis, Wastewater treatment, Metal ferrites, Hybrids, Environmental application

Introduction

Environmental pollution is a pressing concern in contemporary discourse, holding profound implications for ecosystems, public health, and global sustainability [1,2]. Within this intricate landscape, water pollution surfaces as a critical issue exacerbated by the substantial volume of wastewater generated from diverse sources, including domestic, commercial, and industrial activities. This wastewater carries dissolved and suspended matter, including chemicals, soaps, and heavy metals [3]. Particularly, industrial wastewater, with its high pollutant load, poses a significant threat by contaminating water resources, risking human health, and negatively impacting ecosystems [4-7]. The gravity

of the issue is underscored by poor water quality being responsible for many diseases, with over 80% of global diseases linked to contaminated water [8,9]. Additionally, the global water crisis is further intensified by the discharge of untreated wastewater from various sources, including kitchens, bathrooms, toilets, industrial effluents, and agricultural runoff [10]. The UN Environment Programme analysis transforms the narrative by redefining wastewater as a transformative solution, emphasizing its potential for sustainable wastewater management and endorsing a circular economy approach. If strategically managed, wastewater has the capacity to provide alternative energy to half a billion people, exceed global desalination capacity tenfold, and offset more than 10% of global fertilizer use [11,12]. However, with only 11% of treated wastewater currently reused globally, there exists an urgent need to harness the potential of wastewater for clean water, sustainable energy, and nutrient resources, envisioning a pivotal solution to global climate challenges and water insecurity [13].

The treatment of industrial wastewater poses several challenges. Industrial wastewater is more complex than domestic sewage and contains numerous organic and inorganic pollutants, making it difficult to meet stringent discharge standards and water reclamation requirements [14]. Industrial wastewater treatment techniques include adsorption, advanced oxidation processes (AOPs), coagulation and flocculation, biological treatment, membrane filtration, precipitation, ion exchange, and dissolved air flotation (DAF) [15-19]. Adsorption is a promising technique for wastewater treatment, but it can lead to major sludge generation and high costs for certain adsorbents [20,21]. Other challenges with adsorption techniques are Low efficiency due to partial adsorbent utilization, challenges in chemical regenerant disposal during bed regeneration [22], issues of low separation efficiency, high operational costs and extended treatment hours in conventional approaches for oily wastewater. Conventional biological treatment technologies alone are often inadequate for meeting these standards [23]. Additionally, there is a risk of secondary pollutant generation associated with various wastewater treatment techniques [24]. However, Researchers are employing diverse strategies to overcome limitations of various methods and optimize wastewater treatment plants for maximum efficiency and sustainability. AOPs offer several advantages over traditional methods for industrial wastewater treatment. AOPs utilize reactive free radical species to degrade persistent compounds and minimize toxicity [25]. These mechanisms, combined with hydrodynamic cavitation, ultrasound, and sono-electrochemical oxidation, result in hybrid AOPs with significant oxidative capacities [26]. AOPs are effective at removing a variety of pollutants, including refractory organic compounds, micropollutants, and color and odor components [27]. They can also achieve high removal percentages, such as 98.43% for oil from oily wastewater [28].

Photocatalysis, a promising advanced oxidation process (AOP), utilizes photocatalysts to expedite light-induced chemical reactions, providing a cost-effective, versatile, and environmentally friendly approach for mitigating diverse harmful pollutants in both air and water [29]. Photocatalysis can effectively remove emerging pollutants like pharmaceuticals [30,31], pesticides [32,33] and organic compounds [34-36] from industrial and municipal wastewater using visible, UV radiation, and solar light. A variety of photoreactors, such as slurry, membrane, annular, closed-loop step, rotating-drum, and micro photoreactors, have been constructed and used for wastewater treatment [37]. These reactors have used heterogeneous, homogeneous, and mixed photocatalyst systems to accomplish effective photocatalysis [38]. Photocatalysis operates at ambient temperatures and pressures, reducing the requirements for reaction facilities and operating costs [39]. However, despite its advantages, photocatalysis for wastewater treatment faces several challenges depending upon the type of photocatalyst used. Metal oxides, such as TiO_2, which is the most studied photocatalyst, have large band gaps ($\geq$ 3 eV), which restricts their absorption of visible light and limits their photocatalytic activity under sunlight, resulting in limited applicability due to the expense of producing ultraviolet light [40]. Photo corrosion of metal oxide-based photocatalysts is also a significant challenge in their practical use. TiO_2, Cu_2O, and ZnO have been found to exhibit increased corrosion rates under illumination, leading to degradation of their performance [41,42]. In the visible light regime, metal chalcogenides like MoS_2, ZnS, CdS, etc. have better solar spectral response due to their narrow band gap.

However, Metal chalcogenides, while possessing diverse architectures and narrow band gaps, face several drawbacks in photocatalysis. These include limited synthesis methods, low degradation efficiency, rapid recombination of charge carriers, difficulty in separation and recovery from the reaction mixture, and poor chemical stability leading to the photo corrosion process, and reduced efficiency in pollutant removal [43-46].

Ferric oxide nanotechnology is the manipulation of nanoscale materials to produce certain properties and functionalities, which allow them to be used in a variety of applications [47]. Nanoparticles, which range in size from 1 to 100 nm, have distinct features in terms of form, magnetic, structure, electrical conductivity, catalytic activity, mechanical strength, optical scattering, and physicochemical properties [48-50]. The term "magnetic nanoparticles" encompasses a broad spectrum of nanoscale materials that benefit from magnetic properties, making them versatile for diverse applications. This category includes metallic, bimetallic, and metal oxide nanoparticles, as well as core-shell and Janus-type structures in different configurations [51,52]. Magnetic nanoparticles can be synthesized using various transition metals such as nickel (Ni), iron (Fe), and cobalt (Co), along with their respective compounds. Notably, iron exhibits multiple valence states, ranging from 0 to +3. Haematite (α-Fe_2O_3) is a popular material due to its abundance, low cost, and high photo-stability, making it suitable for many applications [53]. Iron oxides come in several forms, such as maghemite (γ-Fe_2O_3), goethite (FeO(OH)), haematite (α-Fe_2O_3), and magnetite. Haematite (α-Fe_2O_3) has the highest thermodynamic stability when exposed to oxygen. Due to their core-shell structure, iron oxide nanoparticles (IONPs) have characteristics that are similar to both hydrous iron oxides and metallic iron [54,55]. Because of these characteristics, IONPs are positioned as prospective enzyme mimics for a range of uses. Iron oxide systems' special properties have been extensively studied for applications in biology and technology [56]. IONPs are positioned as prospective enzyme mimics for a range of applications due to their characteristics. Numerous studies have been conducted on the special properties of iron oxide systems for applications in biology and technology [56]. Iron (III) oxides have different magnetic properties from their bulk equivalents, particularly as particle size decreases, due to nanoscale confinement and surface effects. Among the many benefits of magnetic IONPs are their high level of physical and chemical stability, biocompatibility, and affordability [55]. In the nanoscale range, the quantum effect significantly influences their magnetic, electrical, and optical behaviors. Notably, Fe_3O_4 and γ-Fe_2O_3 nanoparticles exhibit superparamagnetic properties at sizes around 10 - 20 nm, enhancing their performance in various applications. Their high surface-to-volume ratio also improves dispersibility in solutions, making them highly suitable for practical applications. Metal nano ferrites have emerged as promising photocatalysts for industrial wastewater treatment [57-61]. The band gap energies of these ferrite nanoparticles range from 2.80 to 3.5 eV, indicating their potential for visible light photocatalysis. These ferrites exhibit unique physical and chemical characteristics that make them effective in eliminating pollutants from wastewater. Their tunable band gaps, surface areas, and magnetic properties enable efficient photodegradation of organic pollutants. The high stability and magnetization of ferrites allow for easy separation and recovery of the photocatalysts from the treated water [62,63] Moreover, enhanced electrical conductivity in transition metal ferrites arises from efficient electron hopping between distinct metal valence states at oxygen sites, facilitating the transfer of charge carriers [64,65]. Owing to their Abundant availability, affordability, ease of synthesis, and excellent biocompatibility, metal nano ferrites have a huge potential for wastewater treatment. This investigation delves into an extensive examination of diverse metal ferrites and hybrid nanostructures based on metal ferrites, assessing their potential for advanced photocatalytic applications in wastewater treatment [66].

The elimination of both organic and inorganic contaminants from wastewater is the main topic of this review. Recent studies on wastewater treatment [67-70], have been published by our research group, with a focus on the application of ferrite materials in this field. With an emphasis on recent developments in their synthesis and the related difficulties, the review will investigate the efficacy of spinel ferrite-derived nanomaterials as proficient photocatalysts for the remediation of wastewater [71-75]. This analysis will explore the latest developments in doped, binary and ternary spinel ferrite

nanocomposites, alongside their enhanced properties and photocatalytic applications when integrated with advanced materials such as TiO_2, MXene, and g-C_3N_4. Based on their magnetic coercivity, ferrite materials can be broadly divided into 2 groups: Soft ferrites, which have low coercivity, and hard ferrites, which have high coercivity. Furthermore, ferrites are categorized into spinel, garnet, hexagonal, and orthoferrite based on their crystal forms [71,72]. Among these, spinel ferrites are the most common, with the general chemical formula MFe_2O_4, where M represents a divalent metal (such as Co, Cu, Ni, Zn, etc.), and the structure consists of iron and oxygen in tetrahedral and octahedral coordination sites [73]. With 56 atoms - 32 oxygen anions, 16 trivalent metal cations, and 8 divalent metal cations - the spinel ferrite takes on a face-centred cubic (FCC) lattice. In this configuration, Fe^{3+} and M^{2+} ions are positioned within interstitial sites, with Fe^{3+} occupying octahedral sites and M^{2+} residing in tetrahedral sites, while the oxygen anions are systematically arranged in a cubic close-packed structure [74,75]. The spinel ferrite structure's physical and chemical characteristics are largely determined by the distribution of M^{2+} and Fe^{3+} ions within it. The qualities of the material are impacted by the cations' random distribution between the 2 locations in a mixed spinel structure. The final characteristics of the ferrites can also be greatly influenced by the synthesis circumstances, including reaction temperature, pH, and calcination procedure [76].

The straightforward synthesis process, cost-effectiveness, elevated electrical resistivity, limited bandgap energy, magnetic permeability, substantial charge transfer capability, non-toxic nature, recyclability, as well as exceptional thermal and chemical resilience represent merely a selection of the prominent properties associated with spinel ferrites [77,78]. Because of these characteristics, ferrites can be used in a wide range of applications, including gas sensors, medication delivery, electronic devices, biomedical devices, information storage, mobile communication, water splitting, water treatment, and catalysis. Their narrow bandgap (1.5 - 2 eV) allows them to serve as effective photocatalysts under visible light, which is particularly useful for environmental remediation applications, including wastewater treatment. Spinel ferrites exhibit significant promise for the photocatalytic destruction of organic contaminants in wastewater treatment. Because of their tiny bandgaps, visible light can be used efficiently, which helps pollutants mineralize into innocuous byproducts like CO_2 and H_2O. This method reduces waste generation compared to traditional treatment techniques. Additionally, the magnetic properties of spinel ferrites make it easier to separate them from the reaction mixture after the degradation process, thus allowing for easy reuse in continuous catalytic cycles. Numerous approaches have been investigated to improve spinel ferrites' photocatalytic activity. These include the creation of mixed ferrites, doped ferrites, hybrid heterojunctions, and nanocomposites based on ferrite [79-84]. For example, the photocatalytic degradation of azo dyes under sunlight has been examined for Co-Ni mixed ferrite ($Co_{0.5}Ni_{0.5}Fe_2O_4$). Electrons are excited by light absorption, creating electron-hole (e-h) pairs that take part in redox reactions and release reactive radicals (such O_2^-•) that break down the dye [85]. Additionally, doping Co-Ni mixed ferrite with Ce has been shown to lower its bandgap, enhancing its visible light absorption and improving photocatalytic efficiency by reducing electron-hole recombination [86].

Another strategy involves hybrid organic-inorganic nanomaterials. For example, Nd-doped Rhodamine B (RhB) has been photo catalytically degraded using $NiFeO_4$ in conjunction with carbon nanotubes (CNTs). In this system, electrons in the Nd-$NiFeO_4$/CNTs composite are excited by light irradiation from the valence band (VB) to the conduction band (CB). While the holes oxidize OH^- to OH• radicals, these excited electrons convert O_2 to O_2^-• radicals. CNTs' enormous surface area aids in these redox processes during photocatalysis, which causes pollutants to degrade [86]. Furthermore, the creation of ferrite nanocomposites has been shown to improve photocatalytic activity. For instance, a $CuFe_2O_4/Bi_2O_3$ nanocomposite demonstrated enhanced photocatalytic performance for methyl blue (MB) removal compared to pure $CuFe_2O_4$. By adding BiO_3, the material's specific surface area is increased, aggregation is decreased, and light absorption is enhanced, all of which lead to more effective electron-hole pair separation [79,87]. The spinel ferrites hold significant promise for wastewater treatment, particularly in photocatalytic applications. Their ability to effectively decompose organic

contaminants in the presence of visible light, along with their magnetic characteristics, makes them a compelling and sustainable alternative for environmental remediation.

Scope of review

Magnetic nanoparticles have drawn a lot of interest because of their special qualities and possible uses in the separation and removal of environmental contaminants. Among them, ferrites are particularly promising as photocatalysts, with band gap ranging from 1.1 to 2.3 eV, allowing them to absorb visible light. Spinel ferrites offer the advantage of easy magnetic separation, making them ideal for reuse. Their crystal structure, low bandgap, excellent electrical and magnetic properties, and high chemical and thermal stability position them as top contenders in photocatalytic applications. Developed in the last few decades, photocatalysis has many uses, such as the production of coating materials, the removal of heavy metal ions, wastewater treatment, and the degradation of volatile organic compounds. It plays a crucial role in addressing microbial contamination as the global demand for freshwater increases. Various homogeneous and heterogeneous photocatalytic systems have been developed for wastewater treatment, offering cost-effective solutions that operate at ambient conditions. This review aims to present a comprehensive and critical analysis of ferrite-based photocatalysts and their hybridization with advanced functional materials such as ZnO, TiO_2, MXene, and g-C_3N_4 for environmental remediation applications, particularly the degradation of organic contaminants in wastewater. The discussion encompasses both the fundamental mechanisms and practical performance of these composite systems, drawing on recent advances in materials science and photocatalysis. The key focus areas include how the integration of ferrites with semiconductors and conductive materials influences charge separation efficiency, electron transport, and recombination dynamics, which are central to enhancing photocatalytic activity. The review assesses the optical characteristics of these composites, particularly bandgap engineering and light absorption behavior, supported by UV-Vis. spectroscopy data from recent literature. Additionally, the recyclability and operational stability of these catalysts across multiple degradation cycles are evaluated to determine their practical viability. By synthesizing data across various material combinations and synthesis strategies, this review identifies trends, performance limitations, and emerging opportunities in the design of efficient ferrite-based photocatalysts. It also outlines future directions for research, including hybridization with next-generation materials and improved methods for tuning photocatalytic properties to meet the demands of sustainable water treatment technologies.

Synthesis of metal ferrite nanomaterials

The synthesis of metal oxide nanoparticles can be achieved through a variety of methods, each offering unique advantages in terms of size control, surface properties, and scalability. This section discusses several commonly used techniques for their preparation.

Co-precipitation method

The co-precipitation method is a popular technology for manufacturing high-purity, nanoscale magnetic ferrite nanostructures due to its low complexity and high yield [88]. This approach is inexpensive and provides precise control over particle size and content. It demands low temperatures and produces materials with high crystallinity, homogeneity, and textural qualities [88,89]. However, notable limitations associated with co-precipitation include extensive particle agglomeration, sub-optimal crystallization, heterogeneous particle size distribution, and the necessity for careful pH control [90,91]. Inorganic salts (such as chlorides, sulphates, or nitrates) are first dissolved in water or another solvent. After correcting the pH to between 7 and 12 and continuously stirring, a precipitate form, which is then extracted by filtering or centrifugation, cleaned, and dried. The rate of pH shift has a substantial impact on particle aggregation and crystallization [88]. Nanostructured ferrites are typically synthesized by combining Co^{2+} and Fe^{3+} salts with a strong base [92]. Nanoparticle size, shape, and magnetic characteristics can be adjusted by varying experimental parameters such as reaction temperature, duration, reagent concentration, pH, and drying temperature [93]. $CoFe_2O_4$ nanoparticles (2 - 47 nm) were synthesized using metal chloride salts and varying quantities of NaOH and NH_4OH solutions, with reaction durations of 2 h and temperatures ranging from

20 - 100 °C [93]. These characteristics influence particle size, with greater temperatures and reaction periods typically producing larger particles [93]. In some cases, an oxidizing agent such as KNO_3 is used to convert Fe^{2+} to Fe^{3+}, leading to the formation of both $CoFe_2O_4$ and magnetite (Fe_3O_4). The crystalline quality and saturation magnetization of the resulting particles depend on the surfactant used and the annealing temperature [94]. Furthermore, reverse co-precipitation is a version of the process in which precursor ions are introduced into the precipitant solution rather than the other way around. This guarantees that the precipitant is supersaturated, resulting in a more thorough precipitation and smaller nanoparticles than in classical co-precipitation [95]. Huixia *et al.* [88] reported the production of $CoFe_2O_4$ nanoparticles using reverse co-precipitation.

Hydrothermal/ solvothermal method

The hydrothermal approach is frequently utilized for large-scale ferrite nanoparticle (NP) synthesis due to its excellent yield efficiency. NPs are formed by combining aqueous solutions of divalent metal acetates (Co, Ni, Zn, Mn) using iron nitrate and a carbon-derived nanostructure template at an alkaline pH [88,96]. In an autoclave, the mixture undergoes heating to around 200 °C. The resulting precipitate is subsequently subjected to washing, isolated through centrifugation, and subjected to annealing at approximately 500 °C to remove the carbon template [97]. Surfactants such as ethylenediamine or citric acid are frequently used during the solution phase to refine the composition of the crystals, particle size, and morphology [98]. This method is advantageous as it doesn't require complex processing or extremely high temperatures. It allows the adjustment of NP properties by varying temperature, pressure, reaction time, and the nano templates used. The hydrothermal method offers several benefits, including excellent control over nucleation, small particle sizes with narrow distributions, regulated morphology, high reaction rates, high yields, and simplicity in the process. There have been reports of magnetic nanosized $CoFe_2O_4$ being produced via this method without the need for additional calcination steps. However, the impact of synthesis time on $CoFe_2O_4$ NP size and morphology remains a topic of discussion [99]. $CoFe_2O_4$ nanorods have also been synthesized using cetyltrimethylammonium bromide (CTAB) as a surfactant. Although porous anodic aluminum oxide templates are employed for one-dimensional $CoFe_2O_4$ nanostructures, the costs are high, and the yields are relatively low. For other ferrites, $NiFe_2O_4$ nanocrystals were synthesized using $FeCl_3{\cdot}6H_2O$ and $NiCl_2{\cdot}6H_2O$ with CTAB as a surfactant. $ZnFe_2O_4$ was produced from metallic Zn and $FeCl_2$ in ammonia solutions [100]. Moreover, the hydrothermal synthesis of various ferrites (MFe_2O_4, where M = Co, Ni, Zn and Mn) utilizing metal acetylacetonates in conjunction with aloe vera extracts resulted in the production of nanoparticles (NPs) that are not only well-crystallized but also exhibit high yield at elevated calcination temperatures [101]. Alzami *et al.* [102] synthesized $Zn_{0.5}Ni_{0.5}$ Fe_2O_4 by hydrothermal process combined with PPy. The PPy and NFs nanohybrid improved several properties, such as reducing recombination, speeding up charge transfer, and extending visible light absorption. These enhancements led to superior MG dye mineralization compared to the ZNF catalyst. The nanohybrid showed stability and photocatalytic efficiency, with optimal conditions being 15 ppm MG dye, acidic solution, and intense visible light [102].

Sonochemical synthesis

The sonochemical process is recognized as one of the most effective methods for producing ferrite nanoparticles (NPs). This method takes advantage of the phenomenon of acoustic cavitation, which involves the development, growth, and implosion of bubbles in liquid media. Cavitation's severe circumstances, including high temperatures (5,000 K), pressures (20 MPa), and rapid cooling speeds (10^{10} K/s), create particles with distinct characteristics. A step, surfactant-free sonochemical technique produced extremely crystalline monodisperse $CoFe_2O_4$ NPs with homogeneous spherical morphologies and high saturation magnetization (MS) [103]. This method requires a short synthesis time (approximately 70 min) and eliminates the need for post-synthesis annealing. Key advantages of the sonochemical approach include simplicity, cost-effectiveness, safety, environmental friendliness, uniform size distribution, high surface area, rapid reaction times, and excellent phase purity [103]. However, its limitations include the production of only small concentrations of NPs and the tendency for particle agglomeration [55]. High-energy

ultrasonication generates localized heat points, reaching pressures of 1,800 atm and temperatures up to 5,000 K. These extreme conditions cause erupting bubbles to collapse, facilitating the formation of iron oxides. This technique also enables the production of monodispersed nanoparticles with diverse morphologies, making it suitable for large-scale nanoparticle synthesis [104]. Natarajan *et al.* [105] used the sonochemical approach to create nanoscale amorphous iron particles by dissolved iron carbonyl in decane. When heated over 300 °C, these particles fuse and crystallize.

Microwave-assisted combustion method

The microwave-assisted combustion technique synthesized nanoparticles (NPs) by converting microwave radiation into thermal energy created within the material. Unlike traditional heating, which applies heat externally, this inside heating dramatically saves operating time and energy usage. The approach has various advantages, including simplicity, quick reaction time, high output rates, environmental friendliness, outstanding reproducibility, and low cost of energy [106–108]. It also enables easy handling and precise control over parameters. By allowing molecular-level mixing of reagents through microwave interaction, the process provides excellent control of stoichiometry, homogeneity, purity and, morphology [88,96,109]. Nevertheless, this methodology can be expensive, primarily due to the employment of expensive reactants, including urea, L-alanine, glycine, carbohydrazide, and citric acid, which facilitate the combustion process. It is also less ideal for growing up and effective reaction monitoring [108,110]. The heat provided by microwaves allows for quick, uniform heating, resulting in homogenous nanomaterials with small particle size distribution. For instance, nitrates of zinc, iron, manganese, copper, nickel, and cobalt are solubilized in deionized water, maintained at a pH of 9.4, and enclosed in tetrafluoromethoxyl (TFM) [109,111]. The mixture is subsequently subjected to thermal processing in a microwave oven at a temperature of 160 °C for a duration of 30 min. After drying, polyvinyl alcohol (PVA) is added as a binder, and the mixture is sintered for 30 min [88]. This approach is both faster and more economical, producing fine, uniform NPs [96].

Sol-gel process

The sol-gel technique constitutes a low-temperature procedure that encompasses both hydrolysis and the condensation of metallic precursors, which may comprise salts or alkoxides, aimed at generating a 3-dimensional inorganic framework. In this process, monomers are transformed into a colloidal form of solution (sol), which then solidifies into a gel as particles bind together after the solvent evaporates. The sol-gel process is simple, cost-effective, and environmentally friendly, making it ideal for preparing nanocomposites (NCs) [112]. It facilitates precise regulation of microstructural attributes, particulate dimensions, distribution, structural configuration, and chemical composition through careful alteration of the synthesis parameters [88,113]. This methodology is frequently employed to synthesize fine, dense, homogeneous, single-phase ferrite nanoparticles (NPs). In contrast to conventional techniques, the sol-gel method offers superior stoichiometric precision and facilitates the production of ferrites at reduced thermal conditions [114,115]. These nanoparticles can be manufactured as films or colloidal powders. However, the approach has drawbacks, such as low efficiency and lengthy synthesis durations. As an example, glycolic acid was used as a chelating agent to synthesize $NiFe_2O_4$ nanostructures with a typical particle size of 27 nm. In the case of $CoFe_2O_4$@SiO_2, the silica network helps protect the NPs, reducing surface roughness and spin disorder, resulting in significantly higher coercivity (HC) values at room temperature compared to uncoated $CoFe_2O_4$ [88,116]. Metal nitrates are frequently employed as a source of metal ions, glycols (such as 1,2-ethanediol, 1,3-propanediol, or 1,4-butanediol) serve as chelating agents, tetraethyl orthosilicate (TEOS) functions as a precursor for the matrix, ethanol acts as a solvent, and nitric acid is also utilized. During annealing, the NPs tend to clump together and form larger particles, prompting additional investigation into the impacts of thermal energy on unwanted particle growth [117,118].

The integrative application of sol-gel and auto-combustion methodologies presents a systematic and economically viable approach for the synthesis of high-purity, homogeneous nanopowders at reduced annealing temperatures. This procedure entails the dissolution of nitrate salts in aqueous medium, the incorporation of an

organic complexing agent, such as citric acid, the adjustment of the pH to a neutral value of 7, and the subsequent heating of the solution to 70 °C to facilitate the formation of the sol. At a temperature of 110 °C, the extraction of residual water occurs, and the nitrate-fuel gel is subjected to an autocatalytic combustion reaction. Citric acid and glucose are commonly used fuels because of their strong complexing properties and low ignition temperatures. The sol-gel auto-combustion method has successfully synthesized $CoFe_2O_4$ NPs ranging in size from 11 to 40 nm, with annealing temperatures between 800 and 1,000 °C [119]. The organic precursor approach, like the Pechini process, requires preparing an aqueous solution containing cations, then chelating them with carboxylic acids, heating the solution to produce a precursor, and then annealing the precursors [119]. Carboxylic acids serve as both complex agents and fuel. Using this method, magnetic $CoFe_2O_4$ NPs (38.0 - 92.6 nm) were prepared with tartaric and oxalic acids as precursors [120].

Combustion method

The combustion process is a straightforward, quick, and inexpensive technology that avoids the need for intermediary decomposition or calcination procedures. The process is predicated upon an exothermic, rapid, and self-sustaining chemical reaction that incorporates metallic salts and organic fuels (including sucrose, urea, glycine, sucrose, citric acid, hydrazine or polyvinyl alcohol), which function as reducing agents [127]. The characteristics of the resultant powders, including crystallite size and surface area, are influenced by the reaction's enthalpy or combustion temperature, which varies depending on the fuel employed and the ratio of fuel to oxidant. Furthermore, the selection of fuel is instrumental in determining the morphology and phase formation of nanoparticles (NP) [121]. A notable advantage of this method is that the heat required for the reaction is generated internally rather than from an external source. Metal nitrates are commonly used as precursors due to their high-water solubility and ability to combust easily when mixed with an appropriate fuel [122]. Ammonium nitrate is frequently used as an additional oxidant to expand microstructures and enhance NP surface area without affecting the quantities of other reactants. The combustion technique is extensively employed for the fabrication of ceramic substances, composite materials, and ferrimagnetic nanostructures due to its efficacy, minimal preparation duration, economically viable precursors, uncomplicated apparatus, meticulous control of balance, tailored particle size distribution, high-purity outputs, and the stabilization of metastable phases. Nevertheless, its drawbacks include elevated combustion temperatures and suboptimal manufacturing yields [123]. This technique is particularly effective for producing high-quality $CoFe_2O_4$, $NiFe_2O_4$, and $MnFe_2O_4$ NPs, with their size, saturation magnetization (MS), and coercivity (HC) values tailored by adjusting the nitrate-to-fuel ratio [88]. For instance, nanocrystalline $NiFe_2O_4$ can be prepared by mixing metal nitrates with citrate to form a colloidal sol, heating the xerogel, undergoing an auto-combustion process to yield loose powder, and annealing the powder at 700 °C [96]. This approach produces high-purity, homogenous NPs with minimum waste but necessitates high temperatures. The high purity is due to the removal of contaminants that are volatile species during burning.

Green synthesis method

The biosynthetic approach offers a sustainable alternative to traditional chemical methods for synthesizing nanomaterials, using plant extracts, microorganisms, and enzymes. This eco-friendly route provides simplicity, high yield, and crystalline nanomaterials with desirable properties [124,125]. For example, Aloe vera extract, rich in long-chain polysaccharides, serves as an efficient bio-reducing agent for synthesizing ferrites, facilitating the uniform distribution of ferrite particles. This method is not only cost-effective but also employs non-toxic reducing and gelling agents, making it an environmentally friendly option [126]. However, certain challenges hinder the broader adoption of biosynthetic techniques. These include the challenges of managing nanoparticle (NP) size and characteristics, the requirement for high temperatures to transform precursors into crystalline materials, and the synthesis of polydisperse or surface-capped NPs. Furthermore, repeatability remains a challenge due to incomplete mixing of reactants and undesirable side reactions, both of which have a negative impact on NP characteristics. Alternative synthesis methods have been explored to address these issues. For instance, using Ni and Fe nitrates with

freshly extracted egg white (ovalbumin) in aqueous media yields $NiFe_2O_4$ NPs with ferrimagnetic behavior and saturation magnetization (MS) values ranging from 26.4 - 42.5 emu/g at room temperature [127]. Despite these advances, repeatability and size control remain major issues. Heat and mechanical treatments, while important for certain structural features, can modify crystal structure and reduce photocatalytic activity. The combustion process is the simplest and fastest of the various ways, but it requires exact monitoring of the ratio of organic fuel to nitrates to maintain size and magnetic characteristics. Solid-state methods yield larger particles at higher temperatures, while citrate precursor methods produce smaller NPs at lower temperatures. For optimum, reproducible synthesis, critical processes include complete reactant mixing, automation, and exact control over reaction variables [128]. In summary, sol-gel and chemical co-precipitation methodologies are recognized as the most advantageous approaches for the fabrication of homogeneous, highly pure, and narrowly dispersed nanoferrites, achieving a harmonious equilibrium between the simplicity of synthesis and meticulous regulation of nanoparticle attributes [129].

Principle of photocatalytic degradation

Due to its many benefits and wide range of uses in environmental remediation, especially the removal of contaminants from wastewater, the use of photo catalysts in aqueous suspension has attracted a lot of attention [130]. The process known as photocatalysis occurs when substances like metal oxides, semiconductors, and organic molecules function as catalysts when exposed to light, facilitating chemical reactions that are fueled by light energy. In contrast to traditional catalysis, photocatalysis uses visible or ultraviolet (UV) light to activate a photocatalyst, increasing the pace of a chemical reaction. Because the materials' catalytic qualities are essential to the process, choosing the right photocatalysts is essential to attaining superior photocatalytic performance. These characteristics include things like the availability of oxidizing agents, band-gap values, and electron-hole recombination rates. To maximize the photocatalytic reaction, factors pertaining to the manufacturing of photocatalysts and the properties of pollutants must also be carefully considered. In order to enhance the photocatalytic properties of a material, various methodologies have been employed, such as surface modification, incorporation of dopants, fabrication of composites, and the development of heterostructures [131]. A potent illumination source, an appropriate photocatalyst (such as MFe_2O_4), and a suitable oxidizing agent are indispensable for the photocatalytic degradation of organic pollutants. The initiation of the process is facilitated by the excitation of electrons from the valence band (VB) into the conduction band (CB) through the absorption of photons possessing energies that exceed the material's band-gap energy (Eg). In contrast, photons characterized by longer wavelengths or reduced energy typically dissipate energy in the form of heat. According to **Figure 1**, the photocatalytic reaction stages entail the semiconductor material absorbing light, which causes electrons to go from the VB to the CB and leave a hole in the VB.

The efficiency of the photocatalyst is determined by the band gap, an energy barrier that separates these bands and inhibits electron-hole recombination. Through scavenging, the hydroperoxyl radical that is created during this process prolongs the life of the photogenerated holes. On the surface of the photoexcited photocatalyst, oxidation and reduction activities occur [132]. Electrons and holes recombine when oxygen eliminates the electrons, producing superoxide radicals (O_2^-), which in turn produce hydrogen peroxide (H_2O_2) and hydroperoxyl radicals (HO_2^-). Intermediates and final products are the result of additional interactions between these reactive species. Photonic activation of the catalyst is the first step in an effective photocatalytic system [132]. The following describes the next steps in using UV light to activate MFe_2O_4 in order to eliminate organic pollutants [133]. In summary, steps 1 to 5 show how the photocatalytic oxidation cycle produces hydroxyl radicals (OH-). A positive hole and an electron are produced at the VB and CB, as well, when sunlight strikes MFe_2O_4 (Eq. (1)). When positive holes, hydroxide (OH), and water (H_2O) mix, hydroxyl radicals (OH^-) are created (Eqs. (2) and (3)). The presence of oxygen inhibits electron-hole recombination, and these hydroxyl radicals are the main agents responsible for decomposing organic pollutants. Furthermore, the interaction of oxygen (O_2) with electrons produces superoxide anions (Eq. (4)). Electron build-up in the CB may enhance electron and hole

recombination, lowering photocatalytic efficiency, if oxygen reduction and pollutant oxidation are not coordinated. Therefore, improving the effectiveness of photocatalytic degradation requires preventing electron accumulation. Lastly, organic contaminants are broken down into carbon dioxide (CO_2) and water (H_2O) by hydroxyl radicals (OH^-) binding to them (Eq. (5)).

$$MFe2O4 + h^+ \rightarrow MFe2O4 + h^+ + e^- \quad (1)$$

$$OH^- + h\vartheta b \rightarrow \cdot OH \quad (2)$$

$$H_2O + h^{+-} \rightarrow \cdot OH + H^+ \quad (3)$$

$$O_2 + e^- \rightarrow O_2 \quad (4)$$

$$OH + organic\ pollutants \rightarrow CO_2 + H_2O \quad (5)$$

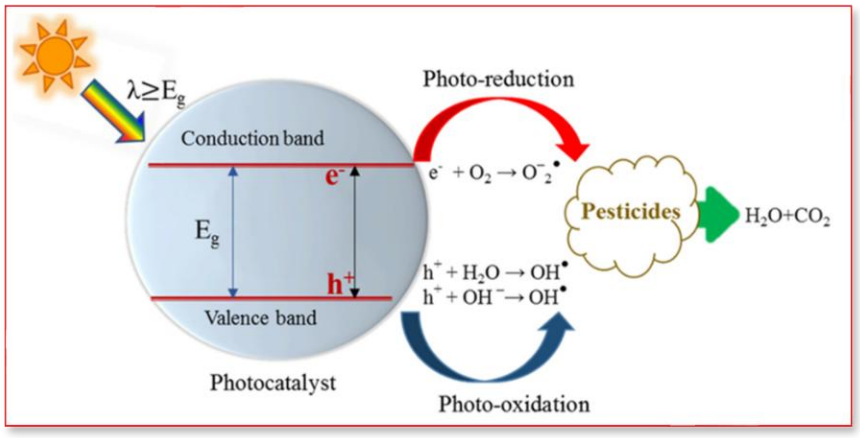

Figure 1 Schematic diagram illustrating the photocatalytic degradation mechanism of organic pollutants [133].

The bonding of hydroxyl radicals (OH^-) to the contaminants successfully decreased the content of organic pollutants. In conclusion, photocatalysts are essential to the photodegradation of organic contaminants. Because of its low band-gap energy, the perfect photocatalyst can lower the rate at which electrons and positive holes recombine. It should also be non-toxic, photoactive, physiologically and chemically inert, able to absorb visible or near-UV light, and resistant to photo corrosion [134]. Numerous photocatalysts have been thoroughly investigated; each has pros and cons, which has led to a broad investigation of appropriate photocatalysts for various pollutants.

Metal nanoferrites as photocatalysts for wastewater treatment

Metal nanoferrites have attracted growing interest in the field of photocatalysis due to their unique structural, electronic, and magnetic properties [135-138]. These substances exhibit a spinel crystal configuration, defined by a cubic close-packed arrangement of oxygen anions, with metal cations positioned in both tetrahedral (A) and octahedral (B) sites. The distribution of cations between these sites can be tailored by adjusting synthesis conditions or doping, enabling precise control over their band structure, magnetic behavior, and surface activity [139,140]. Nano-structuring further enhances their surface area-to-volume ratio, shortens charge diffusion paths, and increases the density of reactive sites, all of which are beneficial for photocatalytic applications. One of the most compelling features of metal nanoferrites is their ability to absorb visible light efficiently, with bandgap energies typically ranging between 1.4 and 2.4 eV depending on the specific metal ion and synthesis route employed. This makes them suitable for solar-driven photocatalytic processes aimed at degrading persistent organic pollutants such as dyes, pharmaceuticals, pesticides, and phenolic compounds. Additionally, their magnetic characteristics facilitate straightforward post-reaction extraction through the application of external magnetic fields, rendering them especially appealing for recurrent utilization in heterogeneous catalysis, thereby diminishing both the financial expenditure and intricacy associated with wastewater treatment methodologies. Metal nanoferrites have also demonstrated strong

potential in activating peroxymonosulfate or peroxydisulfate to generate reactive sulfate radicals ($SO_4^{\bullet-}$), which are known for their high redox potential (2.5 - 3.1 V) and greater selectivity compared to hydroxyl radicals [141,142]. In such AOPs, the transition metal ions (e.g., Fe^{2+}, Co^{2+} and Cu^{2+}) at the surface of the nanoferrites play a crucial role in facilitating electron transfer reactions, thereby accelerating the decomposition of oxidants and the subsequent generation of reactive species [143,144]. Despite these advantages, several challenges limit the widespread application of metal nanoferrites in photocatalysis. One major concern is the rapid recombination of photoinduced electron-hole pairs, which significantly reduces quantum efficiency. Moreover, their redox potential may be insufficient to fully oxidize certain organic pollutants, especially under mild conditions. Long-term stability under repeated cycling and in harsh environments, such as high ionic strength or varying pH, also remains a critical issue, as some ferrites are prone to leaching or surface passivation.

To overcome these limitations, researchers have explored a wide range of modification strategies, including metal or non-metal doping, formation of heterojunctions with other semiconductors (e.g., TiO_2, ZnO and g-C_3N_4), surface functionalization, and coupling with carbon-based materials like graphene and carbon nanotubes as discussed in the sections ahead. Such approaches aim to improve charge separation, extend light absorption, and enhance the adsorption of pollutants or oxidants at the catalyst surface. Furthermore, various synthesis methodologies, including co-precipitation, sol–gel, combustion, hydrothermal, and microwave-assisted techniques, have undergone optimization to regulate parameters such as particle size, morphology, and crystallinity - factors that significantly impact photocatalytic efficacy.

A systematic investigation into the relationships between structural features, electronic properties, and catalytic performance is thus essential to guide the rational design of next-generation nanoferrite-based photocatalysts. With continued research and development, metal nanoferrites hold significant promise for sustainable, efficient, and scalable solutions to contemporary environmental challenges, particularly in the realm of wastewater treatment and emerging contaminant removal.

Structural parameters affecting photocatalysis

The photocatalytic activity of metal nanoferrites is intrinsically governed by their crystal structure, cation distribution, and nanoscale morphology. All metallic ferrites exhibit crystallization in a cubic spinel configuration (space group $Fd\bar{3}m$), characterized by a densely packed lattice of oxygen atoms with metallic cations residing in tetrahedral (A) and octahedral (B) coordination sites. The classification of spinels into normal, inverse, or mixed categories depends on the distribution of M^{2+} and Fe^{3+} ions across the respective sites. In the case of normal spinels such as $ZnFe_2O_4$, the divalent M^{2+} ions are situated at the A-sites, while the Fe^{3+} ions occupy the B-sites; conversely, in inverse spinels such as $CoFe_2O_4$, the Fe^{3+} ions are distributed between the A and B sites, with M^{2+} ions residing solely at the B-sites. Mixed spinels like $NiFe_2O_4$ exhibit an intermediate or partially ordered arrangement of cations between the 2 sites, and this distribution is often influenced by synthesis parameters such as pH, calcination temperature, and precursor ratio. This structural arrangement directly affects the electronic band structure, surface energy, and charge separation behavior of ferrites. The electron transfer processes within ferrites are primarily driven by super exchange interactions between cations (Fe^{3+}–O^{2-}–Fe^{3+} or M^{2+}–O^{2-}–Fe^{3+}), where the strength and directionality of these interactions influence magnetic ordering and electronic conductivity [145,146]. For instance, in zinc ferrite, the optical response is governed by the degree of inversion, which determines the distribution of Zn^{2+} and Fe^{3+} ions between tetrahedral and octahedral sites; higher inversion increases transitions involving the Zn^{2+} 4s energy level (emission at ~464 nm) and reduces transitions from the Fe^{3+} 3d states near the valence band to conduction band levels (emission at ~547 nm). This shift in electronic transitions enhances the lifetime of electrons excited into the Zn^{2+} 4s state, promoting more efficient charge separation and thereby improving the overall photocatalytic activity [147]. In particular, electron hopping between Fe^{2+} and Fe^{3+} at octahedral B-sites enhances local conductivity, a factor that is critical in suppressing recombination of photo-induced charge carriers during photocatalysis [148,149]. Additionally,

the magnetic properties arising from these interactions enable easy magnetic separation of catalysts post-treatment, a practical advantage for environmental applications.

The nanoscale size and morphology of ferrite nanoparticles play a critical role in determining their photocatalytic performance. Particle size directly affects surface area, band gap energy, and the density of active sites, all of which are key parameters influencing photocatalytic efficiency. Smaller ferrite nanoparticles generally exhibit enhanced activity due to their higher surface to volume ratio, which increases the availability of active sites for photocatalytic reactions. Zirconium ferrite nanoparticles with an average size of 43 nanometers have demonstrated up to 95% degradation efficiency of rhodamine B under ultraviolet irradiation, surpassing the performance of larger particles. Changes in particle size also alter optical properties; in zirconium ferrite, an increase in particle size resulted in a reduction of the band gap from 2.5 to 2.24 eV, thereby improving the absorption of visible light and enhancing photocatalytic activity [150]. In addition to size, the morphology of ferrite nanoparticles significantly influences their catalytic behavior. Distinct morphologies such as needle like, cube like, plate like, and spherical forms affect surface area, light absorption, and interaction with pollutants. Needle like zinc ferrite structures have exhibited the highest photocatalytic degradation efficiency for methyl orange, attributed to their optimized surface area and crystallinity [151]. Spherical nanoparticles, widely reported in the literature, offer uniform light exposure and enhanced interaction with contaminants due to their homogeneous distribution and large reactive surface area, contributing to improved photocatalytic performance [152]. The synthesis of spinel ferrite nanoparticles using methods like urea-assisted combustion results in nanoscale particles with high crystallinity, which is crucial for their magnetic and electronic properties. The absence of secondary phases in these materials further supports efficient transport [153].

Moreover, defect engineering has become a critical strategy for boosting the photocatalytic efficiency of ferrites, especially for solar driven environmental applications. By deliberately introducing structural imperfections such as oxygen or cation vacancies, this approach enhances light absorption, promotes charge carrier separation, and suppresses recombination through the formation of midgap trap states [154,155]. The concentration of oxygen vacancies in spinel ferrites can be significantly enhanced by doping with lower valent or smaller radius cations and through controlled thermal treatment. In $NiFe_2O_4$, e.g., oxygen nonstoichiometry (δ) increases markedly with rising sintering temperature, from 0.0014 at 1,150 °C to 0.0355 at 1,400 °C, due to thermally induced oxygen loss under reduced oxygen partial pressures, thereby modifying the defect landscape and electronic structure [156]. These defects not only broaden visible light utilization by tuning the optical bandgap but also increase the density of surface-active sites, thereby accelerating redox reactions and improving overall photocatalytic performance. However, excessive disorder can also introduce non-radiative recombination centers, underscoring the need for optimal defect engineering. The type of spinel arrangement, cation distribution, degree of inversion, crystallinity, and presence of defects collectively influence key performance metrics including light absorption, charge carrier mobility, surface reactivity, and redox capability. Rational control over these structural parameters through judicious selection of synthesis routes and dopants is therefore essential for tailoring nanoferrites for specific photocatalytic applications.

Compositional Parameters affecting photocatalysis

In addition to structural features, compositional modifications through doping or hybridization play a pivotal role in optimizing the photocatalytic potential of metal nanoferrites. Divalent transition metal ions such as Mn^{2+}, Cu^{2+}, Co^{2+}, and Zn^{2+} are widely employed for A-site substitution in spinel ferrites to enhance photocatalytic activity. These dopants modulate the local crystal field environment and introduce defect states that promote efficient charge separation while preserving the structural integrity of the spinel lattice [157,158]. Their ionic radii closely match that of A-site cation, minimizing lattice strain, and their variable oxidation states facilitate the formation of oxygen vacancies and electronic trap states [29], both of which contribute to reduced charge carrier recombination and extended light absorption [159]. The incorporation of such cations fine-tunes the band structure, enhances

redox potential, and improves the overall photocatalytic kinetics by fostering better electron mobility and surface reactivity under visible light irradiation [160–162]. The improved photocatalytic activity is attributed to the unique characteristics of Mn^{2+} ions, which facilitate polaron formation and hopping, enhancing electron transport within the spinel lattice [159]. In a similar study, copper-doped $NiFe_2O_4$ spinel nanoparticles synthesized via a microwave combustion method exhibited a notable band gap reduction from 3.25 to 2.39 eV with increasing Cu content, enhancing visible-light absorption and charge carrier dynamics. The optimized composition, $Ni_{0.6}Cu_{0.4}Fe_2O_4$, achieved a significantly higher photocatalytic degradation efficiency (99.85%) compared to pristine $NiFe_2O_4$ (88.26%), primarily due to improved separation and reduced recombination of photogenerated electron-hole pairs [163].

Trivalent metal cation doping is generally employed at the B site in spinel ferrites, using ions such as Cr^{3+}, Al^{3+}, Ga^{3+}, Y^{3+}, and Sc^{3+}. These dopants influence Fe^{3+}–O^{2-}–Fe^{3+} super exchange interactions, modify cation distribution, and introduce lattice distortions or oxygen vacancies that enhance charge carrier separation and reduce recombination [164,165]. Transition metal ions like Cr^{3+} improve redox activity and enhance electrical conductivity [165,166], while non-transition dopants such as Al^{3+} and Y^{3+} create defect states and strain in the lattice, broadening light absorption and increasing surface reactivity [167]. The type and concentration of dopants in metal nanoferrites significantly influence both photocatalytic efficiency and magnetic properties by modifying the band structure, charge dynamics, and magnetic interactions. For instance, Cr^{3+} doping in Ni-Zn ferrites initially enhances saturation magnetization but reduces it at higher concentrations due to site occupancy effects [145,165]. Al^{3+} substitution in $Mn_{0.5}Cu_{0.5}Cr_xFe_{2-x}O_4$ disrupts magnetic coupling and decreases both saturation magnetization and coercivity, attributed to the non-magnetic nature of Al^{3+} and reduced particle size [164]. Conversely, Ga^{3+} doping in $NiCr_{0.2}Fe_{1.8}O_4$ improves magnetic moment and remanence by strengthening magnetic interactions [168]. In a detailed study, rare earth elements (Sm, Dy, Ho, Er and Yb) were doped into manganese ferrite (MF) via the coprecipitation method to enhance both photocatalytic and magnetic properties. UV-Vis. spectra showed broad absorption from 250 - 800 nm, enabling efficient utilization of both UV and visible light. Among the dopants, Sm, Dy, and Ho-doped MF significantly improved charge separation and electrochemical conductivity, attributed to enhanced electron mobility and reduced recombination of photogenerated carriers. Electrochemical tests revealed a trend in electron transfer efficiency (Sm-MF > Dy-MF > Ho-MF > MF > Er-MF > Yb-MF), with Sm-MF exhibiting the most positive corrosion potential (−0.10 V), indicating excellent structural stability and photocatalytic performance. Conversely, Er and Yb dopants negatively impacted the electrochemical behavior, highlighting the importance of dopant selection in optimizing MF-based photocatalysts [169]. In a study on cerium-doped spinel ferrites synthesized via chemical co-precipitation, $Ni_{0.6}Cu_{0.4}Ce_xFe_{2-x}O_4$ (x = 0.0 - 1.5) demonstrated a clear dependence of photocatalytic performance on the doping level, with the highest degradation efficiency of ~91% for Congo red (CR) observed at x = 1.5 under 60 mg catalyst dose at pH 6.5. The activity followed the trend: $Ni_{0.6}Cu_{0.4}Fe_2O_4$ < $Ni_{0.6}Cu_{0.4}Ce_{0.5}Fe_{1.5}O_4$ < $Ni_{0.6}Cu_{0.4}CeFeO_4$ < $Ni_{0.6}Cu_{0.4}Ce_{1.5}Fe_{0.5}O_4$. Structural and optical analyses revealed that increased Ce^{3+} substitution at x = 1.5 resulted in enhanced octahedral cation occupancy, larger particle size, and a narrowed bandgap, facilitating improved light absorption and charge transfer. Additionally, the catalyst retained structural integrity and photocatalytic efficiency upon recycling, highlighting its stability and reusability [170].

Eu^{3+}-doped $CoFe_2O_4$ nanoparticles synthesized via a sol–gel auto-combustion method exhibited enhanced photocatalytic performance, achieving 95.98% degradation of Rhodamine B under visible light compared to 89.77% by the undoped sample. The improvement is attributed to the role of Eu^{3+} ions as charge trapping centers, which effectively reduce electron-hole recombination. Moreover, the internal redox cycling between Eu^{3+} and Eu^{2+} extends charge carrier lifetimes and facilitates the generation of reactive oxygen species ($\bullet O_2^-$, •OH), thereby boosting photocatalytic efficiency [171]. Another crucial compositional strategy involves forming heterojunctions between ferrites and other semiconductors, which not only suppresses rapid charge recombination by promoting spatial separation of

electrons and holes but also enhances the overall photocatalytic efficiency. The construction of Type II, Z scheme, or Schottky junctions facilitates synergistic charge transfer between semiconductors with aligned band structures, while simultaneously helping the catalysts maintain their structural integrity and catalytic performance over multiple cycles [172-174]. The combination of spinel ferrites with materials such as g-C_3N_4, TiO_2, ZnO, and MXenes is increasingly popular due to their complementary electronic structures and their ability to promote effective charge separation (discussed in detail later). Schottky junctions are formed when a metal with a higher work function is coupled with a semiconductor, creating a potential barrier that facilitates electron flow while minimizing recombination [175]. The use of noble metals like Au and Pt in these junctions is beneficial due to their high work function, which enhances the barrier height and improves charge transfer efficiency [176]. The Schottky junction facilitates the generation and transfer of plasmon-induced hot electrons, which are crucial for photocatalytic reactions. These hot electrons can be efficiently collected and utilized, leading to enhanced photocatalytic activity [177]. The Z-scheme mechanism involves the transfer of electrons from the conduction band of one semiconductor to the valence band of another, maintaining high redox potential for pollutant degradation [178]. Surface functionalization by introducing functional groups, polymers, or nanoparticles improves the photocatalytic performance of metal ferrites by enhancing reactant adsorption, facilitating charge separation, and promoting surface redox reactions. For instance, Surface functionalization of $Co_{1-x}Zn_xFe_2O_4$ nanodots with polyaniline (PANI) has been achieved via hydrothermal process. The $Co_{1-x}Zn_xFe_2O_4$/PANI nanophotocatalyst exhibited exceptional photocatalytic performance, achieving nearly 98% degradation of DR-1, RO-16, RB-222 and RY-145 dyes within a span of 5 min. The most effective degradation was noted at a dye concentration of 30 mg/L and a nanophotocatalyst concentration of 1 g/L, with optimal results realized at a 1:0.67 ratio of $Co_{1-x}Zn_xFe_2O_4$ to aniline. The nanophotocatalyst exhibited stable photocatalytic performance across a wide range of pH values and temperatures, maintaining approximately 82% efficiency after 7 cycles, demonstrating its excellent reusability and stability [179]. Using *Ulva lactuca* L. biomass and extracts, green synthesis of biochar/$CoFe_2O_4$ (BCF) nanocomposites was achieved, yielding a multifunctional material with superior photocatalytic properties. The optimized nanocomposite, characterized by a weight ratio of biochar to $CoFe_2O_4$ of 10:4, demonstrated a diminished band gap of 1.58 eV and accomplished a 96% degradation of Congo Red under visible light within a time frame of 70 min ($k = 0.0394$ min^{-1}), markedly exceeding the performance of pure biochar (37%) and unmodified $CoFe_2O_4$ (58%) [180]. Decorating metal nanoferrites with plasmonic nanoparticles such as Ag or Au induces localized surface plasmon resonance, which amplifies visible light absorption and enhances photocatalytic reactivity through improved charge carrier dynamics. The Au/$ZnFe_2O_4$@rGO composite achieved 96% degradation of bromophenol blue dye under sunlight, significantly outperforming pure $ZnFe_2O_4$, due to the enhanced charge separation and electron transfer facilitated by the plasmonic effect of Au NPs [181]. Moreover, activation-induced photocatalysis using metal nanoferrites focus on integrating external stimuli such as persulfate activation [182], photo-Fenton-like reactions [183] and sonophotocatalysis [184] to boost photocatalytic efficiency. These approaches leverage the inherent redox activity and magnetic recoverability of spinel ferrites to generate reactive oxygen species (ROS) more effectively.

Operational parameters

Beyond intrinsic structural and compositional characteristics, the photocatalytic performance of metal nanoferrites is heavily influenced by external operational parameters such as pH, temperature, light intensity, pollutant concentration, and oxidant dosage. These conditions modulate the surface charge of the photocatalyst, the generation and lifetime of reactive species, and the adsorption-desorption equilibrium of pollutant molecules. Temperature plays a significant role in influencing the morphology, crystalline, electronic, and magnetic properties of spinel ferrites, all of which are important determinants of their photocatalytic performance. In the case of $SrFe_2O_4$, the synthesis temperature has a notable effect on morphology, with a transition observed from nanoribbons to dendritic structures and ultimately to

hexagonal nanoplatelets as the temperature increases from 85 to 160 °C. These morphological changes correlate with improved photocatalytic degradation of methylene blue, indicating enhanced performance at higher synthesis temperatures [185]. Temperature also affects cation distribution within the spinel lattice. For instance, in $NiFe_2O_4$, an increase in calcination temperature leads to a decrease in the occupancy of Ni^{2+} ions at the tetrahedral (A) sites, influencing the material's magnetic properties [186]. Higher synthesis temperatures generally promote increased crystallinity, which can suppress electron-hole recombination and thereby improve photocatalytic efficiency [187]. Structural parameters such as lattice constants and bond lengths, which are sensitive to temperature, also impact the optical behavior of these materials. In $CuFe_2O_4$, higher calcination temperatures enhance both saturation magnetization and photocatalytic activity, attributed to changes in the structural and optical characteristics [188]. Similarly, $Mg_{0.7}Zn_{0.3}Fe_2O_4$ nanoparticles exhibit increased dielectric properties and photocatalytic degradation efficiency at elevated temperatures, reflecting improved charge carrier dynamics [189].

Temperature can further influence the electronic band structure of ferrite photocatalysts, potentially enabling absorption of lower-energy photons and enhancing redox capability during photocatalytic reactions [190]. However, while elevated temperatures often improve properties such as crystallinity and charge separation, excessively high temperatures may lead to particle agglomeration, resulting in reduced surface area and fewer active sites, which can adversely affect photocatalytic efficiency [191,192]. Therefore, the optimal synthesis temperature must be carefully tailored to each spinel ferrite composition and synthesis route. Additionally, environmental and economic considerations associated with high-temperature synthesis should be addressed to ensure the sustainable and cost-effective production of spinel ferrites for photocatalytic applications.

The pH level during synthesis significantly affects the crystallite size and lattice parameters of spinel ferrites. For instance, $Ni_{0.3}Cu_{0.3}Zn_{0.4}Fe_2O_4$ synthesized at different pH levels showed variations in crystallite size from 31.12 to 45.32 nm and lattice dimensions from 8.4175 to 8.4368 Å, indicating structural enhancement with pH variation [193]. In $CuFe_2O_4$ spinel, pH influenced the distribution of iron and copper ions within the octahedral and tetrahedral sublattices, affecting the overall structure and properties of the ferrite [194]. In $MgFe_2O_4$, an increase in pH resulted in larger particle sizes and improved crystallinity, which enhanced the magnetic properties [195]. Changes in pH can shift the conduction and valence band edges of the photocatalyst, affecting the generation and separation of charge carriers. This shift can either enhance or reduce the photocatalytic activity depending on the alignment of the band edges with the redox potential of the pollutants [196]. The sol-gel method used for $SrFe_2O_4$ nanoparticles demonstrated that increasing pH from 1 to 9 leads to a decrease in the band gap, which is associated with changes in crystallite size and ion distribution [197].

The pH of the solution affects the surface charge of the photocatalyst, which can enhance or inhibit the adsorption of pollutants. For instance, at a pH lower than the point of zero charge (pH ZPC), the catalyst surface becomes positively charged, which can enhance the degradation of negatively charged pollutants through electrostatic attraction [198]. Conversely, at a pH higher than the pH ZPC, the surface becomes negatively charged, which may repel negatively charged pollutants as evident from the photo-degradation evofloxacin using Ni-Zn ferrite [199]. At acidic pH levels, the increased concentration of protons can lead to the protonation of surface hydroxyl groups on nanoferrites, which reduces electrostatic repulsion between particles and promotes aggregation [200]. This aggregation can decrease the available surface area for catalytic reactions and potentially lead to sedimentation resulting in decreased photocatalytic efficiency. Moreover, Ferrites may undergo partial dissolution or leaching of metal ions (e.g., Fe^{3+}, Co^{2+} and Ni^{2+}), especially under strong acidic conditions (pH < 4). This compromises structural integrity and reduces photocatalytic activity over time. Conversely, extreme alkaline conditions may also lead to the formation of metal hydroxide precipitates, which can alter the surface properties and reactivity of the nanoferrites. Therefore, maintaining a near-neutral pH is often considered optimal for the stability of metal nanoferrites in photocatalytic applications. From a process engineering perspective, minimizing the need for chemical pH adjustment post photocatalysis reduces treatment costs and simplifies reactor design. While

laboratory studies often demonstrate higher photocatalytic efficiencies under extreme pH values, these conditions are less feasible for large-scale implementation. Therefore, developing photocatalysts that retain high performance under near-neutral pH is crucial for advancing real-world wastewater treatment technologies.

Hybrids of metal ferrite as photocatalysts

Titanium dioxide (TiO_2)/ ferrites

Titanium dioxide (TiO_2) is a well-studied photocatalyst because of its chemical stability, nontoxicity, strong oxidative strength, and low cost. It has been widely employed in environmental cleaning, biocidal applications, and energy-based applications such as solar energy production and photocatalytic water splitting [201,202]. However, TiO_2 has severe limitations, most notably a high band gap that limits its activation to UV light and the quick recombination of photogenerated electron-hole pairs, which decreases photocatalytic efficacy. To overcome these restrictions, a variety of techniques have been used, including metal and non-metal doping to improve charge carrier separation and lower the band gap, as well as dye sensitization to boost visible light absorption and electron lifetime [203]. Incorporating spinel ferrites with TiO_2 presents a promising approach to address these challenges. Spinel ferrites, such as those with the MFe_2O_4 structure (where M is a transition metal), offer unique properties like a smaller band gap suitable for visible light absorption, magnetic properties, and biocompatibility, making them versatile for various applications. The combination of TiO_2 with ferrites can enhance photocatalytic performance by improving charge separation and extending the light absorption range. For instance, TiO_2-doped nanocrystalline $Ni_{0.4}Cu_{0.3}Zn_{0.3}Fe_2O_4$ ferrites have shown a decrease in band gap energy with increased TiO_2 doping, indicating enhanced semiconducting properties [204]. Additionally, the magnetic properties of ferrites facilitate the separation and recovery of photocatalysts under a magnetic field, addressing the issue of material separation from process suspensions [73]. However, TiO_2 has severe limitations, most notably a high band gap that limits its activation to UV light and the quick recombination of photogenerated electron-hole pairs, which decreases photocatalytic efficacy. To overcome these restrictions, a variety of techniques have been used, including metal and nonmetal doping to improve charge carrier separation and lower the band gap, as well as dye sensitization to boost visible light absorption and electron lifetime. O_2^- species

Helmy *et al.* [205] utilized CuCe-Ferrite/TiO_2 and TiO_2 nanostructures synthesized through a co-precipitation process, followed by heating at 550 °C for 2 h. The author attributed the superior photocatalytic activity of the TiO_2/CuCe ferrite composite compared to bare TiO_2 to the addition of CuCe-Ferrite dopants. These dopants create localized full states and/or oxygen vacancies within the TiO_2 crystals. As a result, these changes lead to the formation of a mid-bandgap, effectively shifting the optical energy band edge of TiO_2 into the visible light range, thus enhancing its photocatalytic performance as shown in **Figure 2**.

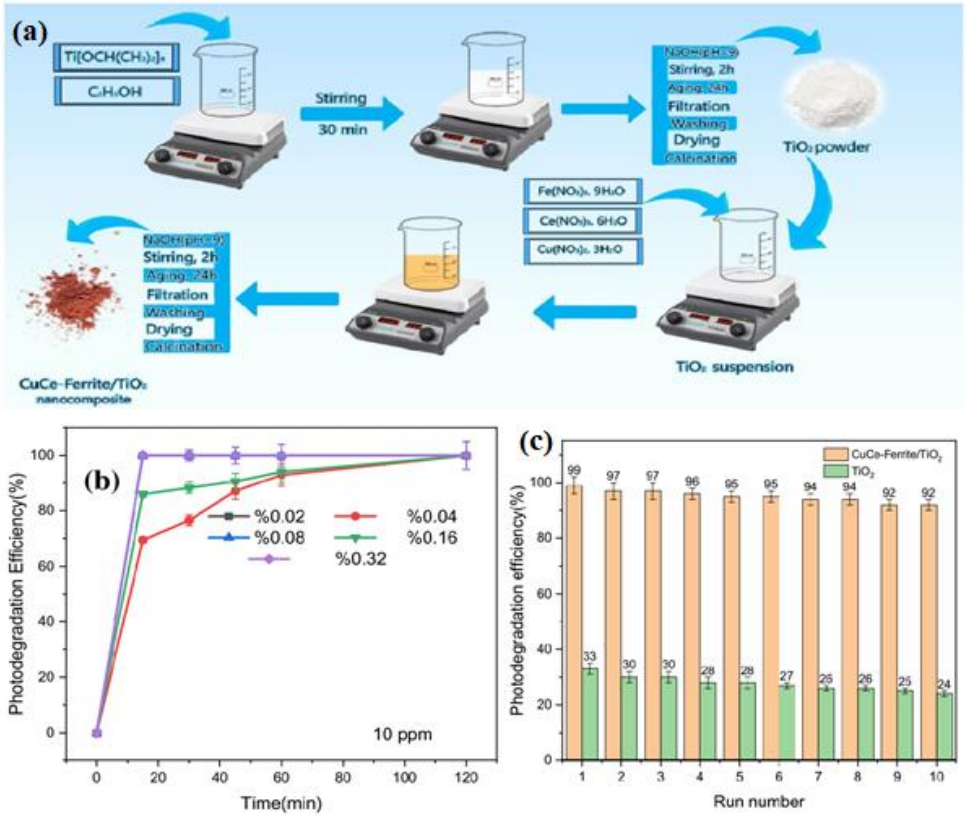

Figure 2 (a) Schematic of the synthesis process for CuCe-Ferrite/TiO_2; (b) Performance of CuCe-Ferrite/TiO_2 NPs in degrading 10 ppm R250 dye over various time intervals; (c) Longevity of CuCe-Ferrite/TiO_2 and TiO_2 NPs after ten usage cycles [205].

Li *et al.* [206] investigated the photocatalytic potential of $ZnFe_2O_4/TiO_2$ (ZF-T) nanocomposites, focusing on their performance under visible light. The synthesis involved dissolving $Zn(CH_3COO)_2{\cdot}2H_2O$, $Fe(NO_3)_3{\cdot}9H_2O$, and TiO_2 in ultrapure water, followed by stirring, ultrasonication, and adjusting the pH to 10. The mixture was autoclaved at 180 °C for 12 h, then dried and heated at 400 °C. Various $ZnFe_2O_4/TiO_2$ ratios (0%, 1%, 5%, 7%, 10% and 15%) were examined. $ZnFe_2O_4$ has a band-gap of 1.90 eV, compared to TiO_2's 3.20 eV, which extends light absorption into the visible region. This doping creates lattice defects in TiO_2, which improves electron-hole pair separation and transport, hence increasing photocatalytic activity. Because of $ZnFe_2O_4$'s high surface area, ZF-T nanocomposites have a greater specific surface area than pure TiO_2. This increased surface area improves visible light absorption and free radical production, thereby enhancing the photodegradation of malachite green (MG). Under conditions of 10 mg/L malachite green (MG), 1.0 g/L catalyst concentration, pH 7.0, and illumination with a 500 W xenon lamp for 240 min, the 10% ZF-T composite achieved 90.1% MG degradation, significantly outperforming pure TiO_2, which reached 53.5%. $ZnFe_2O_4$ exhibits a Z-type heterojunction structure that facilitates efficient charge transfer under visible light. Electrons in $ZnFe_2O_4$'s valence band (VB) may shift to its conduction band (CB) since TiO_2 has a lower CB energy position (−0.29 eV) than $ZnFe_2O_4$ (−1.54 eV). This energy differential enables easy electron transfer from $ZnFe_2O_4$ to TiO_2's CB, resulting in greater separation of electron-hole pairs and lower recombination rates. Consequently, the ZF-T photocatalytic system effectively mitigates the high electron-hole recombination tendency of TiO_2, thereby enhancing interfacial charge transfer efficiency. Furthermore, despite the relatively stable nature of benzene rings with a low delocalization energy of 152 kJ/mol, the energy provided by the free radicals and electronic holes generated in the ZF-T system under visible light is adequate to disrupt the delocalized π bonds. This disruption results in the complete

degradation of methyl green (MG), demonstrating the effectiveness of the ZF-T system in photocatalytic applications. The photocatalytic efficiency remained above 80% over 5 consecutive 4-hour cycles, demonstrating good stability and reusability. UV-vis spectroscopy alongside liquid chromatography-mass spectrometry confirmed the successful disintegration of benzene rings and the degradation of heterocyclic aromatic hydrocarbons, thereby affirming the superior efficacy of the ZF-T system.

$NiFe_2O_4$ was synthesized via sol-gel auto-combustion using glycine as a fuel and combined with TiO_2 through solid dispersion to form a $NiFe_2O_4/TiO_2$ heterostructure. Electrochemical analysis showed $NiFe_2O_4$ as p-type and TiO_2 as n-type, with $NiFe_2O_4$ exhibiting lower charge transfer resistance, enhancing photocatalytic activity. For $NiFe_2O_4$, the band gap is found to be 1.64 eV, which allows it to absorb visible light. TiO_2 has a band gap of 3.21 eV, making it effective in absorbing UV light. The mixture of wavelengths in the heterostructure attempts to use both visible and UV light for photocatalytic activities. Solar irradiation ($hv > Eg$) causes electrons to travel from the conduction band (CB) of p-$NiFe_2O_4$ to the CB of n-TiO_2, while holes move from the valence band (VB) of n-TiO_2 to the VB of p-$NiFe_2O_4$, preventing charge carrier recombination. Hydroxyl radicals (•OH) generated by water reduction on the n-TiO_2 surface attack Congo red dye molecules. The unique band positions of p-$NiFe_2O_4$/n-TiO_2 facilitate the reduction of O_2 to superoxide ($O_2^{\bullet-}$), forming a Z-scheme photocatalytic system. This mechanism leads to a 97% degradation efficiency of Congo red dye after 180 min of sunlight irradiation [207].

In a similar study, Ciocarlan *et al.* [208] synthesized ferrite magnetic nanoparticles (MNPs) with the composition $Co_{0.5}Zn_{0.25}M_{0.25}Fe_2O_4$ (M = Ni, Cu, Mn and Mg) using a co-precipitation method. This spinel structure, which incorporates various cations, offers a promising solution to the common limitations faced in photocatalytic reactions. The inclusion of Co^{2+} ions impart strong magnetic properties to the ferrite systems, facilitating the separation and reuse of the photocatalysts. Zn^{2+} has a low energy band gap and excellent catalytic capabilities in its oxide form, leading to increased photocatalytic efficiency in the composite. The UV-vis diffuse reflectance spectra (DRS) confirm the activation of these nanocomposites under visible light, which is crucial for solar-driven applications. The presence of magnetic nanoparticles (MNPs) in the composite also contributes to the improved crystallinity of the titania phase, which is beneficial for photocatalytic performance. For methyl orange (MO), $Co_{0.5}Zn_{0.25}Ni_{0.25}Fe_2O_4/TiO_2$ achieved a 95% degradation rate according to UV-vis spectroscopy and approximately 80% based on TOC measurements after 6 h of solar irradiation. For methylene blue (MB), the most effective degradation was observed with $Co_{0.5}Zn_{0.25}Ni_{0.25}Fe_2O_4/TiO_2$ and $Co_{0.5}Zn_{0.25}Mn_{0.25}Fe_2O_4/TiO_2$, each achieving 99% degradation as measured by UV-vis spectroscopy within 80 min of solar light exposure. This type of magnetic composite, similar to previously reported $CoFe_2O_4$-TiO_2 and Fe_3O_4-TiO_2 systems, not only shows high efficiency in dye photodegradation but also offers the advantage of easy recovery post-process due to its magnetic nature.

Transitioning from photocatalytic oxidation to photoelectrochemical processes significantly enhances wastewater remediation by integrating electron flow with photocatalytic reactions. This approach allows precise control over oxidative processes and improves pollutant degradation by leveraging the synergy of light-driven charge generation and electrochemical reactions. Photoelectrochemical oxidation fits within the photocatalytic regime when semiconductors are employed to facilitate both light-induced charge generation and electrochemical reactions, thereby optimizing performance under various conditions. The integration of Plasmonic NPs like Ag and Au into heterojunctions has demonstrated improved photocatalytic degradation of dyes and antibiotics. This impact is particularly noticeable when the dimensions of the Ag nanostructures is optimized, as proven by Ag nanocubes on TiO_2, which produced 12 times more photocatalytic hydrogen than pristine TiO_2 [208]. The presence of plasmonic metals like Au improves photocatalytic performance by enhancing light absorption through localized surface plasmon resonance and increasing charge carrier separation due to efficient electron transfer. This is supported by studies on Au/TiO_2 systems, where metal-support interactions improved charge separation and migration [209,210]. The combination of plasmonic nanoparticles with magnetic components like Fe_3O_4 in TiO_2 composites

creates magneto-plasmonic photocatalysts. These composites benefit from both the magnetic separation capabilities of Fe_3O_4 and the enhanced light absorption due to plasmonic effects, leading to significantly improved photocatalytic degradation of pollutants [211].

The synthesis and characterization of Ag-$CoFe_2O_4$@TiO_2 hetero-nanostructures were effectively achieved using the sol-gel combustion technique, which facilitated the creation of a heterojunction with enhanced electrochemical and photoelectrochemical properties. This method involved dissolving citric acid in distilled water, followed by the addition of cobalt nitrate and iron nitrate in a 1:2 ratio. The pH was adjusted to 10 - 12 using NaOH, and a black-colored AgO solution was incorporated, resulting in the formation of Ag-$CoFe_2O_4$ gel. This gel was calcined at 550 °C for 120 min to produce Ag-$CoFe_2O_4$ powder, which was then washed and dried to obtain the nanocomposites. The incorporation of cobalt into TiO_2 results in a narrowing of the band gap, which is evident from the UV-DRS results. This narrowing is caused by the creation of defect sites, such as oxygen-vacancy sites and Ti-C bond formation, which increase light absorbance and improve TiO_2's photocatalytic efficiency by shifting the absorption intensity. Specifically, the addition of silver (Ag) to the Co Fe_2O_4@TiO_2 (CFT) structure causes a modest red shift in the absorption edge, which reflects increased photocatalytic efficiency under visible light circumstances. The band gap of the Ag-modified CFT (ACFT) is reduced from 2.0 to 1.9 eV, extending the photocatalysis spectrum into the visible light range and allowing for more efficient solar energy utilization. When •OH radicals react with the isobutyl group in ibuprofen, they form several metabolites, which undergo further degradation through decarboxylation and hydroxylation, eventually leading to ring cleavage and the mineralization of CO_2 and H_2O. Under direct sunlight irradiation, the ACFT heterostructures achieve complete oxidation of ibuprofen at a potential of 0.8 V versus the reversible hydrogen electrode (RHE), showcasing their high performance in photoelectrochemical applications [212].

Following the comprehensive assessment of the photocatalytic performance of ferrite/TiO_2 heterostructures, it is crucial to address the underlying challenges that impact their operational efficiency and effectiveness in wastewater treatment applications. One significant issue is ensuring the phase stability and compatibility of the ferrite and TiO_2 components under operational photocatalytic conditions, as phase separation or degradation could undermine effectiveness. Efficient charge carrier dynamics are essential, necessitating design strategies to enhance charge separation and reduce recombination. The heterostructure must also offer a high surface area and active sites to maximize photocatalytic activity. Given TiO_2's typical UV absorption and ferrites' visible light absorption, optimizing the light absorption range to cover a broad spectrum is crucial. Additionally, the stability of the photocatalyst under the harsh conditions of wastewater, including variable pH, temperature, and the presence of diverse contaminants, is a key concern. The scalability and cost-effectiveness of synthesizing these heterostructures for industrial applications, alongside their reusability and regeneration potential, are also important factors that are given in Table 1. Finally, tailoring the photocatalyst for broad-spectrum or targeted contaminant removal remains a challenge, requiring precise optimization of material properties and operational parameters.

Table 1 Photocatalytic performance of various ferrite/TiO_2 composites.

Photocatalyst	Preparation method	Contaminant	Light source	Irradiation time	Degradation percentage	Ref.
$CoFe_2O_4$/TiO_2	Sol-gel and electrospinning	methylene blue	300 W Hg lamp	5 h	95.87%	[213]
$CoFe_2O_4$/TiO_2	sol-gel	tetracycline	UV and Visible	3 h	75.31% and 50.4%	[214]

Photocatalyst	Preparation method	Contaminant	Light source	Irradiation time	Degradation percentage	Ref.
$NiFe_2O_4/TiO_2$	simultaneous solution blow spinning	Congo red and Crystal violet	Visible light	30 and 300 min	87% and 77%	[215]
$NiFe_2O_4/TiO_2$	Sol gel	Naphthalene	Visible Light	150 min	67%	[216]
$NiFe_2O_4/TiO_2$	Sol gel and Solid dispersion	Congo Red	Solar light	3h	97%	[207]
$NiFe_2O_4/TiO_2$	polymeric precursor	Arsenic As(III)	Visible	80 min	97.5%	[217]
$ZnFe_2O_4/TiO_2$	Solvothermal	bisphenol A	visible	20 min	> 99%	[218]
$ZnFe_2O_4@TiO_2$	solvothermal	RhB	UV	1 h	97.3%	[219]
$CuFe_2O_4/TiO_2$	Sol gel	Methylene Blue	visible	3 h	83.7%	[220]
$(CuCe)Fe_2O_4/TiO_2$	co-precipitation	reactive red 250 (RR250)	visible	15 min	100%	[205]
$Cu_{0.5}Mg_{0.5}Fe_2O_4–TiO_2$	Coprecipitation and sol gel	Rhodamine B	Simulated sunlight	3 h	98.4%	[221]
(Co,Mn) $Fe_2O_4@TiO_2$.	modified Pechini method	Azo dye (RNL)	UV	16 h	76.3%	[222]
MnCo–Ferrite/TiO_2	coprecipitation	Congo Red Methylene Blue	UV	3 h	99%	[223]
$Co_{0.5}Zn_{0.25}Ni_{0.25}Fe_2O_4$-$TiO_2$	Co-precipitation	Methyl Orange Methylene Blue	Solar light	6 h 80 min	95% 100%	[208]

SiO_2/ ferrites

SiO_2, though not an active photocatalyst due to its wide band gap, plays an important role in improving photocatalytic system performance due to its outstanding stability, large surface area, and capacity to scatter active photocatalysts and avoid agglomeration. Ferrite-based materials, while appealing due to their morphological and optical features, frequently suffer restrictions such as quick charge carrier recombination and particle accumulation, which diminish their photocatalytic effectiveness [224,225]. Agglomeration leads to a decrease in the surface area available for photocatalytic reactions, thereby diminishing the overall activity of the catalyst. Forming SiO_2/ferrite composites is advantageous for several reasons, particularly in terms of agglomeration, surface area, and electron-hole recombination. The incorporation of a SiO_2 matrix helps in controlling the size and distribution of ferrite nanoparticles, which significantly reduces agglomeration. For instance, the sol-gel method used to prepare $CoFe_2O_4$ nanoparticles dispersed in a SiO_2 matrix results in spherical particles that are less agglomerated, as the SiO_2 matrix provides numerous nucleation sites that restrict particle growth and prevent clumping [226]. In addition, the incorporation of $Co_{0.4}Zn_{0.4}Ni_{0.2}Fe_2O_4$ nanoparticles within SiO_2 at varying ratios demonstrates that the specific surface area is enhanced with an increase in SiO_2 content, which is

essential for photocatalytic applications that necessitate materials with elevated surface areas [227].

Ferrite/SiO_2 core-shell and intermediate composites play an important role in increasing photocatalytic efficiency by reducing electron-hole recombination. The SiO_2 layer serves as a protective barrier around the ferrite core, shielding it from corrosion and degradation. This physical barrier also impedes direct electron-hole contact within the ferrite, thereby minimizing recombination rates at the surface [228]. The work by Hariani *et al.* [229] on $NiFe_2O_4/SiO_2/NiO$ magnetic nanocomposites revealed significant improvements in the photocatalytic degradation of methyl orange dye under UV irradiation. The study involved the characterization of $NiFe_2O_4$, $NiFe_2O_4/SiO_2$, and $NiFe_2O_4/SiO_2/NiO$ using X-ray Diffraction (XRD), which revealed specific peaks corresponding to their crystalline structures, indicating successful synthesis and coating processes (**Figure 3**). The optical characteristics were examined through UV-Vis Diffuse Reflectance Spectroscopy (DRS), revealing that the band gap values for $NiFe_2O_4$, $NiFe_2O_4/SiO_2$, and $NiFe_2O_4/SiO_2/NiO$ were 1.81, 2.21, and 2.67 eV, correspondingly. The composite demonstrated a remarkable degradation efficiency of 95.76% for methyl orange dye under optimal conditions, which comprised a pH of 4, a catalyst dosage of 0.50 g/L, and 10 mg/L of initial dye concentration.

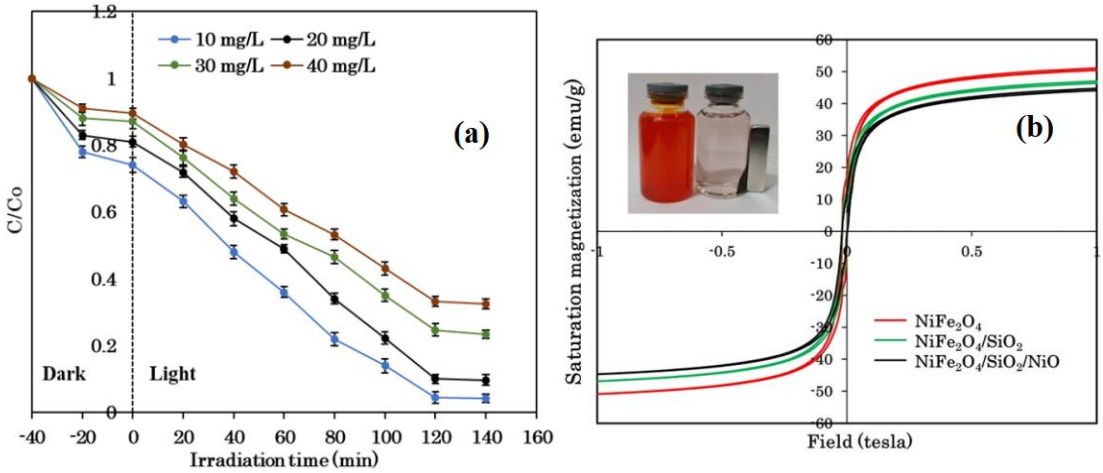

Figure 3 (a) Degradation efficiency at different catalyst dosages and (b) Magnetic properties of prepared samples open access [229].

The magnetic properties of $NiFe_2O_4/SiO_2/NiO$ decreased due to the coating of nonmagnetic SiO_2 on $NiFe_2O_4$, which weakened its magnetic field. Despite this, after being used in the photocatalytic degradation process, the material could still be separated from the solution using a permanent magnet. Even after 5 cycles of recurrent use, $NiFe_2O_4/SiO_2/NiO$ retained good catalytic efficacy, demonstrating that it is an efficient and reusable photocatalyst. The presence of the SiO_2 interlayer improved charge separation, resulting in higher photocatalytic performance compared to composites without the interlayer.

A study conducted by Kumar *et al.* [230] concentrated on the photocatalytic degradation of 2 azo dyes, Methyl Red (MR) and Methyl Orange (MO), utilizing Fe_3O_4, Fe_3O_4/SiO_2, and $Fe_3O_4/SiO_2/Ru$ hybrid magnetic composites in the presence of visible light. Photoluminescence (PL) spectral analysis was performed to assess the efficacy of charge carrier trapping, migration, transfer, separation, and recombination mechanisms within the nanocatalysts. The $Fe_3O_4/SiO_2/Ru$ HMCs exhibited a reduced PL intensity when compared to pure Fe_3O_4 and Fe_3O_4/SiO_2, signifying a diminished likelihood of recombination and enhanced photocatalytic performance. Vibrating sample magnetometry (VSM) investigations revealed the super-paramagnetic characteristics of the HMCs along with a reduction in magnetization attributed to the diamagnetic contribution from the silica shell and the Ru nanoparticles. Under visible light, Fe_3O_4/SiO_2@Ru generates electron-hole pairs. Water reacts with holes to produce ·OH radicals, while electrons reduce oxygen to

form ·O2−. These radicals degrade azo dyes into CO_2 and H_2O. This is clearly depicted in **Figure 4**. The optimal conditions for the Fe_3O_4/SiO_2@Ru photocatalyst are a catalyst dosage of 0.8 g/L, 10 mg/L of initial dye concentration, and a pH of 4, achieving degradation percentages of 95% for methyl orange and 91% for methyl red when irradiated for 150 min under visible light.

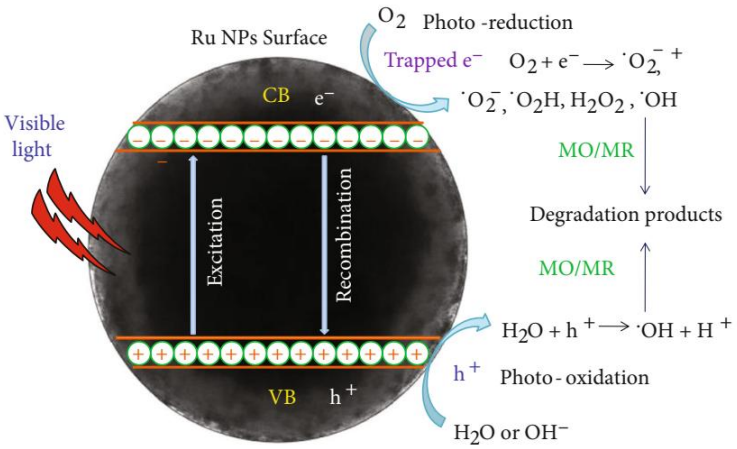

Figure 4 Mechanism of MO/MR dye degradation through photocatalysis by Fe_3O_4@SiO_2@Ru hybrid magnetic composites open access [230].

The Fe_3O_4/SiO_2/Ru HMCs maintain over 90% degradation efficiency even after 6 cycles of use, indicating their stability and durability for repeated applications, which is crucial for practical and sustainable wastewater treatment.

The plasmonic nature of silver nanoparticles (AgNPs) enhances the photocatalytic activity of Ferrite/SiO_2/ hybrid nanocomposites by supporting localized surface plasmon resonances (LSPRs) that improve light absorption and generate hot electrons [231]. Hariani *et al.* [232] synthesized core-shell $Fe_3O_4/SiO_2/TiO_2$ nanoparticles with Ag modification. Fe_3O_4 was coprecipitated and used in the Stöber method to form Fe_3O_4/SiO_2. $Fe_3O_4/SiO_2/TiO_2$ nanoparticles were prepared by dissolving Fe_3O_4/SiO_2 in ethanol, adding titanium tetrabutoxide (TBOT) and ammonia, agitating at 70 °C, isolating, washing and calcining at 350 °C. Ag was impregnated using $AgNO_3$ and $NaBH_4$, followed by washing and vacuum drying to form $Fe_3O_4/SiO_2/TiO_2$@Ag (**Figure 5**). The band gap characteristics of $Fe_3O_4/SiO_2/TiO_2$@Ag were evaluated through the examination of the $(\alpha h\upsilon)^2$ versus $h\upsilon$ graph, revealing TiO2 to be an indirect band gap semiconductor. The $Fe_3O_4/SiO_2/TiO_2$@Ag composite displays an extensive absorption peak within the visible spectrum at wavelengths exceeding 400 nm, whereas TiO_2 presents a pronounced absorption peak in the ultraviolet region at 353 nm.

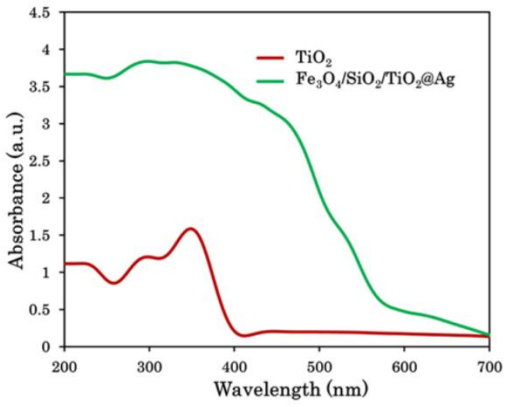

Figure 5 UV-Vis DRS spectra comparison of TiO_2 and $Fe_3O_4/SiO_2/TiO_2$@Ag open access [232].

The energy band gap of $Fe_3O_4/SiO_2/TiO_2$@Ag (2.92 eV) is found to be less than to the band gap associated with TiO_2 (3.24 eV). This indicates that $Fe_3O_4/SiO_2/TiO_2$@Ag exhibits greater efficacy in photocatalytic degradation when subjected to visible light irradiation. The composite exhibits a saturation magnetization of 49.4 emu/g, following the order: Fe_3O_4 > Fe_3O_4/SiO_2 > $Fe_3O_4/SiO_2/TiO_2$ > $Fe_3O_4/SiO_2/TiO_2$@Ag, demonstrating the effect of each layer on magnetic properties. Under optimal conditions (pH 4, 0.5 g/L dosage, 10 mg/L dye concentration, 100 min of irradiation), the composite material demonstrated an exceptionally elevated degradation efficiency, reaching an impressive figure of 96.52% when applied to the decolorization of Congo red dye. It maintains stability with only a 4.83% decline in efficiency after 5 cycles, indicating durability for repeated use. Khan *et al.* [233] found that SiO_2@$CuFe_2O_4$-AgI composites, particularly those containing 15% AgI, outperform pure and other hybrid composites in terms of photocatalytic performance. During methyl orange (MO) degradation, the composite with 15% AgI loading falls 16 times more rapidly than pristine $CuFe_2O_4$ and 8 times faster than pure AgI. The degradation rate of methylene blue (MB) is 18.67 and 9.33 times quicker, respectively. The SiO_2@$CuFe_2O_4$-AgI (15%) composite exhibits an enhanced surface area, a diminished recombination rate of photogenerated electron-hole pairs, expedited separation of photogenerated charge carriers, and an elevated redox capacity, all of which collectively enhance its photocatalytic efficacy.

Electrochemical impedance spectroscopy evaluations were conducted to gain deeper insights into the photoinduced charge transfer mechanisms and capacitance characteristics of various samples. The results indicate that the hybrid ferrite composite, SiO_2@$CuFe_2O_4$-AgI (15%), exhibits the lowest impedance arc compared to pristine AgI, $CuFe_2O_4$, and SiO_2@$CuFe_2O_4$ samples. This implies that the composite exhibits diminished resistance and superior interfacial photoinduced charge transfer efficiencies. Such attributes play a significant role in the augmented photocatalytic efficacy of the photocatalyst. The charge transfer mechanisms of the SiO_2@$CuFe_2O_4$-AgI (15%) photocatalyst under visible light are guided by an S-scheme process. In this mechanism, the conduction band (ECB) electrons of AgI, with a reduction potential of −0.26 V vs. NHE, migrate to the valence band (EVB) of $CuFe_2O_4$. Meanwhile, the EVB holes of AgI, with an oxidation potential of +0.25 V vs. NHE, transfer to the ECB of $CuFe_2O_4$. The conduction band of $CuFe_2O_4$ has a reduction potential of −1.05 V vs. NHE, allowing efficient reduction of O_2 to superoxide radicals ($\bullet O_2^-$), while AgI EVB potential is suitable for oxidizing H_2O to •OH radicals, as shown in **Figure 6**.

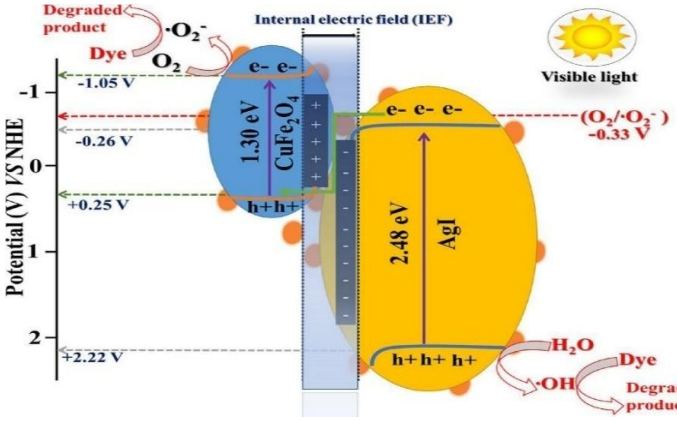

Figure 6 S-Scheme heterojunction mechanism for dye degradation using SiO_2@$CuFe_2O_4$-AgI composite [233].

This S-scheme mechanism enhances charge separation and photocatalytic efficiency, with SiO_2 acting as an electron transporter, reducing recombination rates and improving the overall photocatalytic performance. Furthermore, the hybrid composite exhibits chemical stability and can be reused, retaining its efficacy after ten cycles, thereby rendering it an economically viable alternative for photocatalytic applications. In conclusion, the inclusion of a SiO_2 interlayer in ferrite/SiO_2 composites provides significant

benefits in enhancing photocatalytic activity by improving charge separation and enabling better light penetration. However, optimizing the thickness of the SiO_2 interlayer is crucial. Excessively thick layers can reduce light absorption, increase recombination rates, and introduce diffusion barriers for both the photocatalyst and dye molecules, thereby slowing down the overall photocatalytic process. On the other hand, insufficient thickness may fail to effectively prevent charge recombination, thus potentially decreasing the photocatalytic efficiency of the composite material [234].

Table 2 Photocatalytic performance of various ferrite/SiO_2 composites.

Photocatalyst	Synthesis Method	Contaminant	Light Source	Irradiation Time	Degradation %	Ref.
$CoFe_2O4/SiO_2$	Co-precipitation	Methylene Blue	UV	2 h	80.6	[235]
$CoFe_2O_4$/ PVA-SiO_2	Sol gel	RhB	Visible	4 h	97	[236]
$CoFe_2O_4@SiO_2@Dy_2Ce_2O_7$	Combustion/Sol-gel	Methylene Blue	UV	30 min	94.5	[237]
$Fe_2O4/SiO_2/NiO$	Hydrothermal	Methylene Blue	UV	100 min	98.51	[238]
Fe_3O_4-TiO_2-SiO_2	Sol-gel	Methylene Blue	Halogen lamp	2h	98	[239]
$Fe_3O_4/SiO_2/TiO_2$	Co-precipitation	Methyl orange Methylene blue	UV	5 h	90.2 100	[240]
$Fe_3O_4/SiO_2/TiO_2@Ag$	Stober Method	Congo Red	Visible	100 min	96.52%	[232]
$Fe_3O_4/SiO_2/TiO_2$-Ag	Solvothermal/ Modified Stober	RhB	UV	10 min	100%	[241]
$Fe_3O_4/SiO_2@Ru$	Multistep Wet Chemical process	Methyl orange Methyl red	Visible	150 min	95 91	[230]
$NiFe_2O_4/SiO_2/NiO$	Sol-gel	Methyl Orange	UV	2 h	95.76%	[229]
Ni-Cu-Zn ferrite@SiO_2@TiO_2@Ag	sol-gel method.	Methylene Blue	35-W Xe arc lamp	6 h	83.9%	[242]
$ZnFe_2O_4@SiO_2@TiO_2$	Sol-gel	Methylene Blue	visible	2 h	95.1%	[243]
$ZnFe_2O_4$/ SiO_2/TiO_2	Hydrothermal	Etodolac	Stimulated solar light	20 min	100%	[244]
$ZrFe_2O_4@SiO_2$-NH-TCPP	Hydrothermal/Stober	Methyl Orange	10 W LED lamp	1 h	100%	[245]

Zinc oxide (ZnO)/ ferrites

Zinc oxide (ZnO) is a widely studied semiconductor material known for its significant photocatalytic potential, particularly in the degradation of organic pollutants. Its high surface area, efficient charge transport, and superior photosensitivity make it an attractive candidate for photocatalysis [246]. ZnO can degrade a wide range of organic pollutants,

including dyes, antibiotics, pesticides, and analgesics, and has been well-documented, highlighting its potential in wastewater treatment [247]. The material's photocatalytic activity is primarily driven by its large band gap of approximately 3.3 eV, which allows it to absorb ultraviolet (UV) light and generate electron-hole pairs necessary for the degradation process [248,249]. However, ZnO's photocatalytic efficiency is hindered by several limitations. One major drawback is its inability to fully utilize the solar spectrum, as it predominantly absorbs UV light, which constitutes only about 4% of the total solar radiation [250]. Furthermore, ZnO has an increased recombination tendency for photogenerated electron-hole pairs, considerably reducing its photocatalytic efficacy [251]. Several ways have been used to circumvent these restrictions, including doping with metals and nonmetals, producing heterostructures, and merging ZnO with other materials like graphene to promote separation of charge and extend light absorption into the visible range [252,253].

The formation of ZnO-based heterostructures with narrow bandgap materials effectively extends the absorption region from UV to visible light, enhancing photocatalytic performance. A notable example is the spinel ferrite/ZnO composite, which exhibits significant benefits in photocatalysis, making it highly effective for environmental remediation and energy applications. For instance, Saidi *et al.* [254] synthesized ZnO/$ZnFe_2O_4$ nanocomposites via a hydrothermal method, producing ZF-600 and ZF-700 samples by annealing at 600 and 700 °C, respectively. The band gap values were determined to be approximately 2.2 eV for ZF-600 and 2.1 eV for ZF-700, both lower than pure ZnO (3.37 eV), indicating enhanced suitability for visible light applications. Absorption spectra revealed effective visible light absorption for both samples, with ZF-600 exhibiting higher absorption due to its smaller crystallite size compared to ZF-700.

Sonia *et al.* [255] successfully synthesized $ZnFe_2O_4$-ZnO nanocomposites via a hydrothermal method for photocatalytic degradation of contaminants. These nanocomposites exhibited tunable band gaps (1.73 - 1.88 eV) influenced by ZnO content, promoting visible light absorption. HRTEM confirmed their spherical morphology while VSM analysis revealed magnetic properties for easy post-treatment recovery. The 1:4 $ZnFe_2O_4$-ZnO (ZZ14) composite demonstrated the highest efficiency (88% RB dye degradation in 90 min) and good reusability over multiple cycles, highlighting their potential for practical and sustainable photocatalytic applications. The p-type ZnFe2O4 and n-type ZnO in $ZnFe_2O_4$/ZnO nanocomposites form a type-II p-n heterojunction because $ZnFe_2O_4$ has a more negative conduction band (CB) and valence band (VB) than ZnO. UV irradiation causes both materials to absorb photons, resulting in electron-hole pairs in which electrons are excited from the VB to the CB. The higher energy of $ZnFe_2O_4$'s CB than that of ZnO enables photoexcited electrons to transfer from $ZnFe_2O4$'s CB to ZnO's CB, while holes migrate from ZnO's VB to $ZnFe_2O_4$'s VB, resulting in effective charge separation and superior degrading capabilities.

Undoped ZnO is primarily diamagnetic [256,257], but its magnetic properties can be influenced by factors such as particle size, morphology [258-260], and lattice deformation [256,261]. In contrast, ferrite/ZnO composites exhibit significantly enhanced magnetic properties due to the inclusion of inherently magnetic spinel ferrites. These increased magnetic properties allow for the easy recovery and reuse of the photocatalyst using magnetic separation techniques, boosting the efficiency and sustainability of the photocatalytic process. Hamed *et al.* [262] employed solid-state and sol-gel methods to synthesize ZnO/$NiFe_2O_4$ hetero nanocomposites with different weight percentages of NF (0%, 5%, 10%, 15%, 20%, and 25%). To obtain hysteresis loops, magnetic characteristics were analyzed with a vibrating sample magnetometer (VSM). The findings indicated ferromagnetic characteristics, with both saturation magnetization (Ms) and coercivity (Hc) varying according to NF content and synthesis method. A positive correlation was observed between NF content and saturation magnetization. Observed values of saturation magnetization are higher for samples prepared via the sol-gel method compared to those prepared via the solid-state method. This enhancement in magnetization is attributed to the migration of Zn ions into the $NiFe_2O_4$ crystal structure, redistributing Fe^{3+} ions from tetrahedral to octahedral sites, which promotes increased magnetization despite the smaller particle size of the S-G samples.

The ZnO content significantly impacts the photocatalytic properties of ferrite/ZnO composites,

enhancing their efficiency in applications such as pollutant degradation. Elshypany *et al.* [263] synthesized Fe_3O_4/ZnO nanocomposites via a solid-state reaction method with varying ZnO content. The nanocomposites (MZ1, MZ2, MZ3, MZ4, MZ5) were synthesized by mixing Fe_3O_4 and ZnO in ratios of 0.2:1, 0.4:1, 0.6:1, 0.8:1 and 1:1. X-ray diffraction (XRD) and Raman spectroscopy validated the effective synthesis, which produced distinct ZnO and Fe_3O_4 peaks. UV-Vis diffuse reflectance spectroscopy (DRS) revealed a band gap redshift in Fe_3O_4/ZnO compared to pure ZnO, whereas photoluminescence (PL) spectra revealed decreased electron-hole recombination. Photocatalytic efficiency against methylene blue (MB) under visible light showed MZ4 exhibited the highest activity, followed by MZ3, MZ2, MZ5, and MZ1, as determined by pseudo-first-order kinetics.

These studies collectively highlight the potential of ferrite/ZnO composites for high efficiency photocatalysis in environmental applications, attributed to their synergistic properties and structural enhancements. **Table 3** illustrates the photocatalytic activity of ferrite/ZnO composites and hybrids against various contaminants.

Table 3 Photocatalytic performance of various ferrite/ZnO composites.

Photocatalyst	Synthesis method	Contaminant	Light source	Irradiation time	Degradation percentage	Ref.
Fe_3O_4/ZnO (0.8:1)	Solid state	methylene blue	Visible light	2h	88.5	[263]
Fe_3O_4-ZnO:V	co-precipitation, seed-mediated growth	rhodamine B (RhB)	UV	300 min	95	[264]
$CaFe_2O_4$-ZnO	sonochemical assisted co-precipitation	rhodamine B (RhB)	Visible	140 min	97.5	[265]
$CoFe_2O_4$/ZnO	Sol gel Hydrothermal coprecipitation	Nitrobenzene (NB)	UV	60 min	100	[266]
$CoFe_2O_4$@ZnO (1:5)	Co-precipitation method	Methylene blue (MB)	UV	180 min	78.3	[267]
ZnO/$MnFe_2O_4$	Co-precipitation	Methylene blue (MB)	Visible	50 min	93.2	[268]
ZnO/$MnFe_2O_4$	Co-precipitation and hydrothermal	rifampicin	UV	90 min	94.72%	[269]
$NiFe_2O_4$/ZnO	Solid state	Coomassie blue G-250	UV and Visible	30 min	96.90% and 68.55%	[270]
$NiFe_2O_4$/ZnO	Hydrothermal	Congo Red	Stimulated solar light	10 min	94.55	[271]
ZnO/$NiFe_2O_4$	co-precipitation	Methylene blue	visible	40 min	92	[272]
ZnO/$ZnFe_2O_4$	Hydrothermal method	Rhodamine B	Sunlight	3h	95.6	[273]
Ni-Zn Ferrite/ZnO nanorods	hydrothermal	Rhodamine B	UV	10 min	≈ 100%	[274]

MXenes/ ferrites

MXenes are a class of 2-dimensional nanostructures characterized by the general formula $M_{n+1}X_nT_x$, where M refers to an early transition metal (such as Ti, Nb, Mo, V, Zr, Sc, Hf, W), X signifies carbon and/or nitrogen, and Tx represents surface terminations including -O, -OH, and -F. The structure of MXenes is derived from their corresponding MAX (or $M_{n+1}AX_n$) phases, which have a layered structure consisting of M-X layers interleaved with A layers (where A is typically aluminum). By means of selective etching of the A (elements from groups 13 or 14, such as Al, Si, Ga) layers, MXenes are synthesized, preserving a layered architecture characterized by transition metal carbide or nitride sheets interspersed with surface terminations [275]. MXenes' uncommon structure and bonding play a crucial role in their photocatalytic properties. The 2-dimensional structure has a large surface area, which allows for more active sites in photocatalytic reactions. The existence of hydrophilic functional groups (such as OH- and O-) across the MXene surface improves its dispersibility in aqueous solutions and interaction with reactants. Furthermore, MXenes' high electrical conductivity facilitates efficient charge transport, which is critical for minimizing electron-hole recombination in photocatalysis [276,277].

MXenes can serve as excellent electron acceptors and co-catalysts, promoting effective charge separation and transfer. The surface termination group have been found to provide optimal catalytic sites, enhancing the overall photocatalytic efficiency [278-280]. The formation of heterojunctions with MXenes broadens the light absorption window from visible to near-infrared (NIR) [281], crucial for efficient solar energy utilization, and improves interfacial charge transfer and separation by forming a Schottky junction to enhance charge separation and increase the production of reactive oxygen species [282]. The complimentary coupling of ferrite and MXene in heterostructures improves photocatalytic performance (**Table 4**) by facilitating charge separation and increasing light absorption, addressing the inherent limits of each material in its pure state. Alsafari *et al.* [283] compared the photocatalytic performance of $CuFe_2O_4$/MXene nanohybrids with pristine $CuFe_2O_4$, demonstrating significantly enhanced activity. Copper ferrite ($CuFe_2O_4$) was synthesized by mixing iron nitrate ($Fe(NO_3)_3$) and copper nitrate ($Cu(NO_3)_2$) in deionized water with citric acid, followed by heating, drying, and annealing. MXene (Ti_3C_2) was prepared by etching Ti_3AlC_2 in hydrofluoric acid, followed by washing, intercalation with DMSO, and ultrasonication. The $Ti_3C_2/CuFe_2O_4$ nanohybrids were fabricated by mixing and sonication, with subsequent drying. SEM analysis revealed distinct morphologies: the MAX phase had a closely packed surface, while MXene showed an accordion-like structure, and $Ti_3C_2/CuFe_2O_4$ nanohybrids exhibited copper ferrite intercalation preventing restacking. FTIR confirmed functional groups such as Ti–O, C–F, and C=O. The photocatalytic degradation of methylene blue (MB) was examined under visible light. The $CuFe_2O_4$/MXene nanohybrids achieved 94% degradation in 60 min, 4.5 times higher than pristine $CuFe_2O_4$. The enhanced performance is attributed to the direct Z-scheme mechanism, where $CuFe_2O_4$ generates charge carriers under light and MXene's narrow bandgap facilitates electron-hole recombination. Electrons from $CuFe_2O_4$ recombine with MXene's holes, with MXene serving as a hole reservoir. These electrons react with oxygen to produce superoxide radicals, leading to hydroxyl radicals that degrade MB. Electrochemical impedance spectroscopy (EIS) demonstrated that the nanohybrids have decreased charge transfer resistance, which improves electron-hole separation and hence increases photocatalytic efficiency. The magnetic characteristics of the nanohybrids also helped in separation and reusability. The photocatalytic performance of various Ferrite/MXene Composites is given in **Table 4**.

Table 4 Photocatalytic performance of various ferrite/MXene composites.

Photocatalyst	Synthesis method	Contaminant	Optimum dosage	Light source	Degradation %	Ref.
$CuFe_2O_4/Ti_3C_2$	Ultrasonication	Methylene Blue	Photocatalyst dosage (P) = 0.05 g, Initial Dye Concentration (D) = 15 mg/L, time (T) = 60 min	Visible	94%	[283]
$CuFe_2O_4/Ti_3C_2$	Sol-hydrothermal	Sulfamethazine (SMZ)	P = 25 mg, D = 40 mg/L, T = 60 min	Visible	59.40%	[284]
$Mg_{0.6}Zn_{0.2}Co_{0.2}Fe_2O_4$/ MXene	Micro-emulsion	Congo-red	P = 30 mg, D = 50 ppm, pH = 6 T = 140 min	Bulb (200 W)	78.23%	[285]
$BiFeO_3$ /Ti_3C_2	Sol-gel followed by chemical etching	Acetophenone	P = 100 mg, D = 30 ppm, T = 150 min	Xenon lamp of 300 W	100%	[286]
		Congo Red	P = 100 mg T = 42 min		100%	
$MnFe_2O_4/Ti_3C_2T_x$	Hydrothermal	Tetracycline	P = 100 mg/L, D = 10 mg/L, H_2O_2 dose = 0.4 mL, pH = 3, T = 60 min	Visible	93.80%	[287]
TiO_2/Ti_3C_2/ $MnFe_2O_4$	Ultrasonic-assisted self-assembly approach	Carbamazepine	P = 2 g/ dm^3, D = 7 mg/dm^3, pH = 3, PMS Concentration = 0.25 mM T = 20 min	300 W, Xe lamp	100%	[288]
		Ibuprofen	P = 0.05 g, D = 10 mg/dm^3, pH = 3, PMS Concentration = 0.25 mM T = 10 min		100%	
$NiFe_2O_4$/MXene	Co-precipitation followed by ultrasonication	Methylene Blue	T = 70 min	Visible	74%	[289]
Delaminated $Ti_3C_2/NiFe_2O_4/V_2O_5$	Thermal Decomposition followed by HF-etching	Rhodamine B	P = 0.5 mg/mL, D = 10 mg/L pH = 12, T = 4 h	150 W LED	88.70%	[290]
$TiO_2@Ti_3C_2T_x@ZnFe_2O_4$	Sol-gel followed by ultrasonication	Methylene blue	P = 0.05 g, D = of 20 mg/L (30 cc), T = 2 h	300 W Xe lamp	100%	[291]
$Ti_3C_2/ZnFe_2O_4$ (Persulphate activation)	Hydrothermal	Tetracycline	P = 0.05 g D = 30 mg/L PS dosage = 0.75 g/L, T = 1 h	120 W LED lamp	87%	[292]

In a similar study, Cao *et al.* [284] studied the effect of Ti_3C_2 content on CFO/Ti_3C_2 heterojunction photocatalysts with Ti_3C_2 to $CuFe_2O_4$ 10%, 12%, and15% for SMZ photodegradation under visible light. Ti_3C_2 sheets were produced by treating 0.5 g of Ti_3AlC_2 with 70% HF, followed by washing and vacuum drying. For the composite, 0.065 mmol of Ti_3C_2 was dispersed in water, sonicated, mixed with $CuCl_2$•$2H_2O$ and $FeCl_3$•$6H_2O$, and stirred at pH 10 and 85 °C. This mixture was autoclaved at 120 °C for 12 h. The resulting precipitate was filtered, washed, and vacuum dried, yielding a $CuFe_2O_4/Ti_3C_2$ composite. Diffuse reflection spectroscopy (DRS) shows that both CFO and CFO/Ti_3C_2 have increased light absorption in the 200 - 400 nm range, with Ti_3C_2 shifting the absorption edge and enhancing absorption between 350 - 550 nm. The band gaps (Eg) are 0.63 eV for Ti_3C_2, 1.43 eV for CFO, and approximately 1.32 eV for the CFO/Ti_3C_2 hybrid, with the latter's reduction in Eg indicating improved photocatalytic activity due to defect or impurity introduction. Photoluminescence (PL) analysis reveals that the CFO/Ti_3C_2 hybrid exhibits reduced PL intensity compared to CFO alone, suggesting that the hybrid structure promotes more effective separation of photogenerated electron-hole pairs, enhancing its photocatalytic efficiency. CFO/Ti_3C_2 demonstrated superior performance, achieving a degradation rate constant of 0.0128 min^{-1}, significantly higher than CFO's 0.00144 min^{-1}. CFO/Ti_3C_2 maintained effective degradation across 3 cycles, whereas CFO showed weaker stability. The enhanced degradation mechanism of the CFO/Ti_3C_2 hybrid is attributed to its effective electron transfer and high photocatalytic activity. Ti_3C_2 with its metallic properties, facilitates rapid electron

transfer and traps photoexcited electrons, reducing recombination. This interaction between CFO and Ti_3C_2 leads to an increased generation of reactive species like •OH and h+, which are crucial for the efficient breakdown of SMZ. The valence band potential of Ti_3C_2 (0.33 eV) being higher than CFO (0.31 eV) enables effective charge separation, while the conduction band potential of Ti_3C_2 (−0.30 eV) supports better electron trapping compared to CFO (−1.12 eV). Consequently, the CFO/Ti_3C_2 hybrid exhibits superior photocatalytic performance, achieving a 59.4% degradation rate of SMZ and promoting the formation of small organic molecules and eventual mineralization into CO_2 and H_2O.

Mesoporous architectures markedly improve the efficiency of photodegradation processes by offering an extensive specific surface area, adjustable pore dimensions, and elevated interparticle connectivity. Concurrently, Schottky heterostructures contribute to the enhancement of photocatalytic efficacy by facilitating charge separation and the generation of reactive oxygen species [293]. Tehrani *et al.* [291] studied the effect of varying MXene and $ZnFe_2O_4$ content on the photodegradation ability of mesoporous TiO_2@$Ti_3C_2T_x$ MXene@$ZnFe_2O_4$ composites. The synthesized TiO_2@$Ti_3C_2T_x$ MXene@$ZnFe_2O_4$ composite materials by sonicating 20 mL of $Ti_3C_2T_x$ MXene slurry (with DI water) in an ultrasonic bath (40 kHz, 150 W) for 30 min. Following, 20 mg of TiO_2 nanopowder and various concentrations of $ZnFe_2O_4$ nanoparticles were incorporated in the solution, which was then sonicated for another 30 min. The mixes were heated to 70 °C to produce the final products. Among various composites tested, the TM20ZF50 (0.005 g Zn, 20 cc $Ti_3C_2T_x$ MXene solution) variant exhibited the highest performance, achieving a 100% degradation rate of MB solution in 2 h, highlighting its superior photocatalytic activity. The proposed mechanism for the TiO_2@$Ti_3C_2T_x$ MXene@$ZnFe_2O_4$ photocatalyst involves hybrid/Schottky heterostructures and $Ti_3C_2T_x$ as an electron mediator. With band gaps of 3.2 eV for TiO_2 and 1.9 eV for $ZnFe_2O_4$, the photogenerated electrons transfer to $ZnFe_2O_4$ nanoparticles while holes move to TiO_2, forming a type-II heterostructure that enhances electron-hole separation. $Ti_3C_2T_x$ MXene's high conductivity and narrow band facilitate electron migration and form a Schottky barrier at the $Ti_3C_2T_x$@$ZnFe_2O_4$ interface, preventing electron backflow. This leads to the production of superoxide radicals and hydroxyl radicals, furthering the oxidation process and inhibiting electron-hole recombination. $Ti_3C_2T_x$, which acts as a co-catalyst and electron sink, promotes charge transfer and O_2 adsorption, hence improving photogenerated charge separation and radical formation. The addition of Schottky-Z-scheme/type-II heterostructures to the TiO_2@$Ti_3C_2T_x$MXene@$ZnFe_2O_4$ composite improves photocatalytic performance. Additionally, the filter retained 95% of its efficiency after 60 days, demonstrating excellent long-term stability.

The activation of persulfate (PS) markedly boosts photocatalytic degradation efficiency by producing highly reactive radicals and improving electron-hole separation, resulting in a substantial enhancement in pollutant removal compared to Fenton-like reactions and traditional photocatalytic oxidation alone [294-296]. Wang *et al.* [292] investigated the activation of persulfate (PS) by Ti_3C_2 MXene quantum dots modified $ZnFe_2O_4$ for the fast degradation of tetracycline. Using a 120 W LED lamp having a wavelength of 450 nm and luminous flux of 1200 LM, they tested 0.05 g of the catalyst in 100 mL of a 30 mg L^{-1} tetracycline solution. The mixture was agitated in the dark to achieve adsorption-desorption equilibrium before adding 0.075 g PS and exposing it to light. The degradation process, monitored every 10 min via UV-VIS spectrophotometry, achieved 87% tetracycline removal within 60 min. This high efficiency is attributed to the abundant active edge sites of the 0D Ti_3C_2 QDs and the formation of a Schottky junction between Ti_3C_2 MXene and $ZnFe_2O_4$, which establishes a Schottky barrier that effectively inhibits the recombination of photogenerated electrons and holes. In the $ZnFe_2O_4$/MXene-PS system under light, tetracycline degradation proceeds via free radical pathways (O_2•$^-$, SO_4•$^-$, and •OH) as well as non-radical mechanisms (h^+ and $^1O_2$) as explained by Eqs. (6) - (13).

$$ZnFe_2O_4/MXene + h\nu \rightarrow ZnFe_2O_4/MXene(e^- + h^+) \quad (6)$$

$$O_2 + e^- \rightarrow O_2^{*-} \quad (7)$$

$$h^+ + O_2^{*-} \rightarrow {}^1O_2 \quad (8)$$

$$Fe(III) + e^- \rightarrow Fe(II) \quad (9)$$

$$Fe(II) + S_2O_8^{2-} \rightarrow Fe(III) + SO_4^{2-} + SO_4^{*-} \quad (10)$$

$$S_2O_8^{2-} + e^- \rightarrow SO_4^{*-} + SO_4^{2-} \quad (11)$$

$$h^+ + H_2O \rightarrow {}^*OH + H^+ \quad (12)$$

$$O_2^{*-} / {}^1O_2 // h^+ / SO_4^{*-} / {}^*OH + \text{tetracycline} \rightarrow \text{degradation products} \quad (13)$$

The $ZnFe_2O_4$/MXene catalyst exhibited exceptional stability and reusability, retaining its structural integrity across 4 cycles as confirmed by X-ray diffraction (XRD) analysis, highlighting its robustness for repeated use. Hence, MXenes presents a highly promising avenue for advanced photocatalytic applications. Their ability to facilitate effective charge separation and transfer, combined with versatile surface functionalization, positions MXenes as potent catalysts for environmental remediation and energy conversion processes. Further research is essential to fully understand and optimize MXene-based photocatalysts for practical environmental applications. Furthermore, addressing issues like scalability, cost-effectiveness, and stability will be critical for their wider adoption.

g-C_3N_4/ ferrite

Graphitic carbon nitride (g-C_3N_4) represents a synthetic polymer predominantly constituted of carbon and nitrogen, accompanied by minor concentrations of hydrogen contaminants. The distinctive tris-triazine framework confers electron-rich characteristics, inherent basic surface functionalities, and the potential for hydrogen bonding, thereby establishing it as a noteworthy substitute for traditional carbon-based materials in a diverse array of applications [297]. It is chemically stable under various conditions, including acidic and basic environments, and is composed of earth-abundant and non-toxic elements, making it environmentally friendly. Its unique chemical and optoelectronic properties have garnered significant attention, particularly in fields such as catalysis and energy [298,299]. The synthesis of g-C_3N_4 can be achieved using various precursors, including urea, dicyandiamide, semicarbazide hydrochloride, and thiosemicarbazide, with each precursor influencing the yield and properties of the resulting g-C_3N_4. This material can be synthesized in different morphologies, such as bulk, nanosheets, nanotubes, and nanodots, each offering distinct structural, morphological, optical, and electrical properties tailored for specific applications [300]. The nanoscale architectures of g-C_3N_4, including nanosheets, nanotubes, nanorods, quantum dots, and hollow spheres, exhibit higher surface areas, an abundance of active sites, and wider band gaps, enhancing their performance in applications like photocatalysis, sensors, and bioimaging. Pure g-C_3N_4 has low photocatalytic performance due to quick electron-hole recombination and a broad band gap (~2.7 eV), which limits visible light absorption. The confinement of electrons and holes within C6N7 units and their Coulomb attraction lead them to recombine fast, preventing redox reactions [301]. Furthermore, as a reduction photocatalyst, g-C_3N_4 generates photogenerated holes in its valence band with weak oxidative power, further limiting its overall photocatalytic performance. Forming a ferrite/g-C_3N_4 heterojunction enhances photocatalytic efficiency by leveraging ferrites' oxidation capabilities and g-C_3N_4's strong reduction ability, resulting in improved charge separation, reduced recombination rates, and extended light absorption range [302].

Ajami *et al.* [303] systematically synthesized $CoFe_2O_4$/g-C_3N_4 (CF/CN) nanocomposites with varying g-C_3N_4 weight percentages (15, 25, 35, 50 and 75 wt%) through ultrasonic dispersion of g-C_3N_4 powder in distilled water followed by co-precipitation of cobalt ferrite onto the g-C_3N_4 nanosheets. The samples, designated as CF/15CN, CF/25CN, CF/35CN, CF/50CN, and CF/75CN, were engineered to evaluate the impact of g-C_3N_4 content on their physicochemical properties and photocatalytic performance. Transmission electron microscopy (TEM) revealed an average particle size of 31 nm for CF and 20 nm for the CF/25CN nanocomposite. Photoluminescence (PL) spectroscopy indicated that CF/25CN exhibited the lowest intensity among the samples (CF, CN, and CF/25CN), signifying enhanced charge carrier separation, which is conducive to superior photocatalytic activity. The incorporation of g-C_3N_4 into CF induced an upward shift in the band gap values, with CF/25CN demonstrating a band gap of 1.73 eV.

Remarkably, CF/25CN achieved 100% degradation of methylene blue (MB) within 180 min at a dosage of 400 mg/L under visible light irradiation, maintaining high stability and over 98% degradation efficiency after 3 recycling cycles. The S-scheme mechanism (**Figure 7**) present in this nanocomposite incorporates g-C_3N_4 functioning as the reduction photocatalyst characterized by a reduced work function of 4.18 eV, while $CoFe_2O_4$ serves as the oxidation photocatalyst exhibiting an elevated work function of 5.3 eV.

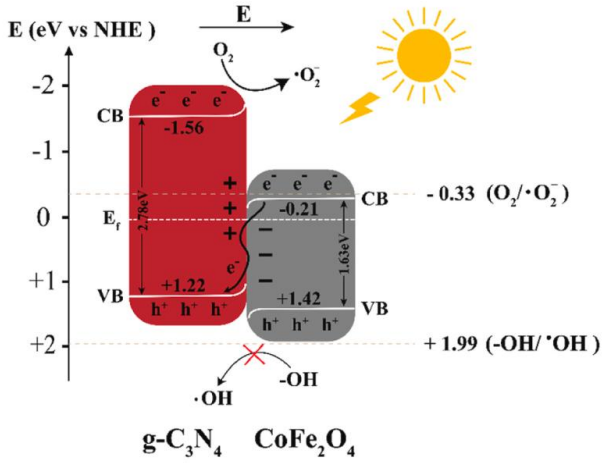

Figure 7 Upon contact, the difference in fermi levels cause electrons to transfer from g-C_3N_4 to $CoFe_2O_4$, creating an internal electric field and resulting in band bending, where the band edge of $CoFe_2O_4$ bends downward and that of g-C_3N_4 bends upward, forming an S-scheme heterostructure [303].

Shenoy *et al.* [304] reported the synthesis of a g-C_3N_4/$CaFe_2O_4$ heterojunction via an in-situ polycondensation approach, where n-type porous g-C_3N_4 nanosheets were grown directly onto p-type $CaFe_2O_4$ particles, resulting in a closely integrated heterojunction with quasi-polymeric characteristics. This structure effectively trapped excited electrons, preventing charge carrier recombination, and significantly improved the degradation rates of ciprofloxacin and phenol compared to unmodified g-C_3N_4. The synthesis of g-C_3N_4 (gCN) nanosheets employed the thermal polycondensation technique, and the $CaFe_2O_4$ (CFO) was prepared using the citrate-nitrate sol-gel method. For the g-C_3N_4/$CaFe_2O_4$ (gCN/CFO) composites, varying amounts of CFO (10 - 100 mg) were blended with 10 g of urea and subjected to calcination at 550 °C for 2 h, using a heating rate of 100 °C min^{-1}. The resulting products were labeled as gCN/CFO10 through gCN/CFO100. Characterization techniques such as PL spectra and photoelectrochemical (PEC) characterizations confirmed efficient interfacial charge transport and separation in the composite. The electron density value of 4.4 eV from energy-resolved distribution of electron trap (ERDT) patterns indicated the formation of a new electron trap state post-heterojunction formation, which is responsible for the enhanced photocatalytic activity. The rates of degradation for ciprofloxacin and phenol when utilizing the optimized gCN/CFO composite increased 2.3 and 2.1 times, respectively, compared to those achieved with pure g-C_3N_4, under visible light exposure. This improvement is attributed to the Z-scheme charge carrier transport route facilitated by the p-n heterojunction, as confirmed by Mott-Schottky measurements and X-ray photoelectron spectroscopy (XPS). Scavenger studies and electron spin resonance (ESR) analysis identified superoxide anion radicals and holes as the primary active species driving the degradation of pollutants. The Z-scheme mechanism facilitates the recombination of photo-generated electrons within $CaFe_2O_4$ and holes present in g-C_3N_4, thereby improving charge separation and transport, which is essential for the effectively harnessing solar energy in the photodegradation of organic pollutants in wastewater.

Reusability and Photostability is crucial for reducing operational costs and ensuring sustainable environmental applications by maintaining catalytic

efficiency over multiple cycles. In a study by Ahmed *et al.* [305], the synthesis of the La-$CuFe_2O_4$/g-C_3N_4 (LCFO/CN) heterojunction photocatalyst was undertaken to augment the photolytic decomposition of Rhodamine B (RhB) dye within aquatic environments. g-C_3N_4 was synthesized from melamine via thermal polymerization, while $La_2Ti_2O_7$ nanosheets were prepared using a hydrothermal method. LCFO nanoparticles and g-C_3N_4 were mixed in water, sonicated for 10 min, and stirred at 60 °C for 2 h. The suspension underwent a filtration process, followed by washing, and subsequently dried at a temperature of 140 °C for a duration of 12 h, and ground to obtain the LCFO/CN (8:2) composite. Various characterization methods confirmed the successful attachment of LCFO on CN sheets, which is crucial for the formation of the heterojunction structure. The assessment of photocatalytic efficacy was conducted through the degradation of RhB dye, wherein the LCFO/CN heterojunction photocatalyst demonstrated an exceptional photodegradation efficiency of 97.35%, markedly surpassing that of pristine CFO (62.73%) and LCFO (67.13%) under consistent reaction parameters. In the LCFO/CN type II heterojunction, both photocatalysts are activated under visible light due to their low bandgaps, generating electron-hole pairs. Electrons from LCFO's lower conduction band (−1.18 V) transfer to the conduction band (-0.58 V) of CN, while holes in CN's valence band (2.31 V) oxidize −OH or H_2O into •OH radicals. The conduction band potential of LCFO is sufficiently negative to facilitate the reduction of surface O_2 to O_2•− radicals. The main active species (•OH, O_2•−, h^+) drive the degradation of RhB dye into H_2O and CO_2. The LCFO/CN nanocomposite demonstrated excellent photostability and reusability, with only a minor loss of 4.83% in photodegradation efficiency after 55 successive cycles. Additionally, the leaching of Cu in the solution was minimal, and SEM analysis showed no significant morphological changes in the catalyst after repeated use, indicating its superior stability. XRD and FTIR results further confirmed the absence of noticeable phase changes in the LCFO/CN catalyst even after multiple cycles, validating its potential for practical applications in industrial wastewater treatment. The saturation magnetization value (29.22 emu/g) of the LCFO/CN photocatalyst also indicated that it could be easily separated from the reaction mixture using external magnets, underscoring its practical utility.

The incorporation of GO into photocatalytic systems enhances their performance by leveraging its 2-dimensional structure, high conductivity, superior electron mobility, and large specific surface area [306]. Farhang *et al.* [307] synthesized g-C_3N_4/GO/$ZnFe_2O_4$ nanocomposite using hydrothermal technique to evaluate its photocatalytic and biomedical potential. g-C_3N_4, GO, and $ZnFe_2O_4$ (1:1:1) were mixed in ethanol/water, sonicated, and sealed in an autoclave at 180 °C for 9 h. After cooling, the product was washed and prepared for characterization and applications. Morphological analysis using FE-SEM and TEM images reveals that $ZnFe_2O_4$ nanoparticles, with an average size of 20 - 30 nm, are uniformly distributed on the surface of g-C_3N_4 and GO sheets, forming a layered structure. The nanocomposite's BET-specific surface area, as determined by nitrogen adsorption-desorption analysis, is measured at 68.24 m^2/g. PL spectroscopy reveals that the g-C_3N_4/GO/$ZnFe_2O_4$ composite has reduced PL intensity, indicating effective suppression of electron-hole recombination and enhanced charge carrier separation. The formation of the g-C_3N_4/GO/$ZnFe_2O_4$ composite significantly reduces the band gap from 2.5 eV for g-C_3N_4 and 2.6 eV for GO to 1.2 eV, indicating enhanced light absorption capabilities. The photocatalytic properties of the g-C_3N_4/GO/$ZnFe_2O_4$ nanocomposite were evaluated by degrading methylene blue (MB) dye. The composite achieved a remarkable 98% degradation efficiency within 60 min under light conditions, while only 3.7% degradation occurred in dark conditions, demonstrating its high photocatalytic activity. The enhanced performance is attributed to the formation of electron-hole pairs facilitated by the heterojunction structure, where GO acts as an electron acceptor, improving the adsorption capacity and lifespan of charge carriers, and $ZnFe_2O_4$ aids in charge separation and reusability. Practical factors such as pH, concentration, dosage, and scavenger were optimized, with the best results obtained at pH 10, 20 mg/L concentration, 0.3 g/L dosage, and using EDTA as a scavenger.

Table 5 Photocatalytic performance of various ferrite/g-C_3N_4 composites.

Photocatalyst	Synthesis method	Contaminant	Optimum dosage	Light Source	Degradation (%)	Ref.
$BiFeO_3/gC_3N_4$	Hydrothermal followed by Electrospinning	Tetracycline (TC) Rhodamine B (RhB)	Photocatalyst Dosage (P) = 20 mg, Contaminant Concentration (C) = 50 mL TC (10 mg/L) or RhB (20 mg/L), Time (t) = 150 min for TC and 180 min for RhB	LED light (42 mW/cm^2)	94% 88%	[308]
$CaFe_2O_4$/ gC_3N_4	Polycondensation	Ciprofloxacin Phenol	P = 1 g/L, C =10 ppm, t = 30 min P = 1 g/L, C =10 ppm, t = 130 min	Xe lamp (500 W)	100% 100%	[304]
g-C_3N_4/$CoFe_2O_4$	Calcination and co-precipitation	Methylene blue (MB)	P = 100mg, C = 5 mg/L, pH = 8 t = 180 min	Sunlight	97.40%	[309]
g-C_3N_4/$CoFe_2O_4$	Thermal exfoliation and Co-precipitation	Methylene blue (MB)	P = 400 mg/L C = 2 mg/L, t = 180 min	Visible (OSRAM, 150 W)	100%	[303]
$Ce_{0.2}Co_{0.8}Fe_2O_4$/g-C_3N_4	Hydrothermal	Rhodamine B (RhB)	P = 0.4 g/L, C = 20mg/L, pH = 7, t = 60 min	200 W tungsten filament lamp	90.27%	[310]
Co-$ZnFe_2O_4$@S-GCN	Hydrothermal	Methylene blue (MB)	55% S-GCN@6.5% CoZF, t = 120 min	Solar Light	93%	[311]
$CoCrCuFe_2O_4$@gCN	Sol-gel followed by Ultrasonication	Crystal violet (CV) Congo red (CR) Methyl Orange (MO) MB	P = 30 mg/L, C = 7 ppm t = 135 min C = 8 ppm C = 4 ppm C = 30 ppm	Sunlight	90.20% 90.10% 92.20% 91.10%	[312]
$CuO/CuFe_2O_4$/g-C_3N_4 (PS activation)	calcination	tetracycline (TC)	P = 0.1 g/L, C = 0.02g/L, PS concentration = 1 mmol/L, pH = 3, t = 30 min	Xe lamp (300 W)	99%	[313]
$Cux Ni_{0.5}$-$Co_{0.5}Fe_2$-xO_4@g-C_3N_4	Co-Precipitation followed by Ultrasonication	Rhodamine B (RhB) pendimethalin (PDM)	t = 105 min	Sunlight	92% 86%	[314]
g-C_3N_4/Fe_3O_4/ ZnO	Ultrasonication	Oxytetracycline (OTC)	P = 0.15g/L, C = 20 ppm, t = 2h	100W Visible Lamp	83%	[315]
La-$CuFe_2O_4$/g-C_3N_4	Hydrothermal	Rhodamine B (RhB)	P = 0.4 g/L, C = 30 mg/L, pH = 6, t = 48 min	200 W tungsten filament lamp	97.35%	[305]
$CuSm_{0.06}Fe_{1.94}O_4$@g-C_3N_4	Hydrothermal	Methyl Orange (MO)	P = 1,000 mg/L, C = 10 ppm (120 mL) pH = 3.5, ammonium persulphate (APS) = 40 mg, t = 90 min	Visible (5W LED)	95.70%	[316]
g-C_3N_4/Ti_3C_2/$MnFe_2O_4$ (PMS Assisted)	Solvothermal followed by calcination	Naphthalene (NAP)	P = 0.3 g/L, C = 1.0 mg/L, pH = 6.8, PMS Conc.= 1 mmol/L, amounts of Ti_3C_2 = 10 mg, t = 45 min	Visible Light	100%	[317]

Photocatalyst	Synthesis method	Contaminant	Optimum dosage		Light Source	Degradation (%)	Ref.
g-C_3N_4/ $NiFe_2O_4$ (Photo-Fenton)	Impregnation calcination technique	Tetracycline (TC)	P = 150 mg, C = 20 mg/L (300 mL) t = 60 min		500 W Xe lamp	96.47%	[318]
VFe_2O_4@g-C_3N_4	Hydrothermal	sulfamethoxazole (SUF)	P = 0.12 g/L, C = 10mg/L, pH = 7,	t = 160 min	Visible (xenon, 150 W)	100	[319]
		Ciprofloxacin (CIP)		t = 170 min		94	
		erythromycin (ERY)		t = 160 min		90	
g-C_3N_4/GO/ $ZnFe_2O_4$	Hydrothermal	Methylene blue (MB)	P = 30 mg/100 mL, C = 20 mg/L, t = 60 min		250-W mercury lamp	98%	[307]
KPCN/GO/$ZnFe_2O_4$	Hydrothermal	Rhodamine B (RhB)	P = 60 mg/mL, C = 20 micromolar (μM)	t = 30 min	Visible	96	[320]
		Methylene blue (MB)	in 100 mL water	t = 120 min		93	

Challenges and perspectives

Despite the significant progress in the development of spinel ferrites and their hybrid systems as photocatalysts, several critical limitations continue to impede their real-world application in wastewater treatment. At the material level, their photocatalytic efficiency remains restricted by rapid recombination of photogenerated electron-hole pairs, leading to reduced quantum yields and slower degradation rates. Various strategies such as doping and coupling with semiconductors like TiO_2, ZnO, g-C_3N_4, SiO_2, and MXene have shown potential to address these limitations; however, they often introduce new complications. For example, TiO_2-ferrite hybrids can suffer from poor band alignment that promotes recombination rather than effective charge separation, while SiO_2 hybrids, although improving dispersion, may dilute active sites and reduce catalytic activity. ZnO-based systems are vulnerable to photocorrosion and exhibit instability under variable pH conditions. Meanwhile, g-C_3N_4 and MXene hybrids, though offering enhanced visible light absorption and improved charge carrier mobility, often compromise the magnetic properties essential for easy catalyst recovery, thereby complicating post-treatment separation processes.

In addition to intrinsic material challenges, laboratory studies typically rely on simplified synthetic wastewater containing single pollutants, which does not reflect the complexity of actual industrial or municipal effluents. Real wastewater contains a mix of natural organic matter, various ions, suspended solids, and multiple organic and inorganic pollutants. These components compete for reactive species, block active sites, reduce light penetration, and can destabilize the catalyst. Scavenging species such as carbonate, chloride, and sulfate ions reduce the availability of photogenerated radicals, while organic matter and high turbidity hinder the light-driven activation of the photocatalyst. Furthermore, the aggressive chemical environment and extended exposure times required for treating real effluents can lead to degradation of the photocatalyst itself, including leaching of metal ions and structural breakdown at the hybrid interfaces.

From an engineering standpoint, most reported systems operate at catalyst loadings too high for economic scalability, and immobilized systems, while aiding recovery, typically suffer from mass transfer limitations and reduced activity. Reactor designs that take advantage of ferrites' magnetic properties remain underexplored, despite potential benefits such as enhanced mixing and catalyst retention. The reliance on artificial UV light sources further adds to energy demands, challenging the feasibility of large-scale implementation. Moreover, environmental and toxicological impacts of these materials remain largely unaddressed. Although ferrites are generally seen as low-toxicity alternatives, their long-term behavior in aquatic systems, especially when used in hybrid configurations, is not well understood. There is a lack of standardized toxicity testing and insufficient data on

chronic exposure effects, limiting both regulatory approval and public acceptance.

To overcome these barriers, future research should focus on multifunctional material designs that retain magnetic properties while improving photocatalytic efficiency, such as core-shell structures, single-atom catalysts, and defect-engineered systems. Hybrid systems require careful interface engineering to ensure band alignment and structural stability, especially in complex wastewater environments. Standardized testing protocols using real effluents, long-term performance evaluations, and comprehensive environmental assessments, including life cycle analysis and catalyst recyclability, are essential. Reactor innovations that leverage magnetic properties for continuous operation and integration with solar energy can enhance sustainability. Finally, collaborative efforts between academia, industry, and regulatory bodies are needed to establish clear safety standards, pilot-scale validations, and commercialization pathways that support the practical deployment of ferrite-based photocatalytic systems.

Conclusions

Ferrite-based photocatalysts have demonstrated remarkable potential for the degradation of contaminants in wastewater under visible light. Transition metal doping, especially with elements like Co, Ni, and Mn, has effectively narrowed ferrites' band gaps, enhanced visible light absorption and significantly improving degradation efficiencies for organic pollutants. Furthermore, ferrite-semiconductor composites have shown substantial improvements in charge separation, visible light utilization, and electron-hole recombination suppression, leading to greater photocatalytic efficiency. Despite these advances, several challenges remain, including charge recombination, limited stability, and scalability for real-world applications. Photo corrosion and fouling reduce long-term catalytic activity, while the transition to industrial-scale use is hindered by the variability of wastewater conditions and the high cost of large-scale production. Green synthesis methods, which emphasize eco-friendly processes and minimize hazardous chemicals, offer a promising path forward, enabling the sustainable production of ferrite-based photocatalysts without compromising performance. Hybridization with the latest advanced materials offers exciting opportunities to further enhance the photocatalytic performance of ferrites. For example, integrating MXene, with its high conductivity and excellent electron transfer capabilities, can significantly reduce recombination rates, leading to over 40% improvement in photocatalytic activity. Similarly, g-C_3N_4, with its narrow band gap (~2.7 eV), improves visible light utilization and has demonstrated enhanced degradation of persistent organic pollutants like pharmaceuticals. The development of ferrite-MXene and ferrite-g-C_3N_4 hybrids represents a critical advancement, as these materials exhibit superior charge dynamics and durability under visible light irradiation.

Moving forward, future research should focus on optimizing multi-element doping strategies to further improve visible light absorption and charge carrier mobility. In addition, refining synthesis techniques, particularly those involving green chemistry approaches, will be essential for ensuring the scalability and sustainability of these materials. Hybridization with cutting-edge materials, such as carbon-based nanomaterials, perovskites, and metal-organic frameworks (MOFs), presents a frontier for achieving higher catalytic efficiencies. These hybrid systems could significantly enhance surface area, promote superior electron transport, and increase photocatalytic durability, leading to even higher degradation rates and broader pollutant scope. Pilot-scale testing in real-world wastewater treatment facilities is crucial to evaluate the long-term stability, regeneration, and recyclability of these advanced photocatalysts. Ensuring their economic viability and maintaining high performance under diverse environmental conditions will be key to large-scale adoption. With continued advancements in material design, hybridization, and sustainable production methods, ferrite-based photocatalysts have the potential to revolutionize wastewater treatment, providing an efficient, scalable, and environmentally friendly solution to global water contamination challenges.

Acknowledgements

YK, AS, AA would like to thank Maharaja Agrasen University, Baddi India. KS would like to thank DAV College, Sector 10 Chandigarh for their research assistance.

Declaration of generative AI in scientific writing

ChatGPT was used during the preparation of this manuscript to aid in grammar correction and improve readability. The authors thoroughly reviewed and edited all content and accept full responsibility for the final version of the published article.

CRediT author statement

Yogesh Kumar: Conceptualization, Methodology, Software, Writing - Original draft preparation; **Vidushi Karol**: Data curation, Writing - Original draft preparation; **Abhishek Awasthi**: Visualization, Investigation, Writing - Original draft preparation; **Anshu Sharma**: Supervision, Writing - Original draft preparation; **Vineet Kumar**: Software, Validation, Writing - Original draft preparation; **Kulvinder Singh**: Writing - Reviewing and Editing, Supervision.

References

[1] FO Ajibade, B Adelodun, KH Lasisi, OO Fadare, TF Ajibade, NA Nwogwu, ID Sulaymon, AY Ugya, HC Wang and A Wang. *Environmental pollution and their socioeconomic impacts*. *In*: A Kumar, VK Singh, P Singh and VK Mishra (Eds.). Microbe mediated remediation of environmental contaminants. Elsevier, Amsterdam, Netherlands, 2021, p. 321-354.

[2] A Rani, AS Patel, A Chakraborti, K Singh and P Sharma. Tailoring optical and magnetic properties of molybdenum disulphide nanosheets by incorporating plasmonic gold nanoparticles. *arXiv* 2020. https://doi.org/10.48550/arxiv.1912.03869

[3] M Bryukhov and D Ulrikh. Wastewater treatment: Methods and prospects. *IOP Conference Series: Earth and Environmental Science* 2022; **1061(1)**, 012049.

[4] Y Huang, Y You, M Wu, M Han, J Zhang, W Gao, D Xie, H Chen, H Ou, N Song, C Cheng, W Zhuang, J Li, Z Lei, B Jin, Z Zhou and M Li. Chemical characterization and source attribution of organic pollutants in industrial wastewaters from a Chinese chemical industrial park. *Environmental Research* 2023; **229**, 115980.

[5] P Asaithambi, MB Yesuf, R Govindarajan, P Selvakumar, S Niju, T Pandiyarajan, A Kadier, D D Nguyen and E Alemayehu. Industrial wastewater treatment using batch recirculation electrocoagulation (BRE) process: Studies on operating parameters. *Sustainable Chemistry for the Environment* 2023; **2**, 100014.

[6] Y Wu, Z Gong, S Wang and L Song. Occurrence and prevalence of antibiotic resistance genes and pathogens in an industrial park wastewater treatment plant. *Science of The Total Environment* 2023; **880**, 163278.

[7] S Deng, J Hu, SL Ong, Q Li and J Han. Editorial: Advanced technologies for industrial wastewater reclamation. *Frontiers in Environmental Science* 2023; **11**, 1187335.

[8] L Lin, H Yang and X Xu. Effects of water pollution on human health and disease heterogeneity: A review. *Frontiers in Environmental Science* 2022; **10**, 880246.

[9] S Sarkar, G Mawari, N Kumar, MK Daga and M M Singh. Evaluation of water quality, urinary mercury & arsenic investigation and survey of diseases associated with drinking water sources. *International Journal of Medical Students* 2022; **10(1)**, S222.

[10] S Saquib, A Gupta and A Joshi. Emerging water crisis: Impact of urbanization on water resources and constructed wetlands as a nature-based solution (NbS). *Current Directions in Water Scarcity Research* 2022; **6**, 447-468.

[11] A Abou-Shady, MS Siddique and W Yu. A critical review of recent progress in global water reuse during 2019-2021 and perspectives to overcome future water crisis. *Environments* 2023; **10(9)**, 159.

[12] D Parde and M Behera. *Challenges of wastewater and wastewater management*. *In:* MP Shah (Ed.). Sustainable industrial wastewater treatment and pollution control. Springer Nature, Singapore, 2023, p. 229-255.

[13] Y Kumar, V Karol and A Sharma. Effect of compositional changes on dielectric and ferroelectric properties of Zr substituted barium titanate. *AIP Conference Proceedings* 2022; **2451(1)**, 020019.

[14] M Farzana, MM Haque, S Sonali, A Saha, M Razzak and RA Khan. Types and treatment technology of industrial wastewater. *Journal of*

Chemical, Environmental and Biological Engineering 2023; **6(2)**, 56-69.

[15] OA Valentine, AO Chukwuebuka, AE Obumneme, AA Solace, OP Ogechi, MC Okwudifele, EE Chikwere, SI Izuchukwu, NN Chukwudi and NC Oscar. Characterisation and treatment of automobile and battery water waste using coagulation and adsorption technique. *Path of Science* 2022; **8(9)**, 1030-1041.

[16] B J Singh, A Chakraborty and R Sehgal. A systematic review of industrial wastewater management: Evaluating challenges and enablers. *Journal of Environmental Management* 2023; **348**, 119230.

[17] Y Liu, H Liu and Z Shen. Nanocellulose based filtration membrane in industrial waste water treatment: A review. *Materials* 2021; **14(18)**, 5398.

[18] B Köker and MS Cebeci. Removal of Cr(VI) from tanning wastewater using chitosan-SDS complexes in PEUF: Optimization and analysis via response surface methodology. *Journal of Water Process Engineering* 2023; **54**, 103966.

[19] N Nadeem, M Zahid, HN Bhatti, I Shahid, G Mustafa and A Tabasum. *Wastewater remediation using coal fly ash nanocomposites*. *In*: KA Abd-Elsalam and M Zahid (Eds.). Aquananotechnology. Elsevier, Amsterdam, Netherlands, 2021, p. 159-184.

[20] L Yu, M Han and F He. A review of treating oily wastewater. *Arabian Journal of Chemistry* 2017; **10**, S1913-S1922.

[21] TY Haan, PMI Nordin, NA Juanda, MA Mohd Shafi and P Krishnan. A review on adsorption process for the treatment of oily wastewater. *Advances in Environmental and Engineering Research* 2023; **04(01)**, 1-30.

[22] F Younas, A Mustafa, ZUR Farooqi, X Wang, S Younas, W Mohy-Ud-Din, MA Hameed, MM Abrar, AA Maitlo, S Noreen and MM Hussain. Current and emerging adsorbent technologies for wastewater treatment: Trends, limitations, and environmental implications. *Water* 2021; **13(2)**, 215.

[23] Y Vieira, JMND Santos, JS Piccin, Á Bonilla-Petriciolet and GL Dotto. *Adsorption as an efficient alternative for the removal of toxic metals from water and wastewater*. *In*: JS Piccin, A Dettmer and N Chandrasekaran. Toxic metals contamination. 1st ed. CRC Press, Boca Raton, United States, 2022, p. 146-171.

[24] T Nikbeen and AK Nayab. Transformation of traditional wastewater treatment methods into advanced oxidation processes and the role of ozonation. *Journal of Ecological Engineering* 2023; **24(6)**, 173-189.

[25] N Chaukura, TC Madzokere and TE Tshabalala. *Selected advanced oxidation processes for wastewater remediation*. *In*: E Fosso-Kankeu, S Pandey and SS Ray (Eds.). Photoreactors in advanced oxidation processes. Wiley, New Jersey, United States, 2023, p. 151-174.

[26] HA El-Gawad, EE Ebrahiem, MY Ghaly, AA Afify and RM Mohamed. An application of advanced oxidation process on industrial crude oily wastewater treatment. *Scientific Reports* 2023; **13(1)**, 3420.

[27] S Agrawal, AK Chohadia, P Sherry, G Malhotra and K Verma. A review on wastewater treatment containing organic pollutants using advance oxidation processes. *International Journal of Scientific Research in Science and Technology* 2023; **10(1)**, 50-75.

[28] Y Nosaka and A Nosaka. *Introduction to photocatalysis: From basic science to applications*. The Royal Society of Chemistry, Cambridge, United Kingdom, 2016.

[29] DT Ruziwa, AE Oluwalana, M Mupa, L Meili, R Selvasembian, MM Nindi, M Sillanpaa, W Gwenzi and N Chaukura. Pharmaceuticals in wastewater and their photocatalytic degradation using nano-enabled photocatalysts. *Journal of Water Process Engineering* 2023; **54**, 103880.

[30] RP Brice, H Mouldi, KL Suveechard, G Vincent, CB Carole, JC Claire and P Gaël. Implementation of an advanced photooxidation process to intensify pharmaceuticals removal by a membrane bioreactor. *Chemical Engineering and Processing - Process Intensification* 2023; **191**, 109460.

[31] MH Dalhat and A Ahmad. *Removal of pesticides from water and wastewater by solar-driven photocatalysis*. *In*: M Shah, S Rodriguez-Couto and J Biswas (Eds.). Development in wastewater

treatment research and processes. Elsevier, Amsterdam, Netherlands, 2022, p. 435-458.

[32] M Arfanis, G Theodorakopoulos, C Anagnostopoulos, I Georgaki, K Liappis, G Romanos, E Markellou and P Falaras. Photocatalytic removal of pesticides present in agro-industrial water effluents. *In*: Proceedings of the 17th International Conference on Environmental Science and Technology, Athens, Greece. 2021.

[33] D M EL-Mekkawi. *Polymer-based photocatalysis for remediation of wastewater contaminated with organic dyes*. *In*: A Khadir and SS Muthu (Eds.). Polymer technology in dye-containing wastewater. Springer Nature, Singapore, 2022, p. 57-100.

[34] O Koba-Ucuna, I Arslan-Alaton, IN Sora and M Bekbölet. Persulfate-enhanced lanthanum iron oxide-mediated photocatalysis can effectively degrade an aqueous industrial dye and mineralize water and wastewater. *Desalination and Water Treatment* 2022; **267**, 215-230.

[35] H Xia, MA Ahmad, J Guo and Y Yang. Unraveling the roles of MW/UV/TiO_2 photocatalysis technologies for organic wastewater treatment. *Catalysts* 2023; **13(4)**, 754.

[36] M E Borges, H De Paz Carmona, M Gutiérrez and P Esparza. Photocatalytic removal of water emerging pollutants in an optimized packed bed photoreactor using solar light. *Catalysts* 2023; **13(6)**, 1023.

[37] L Vazquez, LMMT Gomes, PH Presumido, DGD Rocca, RFPM Moreira, T Dagnac, M Llompart, A I Gomes and VJP Vilar. Tubular membrane photoreactor for the tertiary treatment of urban wastewater towards antibiotics removal: application of different photocatalyst/oxidant combinations and ozonation. *Journal of Environmental Chemical Engineering* 2023; **11(3)**, 109766.

[38] N Shah, X Wang and J Tian. Recent advances in MXenes: A promising 2D material for photocatalysis. *Materials Chemistry Frontiers* 2023; **7(19)**, 4184-4201.

[39] FT Geldasa, MA Kebede, MW Shura and FG Hone. Experimental and computational study of metal oxide nanoparticles for the photocatalytic degradation of organic pollutants: A review. *RSC Advances* 2023; **13(27)**, 18404-18442.

[40] H Wilson, A Van Rooij, K Jenewein, J Knöppel, A Kormányos, S Cherevko, S Sunde and A Erbe. Photocorrosion of n- and p-type semiconducting oxide-covered metals: Case studies of anodized titanium and copper. *Physica Status Solidi (a)* 2022; **219(11)**, 2100852.

[41] K Qi and J Yu. Modification of ZnO-based photocatalysts for enhanced photocatalytic activity. *Interface Science and Technology* 2020; **31**, 265-284.

[42] L Nie and Q Zhang. Recent progress in crystalline metal chalcogenides as efficient photocatalysts for organic pollutant degradation. *Inorganic Chemistry Frontiers* 2017; **4(12)**, 1953-1962.

[43] V Navakoteswara Rao, P Ravi, M Sathish, M Vijayakumar, M Sakar, M Karthik, S Balakumar, KR Reddy, NP Shetti, TM Aminabhavi and MV Shankar. Metal chalcogenide-based core/shell photocatalysts for solar hydrogen production: Recent advances, properties and technology challenges. *Journal of Hazardous Materials* 2021; **415**, 125588.

[44] S Tiwari, S Kumar and AK Ganguli. Role of MoS2/rGO co-catalyst to enhance the activity and stability of Cu2O as photocatalyst towards photoelectrochemical water splitting. *Journal of Photochemistry and Photobiology A: Chemistry* 2022; **424**, 113622.

[45] Z Li, X Meng and Z Zhang. Recent development on MoS2-based photocatalysis: A review. *Journal of Photochemistry and Photobiology C: Photochemistry Reviews* 2018; **35**, 39-55.

[46] G Singh, MK Ubhi, K Jeet, C Singla and M Kaur. A review on impacting parameters for photocatalytic degradation of organic effluents by ferrites and their nanocomposites. *Processes* 2023; **11(6)**, 1727.

[47] MD Nguyen, HV Tran, S Xu and TR Lee. Fe_3O_4 Nanoparticles: Structures, synthesis, magnetic properties, surface functionalization, and emerging applications. *Applied Sciences* 2021; **11(23)**, 11301.

[48] V Karol, P Sharma, A Singh, D Goel and S Kaur. *Review of energy storage devices: Fuel cells, hydrogen storage fuel cells, rechargeable*

batteries, pv solar cells. *In*: SS Kumar, P Sharma, T Kumar and V Kumar (Eds.). ACS symposium series. American Chemical Society, Washington, D. C., 2024, p. 1-15.

[49] M Sajid. Nanomaterials: Types, properties, recent advances, and toxicity concerns. *Current Opinion in Environmental Science & Health* 2022; **25**, 100319.

[50] P Sharma, V Karol, S Kaur and M Taunk. *Fabrication and interfacial bonding of cnt-reinforced metal matrix composites*. *In*: V Khanna, P Sharma, and S Kumar (Eds.). Metal matrix composites: A modern approach to manufacturing. Bentham Science Publishers, Sharjah, United Arab Emirates, 2024, p. 116-146.

[51] N Chavan, D Dharmaraj, S Sarap and C Surve. Magnetic nanoparticles: A new era in nanotechnology. *Journal of Drug Delivery Science and Technology* 2022; **77**, 103899.

[52] EM Materón, CM Miyazaki, O Carr, N Joshi, PH S Picciani, CJ Dalmaschio, F Davis and FM Shimizu. Magnetic nanoparticles in biomedical applications: A review. *Applied Surface Science Advances* 2021; **6**, 100163.

[53] M Muhajir, P Puspitasari and JA Razak. Synthesis and applications of hematite α-Fe_2O_3: A review. *Journal of Mechanical Engineering Science and Technology* 2019; **3(2)**, 51-58.

[54] P Kumar, N Thakur, K Kumar, S Kumar, A Dutt, VK Thakur, C Gutiérrez-Rodelo, P Thakur, A Navarrete and N Thakur. Catalyzing innovation: Exploring iron oxide nanoparticles - Origins, advancements, and future application horizons. *Coordination Chemistry Reviews* 2024; **507**, 215750.

[55] N Ajinkya, X Yu, P Kaithal, H Luo, P Somani and S Ramakrishna. Magnetic Iron Oxide Nanoparticle (IONP) synthesis to applications: present and future. *Materials* 2020; **13(20)**, 4644.

[56] W Yang, X Yang, L Zhu, H Chu, X Li and W Xu. Nanozymes: Activity origin, catalytic mechanism, and biological application. *Coordination Chemistry Reviews* 2021; **448**, 214170.

[57] S Rajendran, SG Wanale, A Gacem, VK Yadav, I A Ahmed, JS Algethami, SD Kakodiya, T Modi, AM Alsuhaibani, KK Yadav and S Cavalu. Nanostructured iron oxides: Structural, optical, magnetic, and adsorption characteristics for cleaning industrial effluents. *Crystals* 2023; **13(3)**, 472.

[58] B Alqassem, F Banat, G Palmisano and M Abu Haija. Emerging trends of ferrite-based nanomaterials as photocatalysts for environmental remediation: A review and synthetic perspective. *Sustainable Materials and Technologies* 2024; **40**, e00961.

[59] J Nath, VP Singh, R Sehgal, S Kumar, V Kumar, and R Sehgal. *Utilization of magnetic nanoferrite-based photocatalysts for elimination of organic pollutants from wastewater*. *In*: S Kalia, R Jasrotia and VP Singh (Eds.). Magnetic nanoferrites and their composites. Elsevier, Amsterdam, Netherlands, 2023, p. 317-350.

[60] P Mandyal, R Sharma, S Sambyal, B Fang, M Sillanpää, V Kumar, S Kalia and P Shandilya. *A new generation of magnetic nanoferrite-based nanocomposites for environmental applications*. *In*: S Kalia, R Jasrotia and VP Singh (Eds.). Magnetic nanoferrites and their composites. Elsevier, Amsterdam, Netherlands, 2023, p. 257-293.

[61] B Sehgal and GB Kunde. *Recent Advances in the catalytic applications of magnetic nanomaterials*. *In*: RK Gupta, SR Mishra and TA Nguyen (Eds.). Emerging applications of low dimensional magnets. 1st ed. CRC Press, Boca Raton, 2022, p. 9-31.

[62] KK Kefeni and BB Mamba. Photocatalytic application of spinel ferrite nanoparticles and nanocomposites in wastewater treatment: Review. *Sustainable Materials and Technologies* 2020; **23**, e00140.

[63] A Šutka, R Pärna, T Käämbre and V Kisand. Synthesis of p-type and n-type nickel ferrites and associated electrical properties. *Physica B: Condensed Matter* 2015; **456**, 232-236.

[64] A Hosseinpour, H Sadeghi and A Morisako. Simulation of DC-hopping conduction in spinel ferrites using free electron gas model. *Journal of Magnetism and Magnetic Materials* 2007; **316(2)**, e283-e286.

[65] S Kaur, V Karol, P Kumar, G Kaur, P Sharma, A Saroa and A Singh. Energy build-up factors estimation for $BaZr_{0.10}Ti_{0.90}O_3$, $Ba_{0.90}La_{0.10}TiO_3$

and $Ba_{0.90}La_{0.10}Zr_{0.10}Ti_{0.90}O_3$ ceramics in shielding applications. *Nuclear Engineering and Technology* 2024; **56(5)**, 1822-1829.

[66] J Liu, R Li and B Yang. Carbon dots: A new type of carbon-based nanomaterial with wide applications. *ACS Central Science* 2020; **6(12)**, 2179-2195.

[67] S Munirasu, MA Haija and F Banat. Use of membrane technology for oil field and refinery produced water treatment - A review. *Process Safety and Environmental Protection* 2016; **100**, 183-202.

[68] I Othman, J Hisham Zain, M Abu Haija and F Banat. Catalytic activation of peroxymonosulfate using CeVO4 for phenol degradation: An insight into the reaction pathway. *Applied Catalysis B: Environmental* 2020; **266**, 118601.

[69] M Selvaraj, A Hai, F Banat and MA Haija. Application and prospects of carbon nanostructured materials in water treatment: A review. *Journal of Water Process Engineering* 2020; **33**, 100996.

[70] S Pal, F Banat, A Almansoori and MA Haija. Review of technologies for biotreatment of refinery wastewaters: Progress, challenges and future opportunities. *Environmental Technology Reviews* 2016; **5(1)**, 12-38.

[71] A Houbi, ZA Aldashevich, Y Atassi, ZB Telmanovna, M Saule and K Kubanych. Microwave absorbing properties of ferrites and their composites: A review. *Journal of Magnetism and Magnetic Materials* 2021; **529**, 167839.

[72] VA Pandit, GR Repe, JD Bhamre and ND Chaudhari. A review on green synthesis and characterization technique for ferrite nanoparticles and their applications. *Journal of Physics: Conference Series* 2020; **1644(1)**, 012009.

[73] Z Bielan, S Dudziak, A Kubiak and E Kowalska. Application of spinel and hexagonal ferrites in heterogeneous photocatalysis. *Applied Sciences* 2021; **11(21)**, 10160.

[74] A Vedrtnam, K Kalauni, S Dubey and A Kumar. Mechanical Engineering Department, Invertis University, Bareilly, UP, India-243001, and Departamento de Arquitectura, Escuela de Arquitectura -Universidad de Alcalá, Spain. A comprehensive study on structure, properties, synthesis and characterization of ferrites. *AIMS Materials Science* 2020; **7(6)**, 800-835.

[75] M Fantauzzi, F Secci, MS Angotzi, C Passiu, C Cannas, and A Rossi. Nanostructured spinel cobalt ferrites: Fe and Co chemical state, cation distribution and size effects by X-ray photoelectron spectroscopy. *RSC Advances* 2019; **9(33)**, 19171-19179.

[76] SK Dutta, M Akhter, J Ahmed, MK Amin and PK Dhar. Synthesis and catalytic activity of spinel ferrites: A brief review. *Biointerface Research in Applied Chemistry* 2021; **12(4)**, 4399-4416.

[77] SJ Salih and WM Mahmood. Review on magnetic spinel ferrite (MFe_2O_4) nanoparticles: From synthesis to application. *Heliyon* 2023; **9(6)**, e16601.

[78] R Kodasma, B Palas, G Ersöz and S Atalay. Photocatalytic activity of copper ferrite graphene oxide particles for an efficient catalytic degradation of Reactive Black 5 in water. *Ceramics International* 2020; **46(5)**, 6284-6292.

[79] S Munir, A Rasheed, S Zulfiqar, M Aadil, PO Agboola, I Shakir and MF Warsi. Synthesis, characterization and photocatalytic parameters investigation of a new $CuFe_2O_4/Bi_2O_3$ nanocomposite. *Ceramics International* 2020; **46(18)**, 29182-29190.

[80] A Habibi-Yangjeh and K Pournemati. A review on emerging homojunction photocatalysts with impressive performances for wastewater detoxification. *Critical Reviews in Environmental Science and Technology* 2024; **54(4)**, 290-320.

[81] SA Jadhav, SB Somvanshi, MV Khedkar, SR Patade and KM Jadhav. Magneto-structural and photocatalytic behavior of mixed Ni–Zn nano-spinel ferrites: visible light-enabled active photodegradation of rhodamine B. *Journal of Materials Science: Materials in Electronics* 2020; **31(14)**, 11352-11365.

[82] MM Baig, S Zulfiqar, MA Yousuf, M Touqeer, S Ullah, PO Agboola, MF Warsi and I Shakir. Structural and photocatalytic properties of new rare earth La^{3+} substituted $MnFe_2O_4$ ferrite nanoparticles. *Ceramics International* 2020; **46(14)**, 23208-23217.

[83] M Rashid, W Hassan, M Aadil, HH Somaily, NM Mahdi, R Lataef, AG Taki, K Srithilat, DF

Baamer, SM Albukhari, MA Salam and A Llyas. Solar-light-driven and magnetically recoverable doped nano-ferrite: An ideal photocatalyst for water purification applications. *Optical Materials* 2023; **135**, 113192.

[84] T Kousar, KM Katubi, S Zulfiqar, ZA Alrowaili, MZ Ansari, MS Al-Buriahi, M Aadil, W Hassan, F Mahmood and M Hussain. Synthesis of nanostructured gadolinium doped mixed ferrite: A novel catalyst for the mineralization of textile dyes. *Ceramics International* 2023; **49(12)**, 19641-19651.

[85] T Kousar, M Aadil, S Zulfiqar, MF Warsi, SR Ejaz, AY Elnaggar, AM Fallatah, SM El-Bahy and F Mahmood. Wet-chemical synthesis of nanostructured Ce-doped mixed metal ferrites for the effective removal of azo dyes from industrial discharges. *Ceramics International* 2022; **48(8)**, 11858-11868.

[86] FMA Alzahrani, A Irshad, S Zulfiqar, ZA Alrowaili, N Ain, A Anwar, M Farooq Warsi and MS Al-Buriahi. Nd-doped NiFe2O4 and its composite with CNTs to tune photocatalytic activity. *Journal of Rare Earths* 2023; **41(12)**, 1919-1928.

[87] A Azimi-Fouladi, P Falak and SA Hassanzadeh-Tabrizi. The photodegradation of antibiotics on nano cubic spinel ferrites photocatalytic systems: A review. *Journal of Alloys and Compounds* 2023; **961**, 171075.

[88] PA Vinosha, A Manikandan, AS Judith Ceicilia, A Dinesh, G Francisco Nirmala, AC Preetha, Y Slimani, MA Almessiere, A Baykal and B Xavier. Review on recent advances of zinc substituted cobalt ferrite nanoparticles: Synthesis characterization and diverse applications. *Ceramics International* 2021; **47(8)**, 10512-10535.

[89] P Chand, S Vaish and P Kumar. Structural, optical and dielectric properties of transition metal (MFe_2O_4; M = Co, Ni and Zn) nanoferrites. *Physica B: Condensed Matter* 2017; **524**, 53-63.

[90] M Houshiar, F Zebhi, ZJ Razi, A Alidoust and Z Askari. Synthesis of cobalt ferrite ($CoFe_2O_4$) nanoparticles using combustion, coprecipitation, and precipitation methods: A comparison study of size, structural, and magnetic properties. *Journal of Magnetism and Magnetic Materials* 2014; **371**, 43-48.

[91] M Zahraei, A Monshi, MDP Morales, D Shahbazi-Gahrouei, M Amirnasr and B Behdadfar. Hydrothermal synthesis of fine stabilized superparamagnetic nanoparticles of Zn^{2+} substituted manganese ferrite. *Journal of Magnetism and Magnetic Materials* 2015; **393**, 429-436.

[92] A Amirabadizadeh, Z Salighe, R Sarhaddi and Z Lotfollahi. Synthesis of ferrofluids based on cobalt ferrite nanoparticles: Influence of reaction time on structural, morphological and magnetic properties. *Journal of Magnetism and Magnetic Materials* 2017; **434**, 78-85.

[93] T Prabhakaran, RV Mangalaraja, JC Denardin, and JA Jiménez. The effect of reaction temperature on the structural and magnetic properties of nano $CoFe_2O_4$. *Ceramics International* 2017; **43(7)**, 5599-5606.

[94] K K Senapati, C Borgohain and P Phukan. Synthesis of highly stable $CoFe_2O_4$ nanoparticles and their use as magnetically separable catalyst for Knoevenagel reaction in aqueous medium. *Journal of Molecular Catalysis A: Chemical* 2011; **339(1-2)**, 24-31.

[95] D Kotsikau, M Ivanovskaya, V Pankov and Y Fedotova. Structure and magnetic properties of manganese–zinc-ferrites prepared by spray pyrolysis method. *Solid State Sciences* 2015; **39**, 69-73.

[96] P Thakur, D Chahar, S Taneja, N Bhalla and A Thakur. A review on MnZn ferrites: Synthesis, characterization and applications. *Ceramics International* 2020; **46(10)**, 15740-15763.

[97] S Ahmadian-Fard-Fini, D Ghanbari and M Salavati-Niasari. Photoluminescence carbon dot as a sensor for detecting of Pseudomonas aeruginosa bacteria: Hydrothermal synthesis of magnetic hollow $NiFe_2O_4$-carbon dots nanocomposite material. *Composites Part B: Engineering* 2019; **161**, 564-577.

[98] Z Jia, D Ren and R Zhu. Synthesis, characterization and magnetic properties of $CoFe_2O_4$ nanorods. *Materials Letters* 2012; **66(1)**, 128-131.

[99] M Jalalian, SM Mirkazemi and S Alamolhoda. The effect of poly vinyl alcohol (PVA) surfactant on phase formation and magnetic properties of hydrothermally synthesized $CoFe_2O_4$ nanoparticles. *Journal of Magnetism and Magnetic Materials* 2016; **419**, 363-367.

[100] D Zhao, X Wu, H Guan and E Han. Study on supercritical hydrothermal synthesis of $CoFe_2O_4$ nanoparticles. *The Journal of Supercritical Fluids* 2007; **42(2)**, 226-233.

[101] IAF De Medeiros, AL Lopes-Moriyama and CP De Souza. Effect of synthesis parameters on the size of cobalt ferrite crystallite. *Ceramics International* 2017; **43(5)**, 3962-3969.

[102] S Phumying, S Labuayai, E Swatsitang, V Amornkitbamrung, and S Maensiri. Nanocrystalline spinel ferrite (MFe_2O_4, M=Ni, Co, Mn, Mg, Zn) powders prepared by a simple aloe vera plant-extracted solution hydrothermal route. *Materials Research Bulletin* 2013; **48(6)**, 2060-2065.

[103] M Abbas, BP Rao, N Islam, KW Kim, SM Naga, M Takahashi and C Kim. Size-controlled high magnetization $CoFe_2O_4$ nanospheres and nanocubes using rapid one-pot sonochemical technique. *Ceramics International* 2014; **40(2)**, 3269-3276.

[104] A Gupta and R Srivastava. Mini submersible pump assisted sonochemical reactors: Large-scale synthesis of zinc oxide nanoparticles and nanoleaves for antibacterial and anti-counterfeiting applications. *Ultrasonics Sonochemistry* 2019; **52**, 414-427.

[105] S Natarajan, K Harini, GP Gajula, B Sarmento, M T Neves-Petersen and V Thiagarajan. Multifunctional magnetic iron oxide nanoparticles: diverse synthetic approaches, surface modifications, cytotoxicity towards biomedical and industrial applications. *BMC Materials* 2019; **1(1)**, 2.

[106] A Manikandan, R Sridhar, SA Antony and S Ramakrishna. A simple aloe vera plant-extracted microwave and conventional combustion synthesis: Morphological, optical, magnetic and catalytic properties of $CoFe_2O_4$ nanostructures. *Journal of Molecular Structure* 2014; **1076**, 188-200.

[107] A Baykal, N Kasapoğlu, Y Köseoğlu, A Başaran, H Kavas and M Toprak. Microwave-induced combustion synthesis and characterization of $Ni_xCo_{1-x}Fe_2O_4$ nanocrystals (x = 0.0, 0.4, 0.6, 0.8, 1.0). *Open Chemistry* 2008; **6(1)**, 125-130.

[108] C Barathiraja, A Manikandan, AM Uduman Mohideen, S Jayasree and SA Antony. Magnetically Recyclable Spinel $Mn_xNi_{1-x}Fe_2O_4$ (x = 0.0 - 0.5) Nano-photocatalysts: Structural, Morphological and Opto-magnetic Properties. *Journal of Superconductivity and Novel Magnetism* 2016; **29(2)**, 477-486.

[109] A Manikandan, M Durka and SA Antony. Role of Mn^{2+} doping on structural, morphological, and opto-magnetic properties of spinel $Mn_xCo_{1-x}Fe_2O_4$ (x = 0.0, 0.1, 0.2, 0.3, 0.4, and 0.5) Nanocatalysts. *Journal of Superconductivity and Novel Magnetism* 2015; **28(7)**, 2047-2058.

[110] M Sundararajan, LJ Kennedy, U Aruldoss, SK Pasha, JJ Vijaya and S Dunn. Microwave combustion synthesis of zinc substituted nanocrystalline spinel cobalt ferrite: Structural and magnetic studies. *Materials Science in Semiconductor Processing* 2015; **40**, 1-10.

[111] MH Yousefi, S Manouchehri, A Arab, M Mozaffari, GR Amiri and J Amighian. Preparation of cobalt–zinc ferrite ($Co_{0.8}Zn_{0.2}Fe_2O_4$) nanopowder via combustion method and investigation of its magnetic properties. *Materials Research Bulletin* 2010; **45(12)**, 1792-1795.

[112] M Sajjia, M Oubaha, M Hasanuzzaman and AG Olabi. Developments of cobalt ferrite nanoparticles prepared by the sol-gel process. *Ceramics International* 2014; **40(1)**, 1147-1154.

[113] V Karol, C Prakash and A Sharma. Impact of magnesium content on various properties of $Ba_{0.95-x}Sr_{0.05}Mg_xTiO_3$ ceramic system synthesized by solid state reaction route. *Materials Chemistry and Physics* 2021; **271**, 124905.

[114] L Wang, M Lu, Y Liu, J Li, M Liu and H Li. The structure, magnetic properties and cation distribution of $Co_{1-x}Mg_xFe_2O_4/SiO_2$ nanocomposites synthesized by sol-gel method. *Ceramics International* 2015; **41(3)**, 4176-4181.

[115] R Zhang, L Sun, Z Wang, W Hao, E Cao and Y Zhang. Dielectric and magnetic properties of $CoFe_2O_4$ prepared by sol-gel auto-combustion

method. *Materials Research Bulletin* 2018; **98**, 133-138.

[116] M Hashim, Alimuddin, S Kumar, BH Koo, SE Shirsath, EM Mohammed, J Shah, RK Kotnala, HK Choi, H Chung and R Kumar. Structural, electrical and magnetic properties of Co-Cu ferrite nanoparticles. *Journal of Alloys and Compounds* 2012; **518**, 11-18.

[117] MK Zate, SD Raut, SD Shirsat, S Sangale and A S Kadam. *Ferrite nanostructures*. *In*: RS Mane and VV Jadhav (Eds.). Spinel ferrite nanostructures for energy storage devices. Elsevier, Amsterdam, Netherlands, 2020, p. 13-34.

[118] V Karol, C Prakash and A Sharma. Observation of high dielectric properties of Mg-substituted BST ceramic synthesized by conventional solid-state route. *Journal of Materials Science: Materials in Electronics* 2021; **32(14)**, 19478-19486.

[119] AV Raut, RS Barkule, DR Shengule and KM Jadhav. Synthesis, structural investigation and magnetic properties of Zn^{2+} substituted cobalt ferrite nanoparticles prepared by the sol-gel auto-combustion technique. *Journal of Magnetism and Magnetic Materials* 2014; **358-359**, 87-92.

[120] RM Mohamed, MM Rashad, FA Haraz and W Sigmund. Structure and magnetic properties of nanocrystalline cobalt ferrite powders synthesized using organic acid precursor method. *Journal of Magnetism and Magnetic Materials* 2010; **322(14)**, 2058-2064.

[121] T Dippong, EA Levei and O Cadar. Recent advances in synthesis and applications of MFe_2O_4 (M = Co, Cu, Mn, Ni, Zn) nanoparticles. *Nanomaterials* 2021; **11(6)**, 1560.

[122] GA Weisenburger, RW Barnhart, JD Clark, DJ Dale, M Hawksworth, PD Higginson, Y Kang, D J Knoechel, BS Moon, SM Shaw, GP Taber and DL Tickner. Determination of reaction heat: A comparison of measurement and estimation techniques. *Organic Process Research & Development* 2007; **11(6)**, 1112-1125.

[123] H Bakhshi, N Vahdati, A Sedghi and Y Mozharivskyj. Comparison of the effect of nickel and cobalt cations addition on the structural and magnetic properties of manganese-zinc ferrite nanoparticles. *Journal of Magnetism and Magnetic Materials* 2019; **474**, 56-62.

[124] S Kaur, A Rani, A Sharma, N Luhakhra and V Karol. *Green nanomaterials in energy storage: advancements and challenges*. *In*: SS Kumar, P Sharma, T Kumar and V Kumar (Eds.). ACS Symposium Series. American Chemical Society, Washington, D. C., 2024, p. 281-307.

[125] SH Bhuiyan, MY Miah, SC Paul, TD Aka, O Saha, M Rahaman, JI Sharif, O Habiba and Ashaduzzaman. Green synthesis of iron oxide nanoparticle using Carica papaya leaf extract: Application for photocatalytic degradation of remazol yellow RR dye and antibacterial activity. *Heliyon* 2020; **6(8)**, e04603.

[126] A Femenia, ES Sánchez, S Simal and C Rosselló. Compositional features of polysaccharides from Aloe vera (*Aloe barbadensis* Miller) plant tissues. *Carbohydrate Polymers* 1999; **39(2)**, 109-117.

[127] S Maensiri, C Masingboon, B Boonchom, and S Seraphin. A simple route to synthesize nickel ferrite ($NiFe_2O_4$) nanoparticles using egg white. *Scripta Materialia* 2007; **56(9)**, 797-800.

[128] V Harish, MM Ansari, D Tewari, AB Yadav, N Sharma, S Bawarig, ML García-Betancourt, A Karatutlu, M Bechelany and A Barhoum. Cutting-edge advances in tailoring size, shape, and functionality of nanoparticles and nanostructures: A review. *Journal of the Taiwan Institute of Chemical Engineers* 2023; **149**, 105010.

[129] Neha, P Kumar, V Karol, P Sharma, S Chahal and C Prakash. Improved energy storage and electrocaloric properties in Sm^{3+}- and Fe^{3+}-substituted BCZT Ceramics. *Journal of Electronic Materials* 2025; **54(1)**, 59-65.

[130] A Mills and S Le Hunte. An overview of semiconductor photocatalysis. *Journal of Photochemistry and Photobiology A: Chemistry* 1997; **108(1)**, 1-35.

[131] MA Hassaan, MA El-Nemr, MR Elkatory, S Ragab, VC Niculescu and A El Nemr. Principles of photocatalysts and their different applications: A review. *Topics in Current Chemistry* 2023; **381(6)**, 31.

[132] F Glaser, C Kerzig and OS Wenger. Multi-photon excitation in photoredox catalysis: Concepts, applications, methods. *Angewandte Chemie International Edition* 2020; **59(26)**, 10266-10284.

[133] MH EL-Saeid, A BaQais and M Alshabanat. Study of the photocatalytic degradation of highly abundant pesticides in agricultural soils. *Molecules* 2022; **27(3)**, 634.

[134] WS Koe, JW Lee, WC Chong, YL Pang and LC Sim. An overview of photocatalytic degradation: photocatalysts, mechanisms, and development of photocatalytic membrane. *Environmental Science and Pollution Research* 2020; **27(3)**, 2522-2565.

[135] I Ibrahim, I Ali, T Salama, A Bahgat and M Mohamed. Synthesis of magnetically recyclable spinel ferrite (MFE_2O_4, M = ZN, CO, MN) nanocrystals engineered by sol gel-hydrothermal technology: High catalytic performances for nitroarenes reduction. *Al-Azhar Bulletin of Science* 2015; **26(1-A)**, 15-28.

[136] TD Thanh, TTN Nha, TTH Giang, PH Nam, DN Toan, DT Khan, DH Manh and PT Phong. Structural, optical, magnetic properties and energy-band structure of MFe_2O_4 (M = Co, Fe, Mn) nanoferrites prepared by co-precipitation technique. *RSC Advances* 2024; **14(33)**, 23645-23660.

[137] R Sharma, V Kumar, S Bansal and S Singhal. Assortment of magnetic nanospinels for activation of distinct inorganic oxidants in photo-Fenton's process. *Journal of Molecular Catalysis A: Chemical* 2015; **402**, 53-63.

[138] R Sharma, S Bansal and S Singhal. Tailoring the photo-Fenton activity of spinel ferrites (MFe_2O_4) by incorporating different cations (M = Cu, Zn, Ni and Co) in the structure. *RSC Advances* 2015; **5(8)**, 6006-6018.

[139] V Bilovol, M Sikora, S Lisníková, J Żukrowski, K Berent and M Gajewska. Occupancies of tetra- and octahedral sites in $CoFe_2O_4$ nanoparticles: The effect of the sintering temperature. *Journal of Applied Physics* 2023; **134(9)**, 094304.

[140] TA Tran, HC Tran, NT Nghiem, LV Truong-Son, GT Imanova and SH Jabarov. Effect of doping Mn ion on the crystal structure and cation distribution in $Co_{1-x}Mn_xFe_2O_4$ compounds. *Journal of Materials Science: Materials in Engineering* 2025; **20(1)**, 5.

[141] H Ma, X Wang, M Qiao, Z Liu, M A Hossain, Y Fu, G Wang, P Wang and G Shao. $NiFe_2O_4$/N-CNT mediated peroxydisulfate activation via radical and non-radical pathways for water purification. *Journal of Environmental Chemical Engineering* 2024; **12(5)**, 113390.

[142] A Al-Anazi, WH Abdelraheem, C Han, MN Nadagouda, L Sygellou, MK Arfanis, P Falaras, V K Sharma and DD Dionysiou. Cobalt ferrite nanoparticles with controlled composition-peroxymonosulfate mediated degradation of 2-phenylbenzimidazole-5-sulfonic acid. *Applied Catalysis B: Environmental* 2018; **221**, 266-279.

[143] H Li, N Yuan, C Wang, X Yan and J Qian. New insights into the $CuFe_2O_4$/PMS process: The roles of surface Cu(III) species and free radicals. *Chemical Engineering Journal Advances* 2023; **15**, 100506.

[144] CB Chen, F Zhang, CX Li, JY Lu, S Cui, HQ Liu, and WW Li. A magnetic $CoFe_2O_4$–CNS nanocomposite as an efficient, recyclable catalyst for peroxymonosulfate activation and pollutant degradation. *RSC Advances* 2017; **7(87)**, 55020-55025.

[145] GD Tang, QJ Han, J Xu, DH Ji, WH Qi, ZZ Li, ZF Shang and XY Zhang. Investigation of magnetic ordering and cation distribution in the spinel ferrites $Cr_xFe_{3-x}O_4$ ($0.0 \leq x \leq 1.0$). *Physica B: Condensed Matter* 2014; **438**, 91-96.

[146] R Zhang, Q Yuan, R Ma, X Liu, C Gao, M Liu, C-L Jia and H Wang. Tuning conductivity and magnetism of $CuFe_2O_4$ via cation redistribution. *RSC Advances* 2017; **7(35)**, 21926-21932.

[147] LI Granone, K Nikitin, A Emeline, R Dillert and DW Bahnemann. Effect of the degree of inversion on the photoelectrochemical activity of spinel $ZnFe_2O_4$. *Catalysts* 2019; **9(5)**, 434.

[148] B Balko and GR Hoy. Selective excitation double Mössbauer studies (SEDM) of electron hopping in magnetite ($Fe3O_4$). *Physica B+C* 1977; **86-88**, 953-954.

[149] AM Van Diepen and FK Lotgering. Electron exchange between Fe^{2+} and Fe^{3+} on octahedral sites in spinels. *Physica B+C* 1977; **86-88**, 961-962.

[150] N Kaur, R Kaur and S Singh. Size-dependent structural, optical and photocatalytic properties of zirconium ferrite prepared via a sol-gel route. *ChemistrySelect* 2023; **8(25)**, e202300829.

[151] HY Xu, B Li and P Li. Morphology dependent photocatalytic efficacy of zinc ferrite probed for methyl orange degradation. *Journal of the Serbian Chemical Society* 2018; **83(11)**, 1261-1271.

[152] S Kumari, F Wan, A Thakur, S Singh and P Thakur. Retrievable nano-sized Co–Mg–Zn ferrite as an active photocatalyst and adsorbent for removing organic and biological contaminants for water purification. *Ceramics International* 2024; **50(2)**, 3210-3221.

[153] P Chitra, ER Kumar, T Pushpagiri and A Steephen. Size and phase purity-dependent microstructural and magnetic properties of spinel ferrite nanoparticles. *Journal of Superconductivity and Novel Magnetism* 2021; **34(4)**, 1239-1244.

[154] H Feng, Y Wang, C Wang, F Diao, W Zhu, P Mu, L Yuan, G Zhou and F Rosei. Defect-induced enhanced photocatalytic activities of reduced α - Fe_2O_3 nanoblades. *Nanotechnology* 2016; **27(29)**, 295703.

[155] K Zhong, P Sun and H Xu. Advances in defect engineering of metal oxides for photocatalytic CO_2 reduction. *Small* 2025; **21(28)**, 2310677.

[156] Y He, L Zhang, HW Xiong and X Kang. Evolution of lattice defects in nickel ferrite spinel: Oxygen vacancy and cation substitution. *Journal of Alloys and Compounds* 2022; **917**, 165494.

[157] L Song, H Zhang, J Xiong, Z Chen, Y Liu, H Zhou, W Yang, D Cao, H Huang, L Chen, M Fu and D Ye. Doped Mn modulates the local charge distribution of cobalt-based spinel catalysts to promote the availability of ligand lattice oxygen for complete oxidation of methane. *Applied Catalysis B: Environmental* 2024; **343**, 123547.

[158] VT Gritsyna, IV Afanasyev-Charkin, VA Kobyakov and KE Sickafus. Structure and electronic states of defects in spinel of different compositions $MgO{\cdot}nAl_2O_3$:Me. *Journal of the American Ceramic Society* 1999; **82(12)**, 3365-3373.

[159] M Srinivas. Superior photocatalytic activity of Mn-doped $CoFe_2O_4$ under visible light irradiation: Exploration of hopping and polaron formation in the spinel structure. *Materials Science and Engineering: B* 2021; **270**, 115222.

[160] E Hema, A Manikandan, M Gayathri, M Durka, S A Antony and BR Venkatraman. The role of Mn^{2+} - doping on structural, morphological, optical, magnetic and catalytic properties of spinel $ZnFe_2O_4$ nanoparticles. *Journal of Nanoscience and Nanotechnology* 2016; **16(6)**, 5929-5943.

[161] M Litter. Heterogeneous photocatalysis Transition metal ions in photocatalytic systems. *Applied Catalysis B: Environmental* 1999; **23(2-3)**, 89-114.

[162] CA Hall, P Ferrer, DC Grinter, S Kumar, I Da Silva, J Rubio-Zuazo, P Bencok, F De Groot, G Held and R Grau-Crespo. Spinel ferrites MFe_2O_4 (M = Co, Cu, Zn) for photocatalysis: theoretical and experimental insights. *Journal of Materials Chemistry A* 2024; **12(43)**, 29645-29656.

[163] M Sukumar, JR Rajabathar, H AL-Lohedan, S Suresh, CS Dash, M Sundararajan, PS Subudhi, S Arokiyaraj, E Yanmaz, S Yuvaraj and RSR Isaac. Synthesize and characterization of copper doped nickel ferrite nanoparticles effect on magnetic properties and visible light catalysis for rhodamine dye degradation mechanism. *Journal of Alloys and Compounds* 2023; **953**, 169902.

[164] NI Abu-Elsaad, HM Elsayed and AS Nawara. Exploring the impact of (Al3+ and Cr3+) substitution in Mn0.5Cu0.5Fe2O4 spinel ferrite on structural, optical, photocatalytic activity and magnetic characteristics: A comprehensive investigation. *Journal of Alloys and Compounds* 2025; **1018**, 179034.

[165] A Abu El-Fadl, AM Hassan and MA Kassem. Tunable cationic distribution and structure-related magnetic and optical properties by Cr^{3+} substitution for Zn^{2+} in nanocrystalline Ni-Zn ferrites. *Results in Physics* 2021; **28**, 104622.

[166] SF Mansour, A Dawood and MA Abdo. Enhanced magnetic and dielectric properties of doped Co–Zn ferrite nanoparticles by virtue of Cr^{3+} role. *Journal of Materials Science: Materials in Electronics* 2019; **30(18)**, 17262-17275.

[167] S Caliskan, AM Rodriguez, S Alexander, MA Almessiere, A Baykal and Y Slimani. Electronic, magnetic and optical properties of CoNi spinel ferrites doped by rare earth atoms: A density functional theory study. *Discover Materials* 2024; **4(1)**, 20.

[168] M Ajmal, MU Islam, GA Ashraf, MA Nazir and MI Ghouri. The influence of Ga doping on

structural magnetic and dielectric properties of NiCr0.2Fe1.8O4 spinel ferrite. *Physica B: Condensed Matter* 2017; **526**, 149-154.

[169] N Masunga, VS Vallabhapurapu and BB Mamba. A closer look at the magnetic, photo-electrochemical, and optical properties of rare earth (Sm, Dy, Ho, Er, and Yb)-doped manganese ferrite for potential use as a photocatalyst. *Ceramics International* 2024; **50(17)**, 29747-29762.

[170] M Akhter, K Amin, PK Dhar, SK Dey, MS Hossain and SK Dutta. Fabrication of rare-earth cerium-doped nickel-copper ferrite as a promising photo-catalyst for congo red-containing wastewater treatment. *RSC Advances* 2024; **14(40)**, 29083-29098.

[171] KV Rajan, S Srikanth, BR Krushna, N Navya, S C Sharma, K Manjunatha, SY Wu, SL Yu, S Mishra, V Shivakumara, S Devaraja and H Nagabhushana. Transformative Eu^{3+} doped $CoFe_2O_4$ nanoparticles: A next-generation approach to high-performance energy storage, photocatalysis, and therapeutic applications. *Inorganic Chemistry Communications* 2025; **177**, 114399.

[172] S Ghosh, PS Das, M Biswas, S Samajdar and J Mukhopadhyay. Z-scheme ferrite nanoparticle/graphite carbon nitride nanosheet heterojunctions for photocatalytic hydrogen evolution. *International Journal of Hydrogen Energy* 2025; **107**, 586-596.

[173] Z Wang, X Ning, Y Feng, R Zhang, Y He, H Zhao, J Chen, P Du and X Lu. Insights into the enhanced photoelectrochemical performance through construction of the z-scheme and type II heterojunctions. *Analytical Chemistry* 2022; **94(23)**, 8539-8546.

[174] Y Zhang, M Du, Y Ma, J Shang and B Qiu. Valence engineering via double exchange interaction in spinel oxides for enhanced oxygen evolution catalysis. *Materials Today Catalysis* 2023; **3**, 100027.

[175] S Roy, C Kumar Ghosh, S Dey and AK Pal. *Solid state & microelectronics technology*. Bentham Science Publishers, Sharjah, United Arab Emirates, 2023, p. 91-121.

[176] A Lajn, HV Wenckstern, Z Zhang, C Czekalla, G Biehne, J Lenzner, H Hochmuth, M Lorenz, M Grundmann, S Wickert, C Vogt and R Denecke. Properties of reactively sputtered Ag, Au, Pd, and Pt Schottky contacts on n-type ZnO. *Journal of Vacuum Science & Technology B: Microelectronics and Nanometer Structures Processing, Measurement, and Phenomena* 2009; **27(3)**, 1769-1773.

[177] M Berdakin, G Soldano, FP Bonafé, V Liubov, B Aradi, T Frauenheim and CG Sánchez. Dynamical evolution of the Schottky barrier as a determinant contribution to electron-hole pair stabilization and photocatalysis of plasmon-induced hot carriers. *Nanoscale* 2022; **14(7)**, 2816-2825.

[178] L Harikrishnan and A Rajaram. Constructive Z-scheme interfacial charge transfer of a spinel ferrite-supported g-C3N4 heterojunction architect for photocatalytic degradation. *Journal of Alloys and Compounds* 2024; **976**, 172987.

[179] MA Bashar, MTH Molla, D Chandra, MD Malitha, MS Islam, MS Rahman and MS Ahsan. Hydrothermal synthesis of cobalt substitute zinc-ferrite ($Co_{1-x}Zn_xFe_2O_4$) nanodot, functionalised by polyaniline with enhanced photocatalytic activity under visible light irradiation. *Heliyon* 2023; **9(4)**, e15381.

[180] D Ravichandran, MA Megala, K Anbalagan, P Srivastava, MA Al-Dosary, AA Hatamleh and S Murugesan. Eco-friendly synthesis of biochar-$CoFe_2O_4$ nanocomposites using *Ulva lactuca* L. for photocatalytic degradation of Congo red and in vitro biological applications. *Colloids and Surfaces A: Physicochemical and Engineering Aspects* 2025; **713**, 136465.

[181] D Pattappan, KV Kavya, S Varghese, RTR Kumar and Y Haldorai. Plasmonic effect and charge separation-induced photocatalytic degradation of organic dyes utilizing Au/$ZnFe_2O_4$@rGO ternary composite. *Applied Physics A* 2020; **126(10)**, 785.

[182] Z Geng, S Liu, X Zhou, L Qin, F Xu, X Huo, D Ma, X Fan, W He and C Lai. Recent progress on photo-driven heterogeneous persulfate activation process induced by Fe-based materials. *Journal of Environmental Chemical Engineering* 2025; **13(3)**, 116908.

[183] A Halfadji. Facile prepared Fe_3O_4 nanoparticles as a nano-catalyst on photo-fenton process to remediation of methylene blue dye from water: Characterisation and optimization. *Global NEST Journal* 2023; **26(1)**, 1-6.

[184] JJ Samraj, R Manju, M Ashokkumar and B Neppolian. Leveraging the critical role of $CoFe_2O_4/ZnWO_4$ heterostructure for the enhanced sonophotocatalytic degradation of tetracycline, chlortetracycline, and chloramphenicol: Mechanism insights and pathways. *Journal of Cleaner Production* 2025; **492**, 144846.

[185] S Hema, OD Jayakumar and S Sambhudevan. Temperature-controlled morphology and enhanced functionalities of hydrothermally synthesized $SrFe_2O_4$ nanostructures for multifaceted applications. *Surfaces and Interfaces* 2024; **48**, 104252.

[186] S Asiri, M Sertkol, H Güngüneş, M Amir, A Manikandan, İ Ercan and A Baykal. The temperature effect on magnetic properties of $NiFe_2O_4$ nanoparticles. *Journal of Inorganic and Organometallic Polymers and Materials* 2018; **28(4)**, 1587-1597.

[187] S Zhang, J Wu, F Li and L Li. Enhanced photocatalytic performance of spinel ferrite (MFe_2O_4, M=Zn, Mn, Co, Fe, Ni) catalysts: The correlation between morphology–microstructure and photogenerated charge efficiency. *Journal of Environmental Chemical Engineering* 2022; **10(3)**, 107702.

[188] VAF Samson, B Bernadsha, M Mahendiran, K L Lawrence, J Madhavan, MVA Raj and S Prathap. Impact of calcination temperature on structural, optical, and magnetic properties of spinel CuFe2O4 for enhancing photocatalytic activity. *Journal of Materials Science: Materials in Electronics* 2020; **31(9)**, 6574-6585.

[189] A Manohar, C Krishnamoorthi, KCB Naidu and B P Narasaiah. Dielectric, Magnetic Hyperthermia and Photocatalytic Properties of $Mg_{0.7}Zn_{0.3}Fe_2O_4$ Nanocrystals. *IEEE Transactions on Magnetics* 2020; **56(12)**, 1-7.

[190] Y Cho, A Yamaguchi, A S Sinaga, Y Yang and M Miyauchi. Photocatalysis under thermally shifted bandgap. *Applied Catalysis A: General* 2022; **643**, 118772.

[191] S Singh, AK Atri, I Qadir, S Sharma, U Manhas and D Singh. Role of different fuels and sintering temperatures in the structural, optical, magnetic, and photocatalytic properties of chromium-containing nickel ferrite: Kinetic study of photocatalytic degradation of rhodamine B dye. *ACS Omega* 2023; **8(7)**, 6302-6317.

[192] G Singh, A Kaur, M Kaur, K Jeet and JN Babu. Enhancing photocatalytic potential of $Mg_{0.5}Ti_{0.5}Fe_2O_{4.5}$ NPs by optimizing the sintering temperature. *Ceramics International* 2025; **51(4)**, 5135-5147.

[193] SM Suryawanshi, DS Badwaik, PS Hedaoo, VV Warhate, VD Badwaik and PP Lekurwade. pH influenced synthesis and characterization of $Ni_{0.3}Cu_{0.3}Zn_{0.4}Fe_2O_4$ nano ferrite for energy storage and high frequency applications. *IOP Conference Series: Earth and Environmental Science* 2023; **1281(1)**, 012044.

[194] J Mazurenko, L Kaykan, AK Sijo, M Moiseienko, M Kuzyshyn, N Ostapovych and M Moklyak. The influence of reaction medium pH on the structure, optical, and mechanical properties of nanosized Cu-Fe ferrite synthesized by the sol-gel autocombustion method. *Journal of Nano Research* 2023; **81**, 65-84.

[195] N Mongia, AK Srivastava, D Bansal, PK Giri, D K Goswami, A Perumal and A Chattopadhyay. Effect of pH on magnetic and structural properties of low temperature synthesized $MgFe_2O_4$ Nanoparticles. *In*: Proceedings of the International conference on advanced nanomaterials and nanotechnology (ICANN-2009), Assam, India. 2010, p. 394-400.

[196] A Hameed, MA Gondal, ZH Yamani and AH Yahya. Significance of pH measurements in photocatalytic splitting of water using 355 nm UV laser. *Journal of Molecular Catalysis A: Chemical* 2005; **227(1-2)**, 241-246.

[197] SEM Ghahfarokhi and EM Shobegar. Influence of pH on the structural, magnetic and optical properties of SrFe2O4 nanoparticles. *Journal of Materials Research and Technology* 2020; **9(6)**, 12177-12186.

[198] NF Jaafar, AA Jalil, S Triwahyono, A Ripin and MW Ali. Significant effect of pH on photocatalytic degradation of organic pollutants

using semiconductor catalysts. *Jurnal Teknologi* 2016. https://doi.org/10.11113/jt.v78.9559

[199] P Dhiman, G Rana, A Kumar, G Sharma, DVN Vo, TS AlGarni, M Naushad and ZA ALOthman. Nanostructured magnetic inverse spinel Ni-Zn ferrite as environmental friendly visible light driven photo-degradation of levofloxacin. *Chemical Engineering Research and Design* 2021; **175**, 85-101.

[200] M Baalousha, A Manciulea, S Cumberland, K Kendall and JR Lead. Aggregation and surface properties of iron oxide nanoparticles: Influence of ph and natural organic matter. *Environmental Toxicology and Chemistry* 2008; **27(9)**, 1875-1882.

[201] W Ramadan, Y AlSalka, O Al-Madanat and DW Bahnemann. *Synthesis of magnetic ferrite and TiO_2-based nanomaterials for photocatalytic water splitting applications*. *In*: I Uddin and I Ahmad (Eds.). Synthesis and applications of nanomaterials and nanocomposites. Springer Nature, Singapore, 2023, p. 293-329.

[202] S Peiris, HB De Silva, KN Ranasinghe, SV Bandara and IR Perera. Recent development and future prospects of TiO_2 photocatalysis. *Journal of the Chinese Chemical Society* 2021; **68(5)**, 738-769.

[203] Y Ren, Y Dong, Y Feng and J Xu. Compositing two-dimensional materials with TiO_2 for photocatalysis. *Catalysts* 2018; **8(12)**, 590.

[204] AD Patil, RA Pawar, SM Patange, SS Jadhav, SK Gore, SE Shirsath and SS Meena. TiO_2-doped $Ni_{0.4}$ $Cu_{0.3}$ $Zn_{0.3}$ Fe_2 O_4 nanoparticles for enhanced structural and magnetic properties. *ACS Omega* 2021; **6(28)**, 17931-17940.

[205] ET Helmy, A Soliman, AM Elbasiony and BS Nguyen. CuCe-ferrite/TiO_2 Nanocomposite as an efficient magnetically separable photocatalyst for dye pollutants decolorization. *Topics in Catalysis* 2023; **66(1-4)**, 53-63.

[206] J Li, Y Huang, M Su, Y Xie and D Chen. Dual light-driven p-ZnFe2O_4/n-TiO_2 catalyst: Benzene-breaking reaction for malachite green. *Environmental Research* 2022; **207**, 112081.

[207] H Boulahbel, M Benamira, F Bouremmad, N Ahmia, S Kiamouche, H Lahmar, A Souici and M Trari. Enhanced photodegradation of Congo red dye under sunlight irradiation by p-n $NiFe_2O_4$/TiO_2 heterostructure. *Inorganic Chemistry Communications* 2023; **154**, 110921.

[208] RG Ciocarlan, EM Seftel, M Mertens, A Pui, M Mazaj, N Tusar and P Cool. Novel magnetic nanocomposites containing quaternary ferrites systems $Co_{0.5}Zn_{0.25}M_{0.25}Fe_2O_4$ (M = Ni, Cu, Mn, Mg) and TiO_2-anatase phase as photocatalysts for wastewater remediation under solar light irradiation. *Materials Science and Engineering: B* 2018; **230**, 1-7.

[209] Š Slapničar, G Žerjav, J Zavašnik, M Finšgar and A Pintar. Synthesis and characterization of plasmonic Au/TiO_2 nanorod solids for heterogeneous photocatalysis. *Journal of Environmental Chemical Engineering* 2023; **11(3)**, 109835.

[210] C Ban, B Li, J Ma, Y Feng, C Lin, Y Chen, Y Wang, Y Duan, K Zhou, L Gan, S Wang and X Zhou. Plasmonic Au-TiO_2 interactions for augmented photocatalytic hydrogen evolution. *Ceramics International* 2024; **50(9)**, 15444-15451.

[211] M Amoli-Diva, A Anvari and R Sadighi-Bonabi. Synthesis of magneto-plasmonic Au-Ag NPs-decorated TiO_2-modified Fe_3O_4 nanocomposite with enhanced laser/solar-driven photocatalytic activity for degradation of dye pollutant in textile wastewater. *Ceramics International* 2019; **45(14)**, 17837-17846.

[212] SM Suryawanshi, DS Badwaik, PS Hedaoo, VV Warhate, VD Badwaik, PP Lekurwade. Sustainable photoelectrocatalytic oxidation of antibiotics using Ag–$CoFe_2O_4$@TiO_2 heteronanostructures for eco-friendly wastewater remediation. *Chemosphere* 2024; **362**, 142736.

[213] CJ Li, JN Wang, B Wang, J R Gong and Z Lin. A novel magnetically separable TiO_2/$CoFe_2O_4$ nanofiber with high photocatalytic activity under UV-vis light. *Materials Research Bulletin* 2012; **47(2)**, 333-337.

[214] I Ibrahim, GV Belessiotis, AM Elseman, MM Mohamed, Y Ren, TM Salama and MBI Mohamed. Magnetic TiO_2/$CoFe_2O_4$ Photocatalysts for Degradation of Organic Dyes and Pharmaceuticals without Oxidants. *Nanomaterials* 2022; **12(19)**, 3290.

[215] HCT Firmino, EP Nascimento, RN Araujo, FJA Loureiro, GA Neves, MA Morales and RR Menezes. Nickel ferrite/TiO_2 nanofibrous composite: enhanced photocatalytic dye degradation under visible light. *Materials Research* 2024; **27**, e20230391.

[216] S Alomairy, L Gnanasekaran, S Rajendran and W F Alsanie. Nanosized core-shell ($NiFe_2O_4$/TiO_2) heterostructure for enhanced photodegradation against polycyclic aromatic hydrocarbons. *Chemosphere* 2023; **343**, 140274.

[217] GC De Cristo Borges, IR Verdi, MZ Fidelis, HE Z Junior, GG Lenzi, ÉCF De Souza, OC Alves, and R Brackmann. Magnetic heterostructures of $NiFe_2O_4$ and TiO_2: Pechini synthesis, characterization and photocatalytic performance in arsenite oxidation. *Journal of Water Process Engineering* 2023; **56**, 104352.

[218] TB Nguyen and R Doong. Heterostructured $ZnFe_2O_4$ /TiO_2 nanocomposites with a highly recyclable visible-light-response for bisphenol A degradation. *RSC Advances* 2017; **7(79)**, 50006-50016.

[219] R Chen, S Ding, B Wang and X Ren. Preparation of $ZnFe_2O_4$@TiO_2 novel core-shell photocatalyst by ultrasonic method and its photocatalytic degradation activity. *Coatings* 2022; **12(10)**, 1407.

[220] N Arifin, KR Karim, H Abdullah and MR Khan. Synthesis of titania doped copper ferrite photocatalyst and its photoactivity towards methylene blue degradation under visible light irradiation. *Bulletin of Chemical Reaction Engineering & Catalysis* 2019; **14(1)**, 219-227.

[221] CV Tran, DD La, PNT Hoai, HD Ninh, PN Thi Hong, THT Vu, AK Nadda, XC Nguyen, DD Nguyen and HH Ngo. New TiO_2-doped Cu-Mg spinel-ferrite-based photocatalyst for degrading highly toxic rhodamine B dye in wastewater. *Journal of Hazardous Materials* 2021; **420**, 126636.

[222] AM Neris, WH Schreiner, C Salvador, UC Silva, C Chesman, E Longo and IMG Santos. Photocatalytic evaluation of the magnetic core@shell system (Co,Mn)Fe_2O_4 @TiO_2 obtained by the modified Pechini method. *Materials Science and Engineering: B* 2018; **229**, 218-226.

[223] S Yousefi-Mohammadi, M Movahedi and H Salavati. MnCo-Ferrite/TiO_2 composite as an efficient magnetically separable photocatalyst for decolorization of dye pollutants in aqueous solution. *Surfaces and Interfaces* 2018; **11**, 91-97.

[224] HS Jarusheh, A Yusuf, F Banat, MA Haija and G Palmisano. Integrated photocatalytic technologies in water treatment using ferrites nanoparticles. *Journal of Environmental Chemical Engineering* 2022; **10(5)**, 108204.

[225] Suman, S Chahal, A Kumar, P Chand and P Kumar. *Photocatalytic activity of ferrites*. *In:* JP Singh, KH Chae, RC Srivastava and OF Caltun (Eds.). Ferrite nanostructured magnetic materials. Elsevier, Amsterdam, Netherlands, 2023, p. 575-597.

[226] K Nadeem, F Zeb, M Azeem Abid, M Mumtaz, and MA Rehman. Effect of amorphous silica matrix on structural, magnetic, and dielectric properties of cobalt ferrite/silica nanocomposites. *Journal of Non-Crystalline Solids* 2014; **400**, 45-50.

[227] T Dippong, EA Levei, IG Deac, MD Lazar and O Cadar. Influence of SiO_2 embedding on the structure, morphology, thermal, and magnetic properties of $Co_{0.4}Zn_{0.4}Ni_{0.2}Fe_2O_4$ particles. *Nanomaterials* 2023; **13(3)**, 527.

[228] B Cui, H Peng, H Xia, X Guo and H Guo. Magnetically recoverable core-shell nanocomposites γ-Fe_2O_3@SiO_2@TiO_2-Ag with enhanced photocatalytic activity and antibacterial activity. *Separation and Purification Technology* 2013; **103**, 251-257.

[229] PL Hariani, M Said, A Rachmat, S Salni, N Aprianti and AF Amatullah. Synthesis of $NiFe_2O_4$/SiO_2/NiO magnetic and application for the photocatalytic degradation of methyl orange dye under UV irradiation. *Bulletin of Chemical Reaction Engineering & Catalysis* 2022; **17(4)**, 699-711.

[230] AP Kumar, D Bilehal, T Desalegn, S Kumar, F Ahmed, HCA Murthy, D Kumar, G Gupta, DK Chellappan, SK Singh, K Dua and YI Lee. Studies on synthesis and characterization of Fe_3O_4 @SiO_2 @Ru hybrid magnetic composites for reusable photocatalytic application. *Adsorption Science & Technology* 2022; **2022**, 3970287.

[231] A Liang, Q Liu, G Wen and Z Jiang. The surface-plasmon-resonance effect of nanogold/silver and its analytical applications. *TrAC Trends in Analytical Chemistry* 2012; **37**, 32-47.

[232] PL Hariani, S Salni, M Said and R Farahdiba. Core-shell $Fe_3O_4/SiO_2/TiO_2$ magnetic modified ag for the photocatalytic degradation of congo red dye and antibacterial activity. *Bulletin of Chemical Reaction Engineering & Catalysis* 2023; **18(2)**, 315-330.

[233] AAP Khan, Sonu, A Sudhaik, P Raizada, A Khan, MA Rub, N Azum, MM Alotaibi, P Singh and A M Asiri. AgI coupled $SiO_2@CuFe_2O_4$ novel photocatalytic nano-material for photo-degradation of organic dyes. *Catalysis Communications* 2023; **179**, 106685.

[234] C Singh, A Goyal, S Bansal and S Singhal. SiO_2 $@MFe_2O_4$ core-shell nanostructures: Efficient photocatalysts with excellent dispersion properties. *Materials Research Bulletin* 2017; **85**, 109-120.

[235] M Yakob, H Umar, P Wahyuningsih and RA Putra. Characterization of microstructural and optical $CoFe_2O_4/SiO_2$ ferrite nanocomposite for photodegradation of methylene blue. *AIMS Materials Science* 2019; **6(1)**, 45-51.

[236] T Dippong, D Toloman, EA Levei, O Cadar and A Mesaros. A possible formation mechanism and photocatalytic properties of $CoFe_2O_4$/PVA-SiO_2 nanocomposites. *Thermochimica Acta* 2018; **666**, 103-115.

[237] S Zinatloo-Ajabshir and M Salavati-Niasari. Preparation of magnetically retrievable $CoFe_2O_4@SiO_2@Dy_2Ce_2O_7$ nanocomposites as novel photocatalyst for highly efficient degradation of organic contaminants. *Composites Part B: Engineering* 2019; **174**, 106930.

[238] PL Hariani. Synthesis of Fe_3O_4/SiO_2/NiO magnetic composite: Evaluation of its catalytic activity for methylene blue degradation. *Global NEST Journal* 2022; **25(2)**, 36-43.

[239] N Abbas, GN Shao, SM Imran, MS Haider and HT Kim. Inexpensive synthesis of a high-performance Fe_3O_4-SiO_2-TiO_2 photocatalyst: Magnetic recovery and reuse. *Frontiers of Chemical Science and Engineering* 2016; **10(3)**, 405-416.

[240] E Alzahrani. Photodegradation of Binary Azo Dyes Using Core-Shell Fe3O4/SiO2/TiO2 Nanospheres. *American Journal of Analytical Chemistry* 2017; **08(01)**, 95-115.

[241] Y Chi, Q Yuan, Y Li, L Zhao, N Li, X Li, and W Yan. Magnetically separable $Fe_3O_4@SiO_2@TiO_2$-Ag microspheres with well-designed nanostructure and enhanced photocatalytic activity. *Journal of Hazardous Materials* 2013; **262**, 404-411.

[242] C-C Chen, D Jaihindh, S-H Hu, and Y-P Fu. Magnetic recyclable photocatalysts of Ni-Cu-Zn ferrite@$SiO_2@TiO_2$@Ag and their photocatalytic activities. *Journal of Photochemistry and Photobiology A: Chemistry* 2017; **334**, 74-85.

[243] X Meng, Y Zhuang, H Tang and C Lu. Hierarchical structured $ZnFe_2O_4$ @SiO_2 @TiO_2 composite for enhanced visible-light photocatalytic activity. *Journal of Alloys and Compounds* 2018; **761**, 15-23.

[244] E Mrotek, S Dudziak, I Malinowska, D Pelczarski, Z Ryżyńska and A Zielińska-Jurek. Improved degradation of etodolac in the presence of core-shell $ZnFe_2O_4/SiO_2/TiO_2$ magnetic photocatalyst. *Science of The Total Environment* 2020; **724**, 138167.

[245] R Rahimi, M Rabbani, HB Khosravi and A Maleki. Synthesize and characterization of mesoporous $ZrFe_2O_4SiO_2$ Core-shell Nanocomposite Modified with APTES and TCPP. *Journal of Nanostructures* 2020; **10(2)**, 404-414.

[246] LA Sánchez, BE Huayta, PG Ramos and JM Rodriguez. Enhanced photocatalytic activity of ZnO nanorods/(graphene oxide, reduced graphene oxide) for degradation of methyl orange dye. *Journal of Physics: Conference Series* 2022; **2172(1)**, 012013.

[247] AAA Mutalib and NF Jaafar. ZnO photocatalysts applications in abating the organic pollutant contamination: A mini review. *Total Environment Research Themes* 2022; **3-4**, 100013.

[248] X Shu. Research on photoelectric properties of ZnO-based semiconductor material. *Journal of Physics: Conference Series* 2023; **2541(1)**, 012060.

[249] X Gu, T Edvinsson and J Zhu. *ZnO nanomaterials: Strategies for improvement of*

photocatalytic and photoelectrochemical activities. *In*: X Wang, M Anpo and X Fu (Eds.). Current developments in photocatalysis and photocatalytic materials. Elsevier, Amsterdam, Netherlands, 2020, p. 231-244.

[250] V Gurylev. *Case study II: Defect engineering of ZnO*. *In*: V Gurylev (Ed.). Nanostructured photocatalyst via defect engineering. Springer International Publishing, Cham, Switzerland, 2021, p. 189-222.

[251] AA McLain. Photocatalytic properties of zinc oxide and graphene nanocomposites. *In*: Proceedings of the Wisconsin Space Conference, Wisconsin, United States. 2019.

[252] A Hezam, QA Drmosh, D Ponnamma, MA Bajiri, M Qamar, K Namratha, M Zare, MB Nayan, SA Onaizi and K Byrappa. Strategies to enhance ZnO photocatalyst's performance for water treatment: A comprehensive review. *The Chemical Record* 2022; **22(7)**, e202100299.

[253] RB Rajput, R Shaikh, J Sawant and RB Kale. Recent developments in ZnO-based heterostructures as photoelectrocatalysts for wastewater treatment: A review. *Environmental Advances* 2022; **9**, 100264.

[254] M saidi, M Ghazi and M Izadifard. A study on structural optical and magnetic properties of ZnO/$ZnFe_2O_4$ Composite. *Progress in Physics of Applied Materials* 2023; **3(1)**, 49-55

[255] Sonia, H Kumari, S Chahal, Suman, S Kumar, Mahak, P Kumar and A Kumar. Hydrothermally synthesized $ZnFe_2O_4$/ZnO heterojunction nanocomposites for enhanced RB dye degradation via Z-scheme photocatalysis. *Materials Chemistry and Physics* 2024; **322**, 129560.

[256] TL Phan, YD Zhang, DS Yang, NX Nghia, TD Thanh and SC Yu. Defect-induced ferromagnetism in ZnO nanoparticles prepared by mechanical milling. *Applied Physics Letters* 2013; **102(7)**, 072408.

[257] JMD Coey, K Wongsaprom, J Alaria and M Venkatesan. Charge-transfer ferromagnetism in oxide nanoparticles. *Journal of Physics D: Applied Physics* 2008; **41(13)**, 134012.

[258] DE Motaung, GH Mhlongo, SS Nkosi, GF Malgas, BW Mwakikunga, E Coetsee, HC Swart, HMI Abdallah, T Moyo and SS Ray. Shape-selective dependence of room temperature ferromagnetism induced by hierarchical ZnO nanostructures. *ACS Applied Materials & Interfaces* 2014; **6(12)**, 8981-8995.

[259] SW Kim, S Lee, ANS Saqib, YH Lee and MH Jung. Ferromagnetism in undoped ZnO nanostructures synthesized by solution plasma process. *Current Applied Physics* 2017; **17(2)**, 181-185.

[260] X Xu, C Xu, J Dai, J Hu, F Li and S Zhang. Size Dependence of defect-induced room temperature ferromagnetism in undoped ZnO nanoparticles. *The Journal of Physical Chemistry C* 2012; **116(15)**, 8813-8818.

[261] S Mal, J Narayan, S Nori, JT Prater and D Kumar. Defect-mediated room temperature ferromagnetism in zinc oxide. *Solid State Communications* 2010; **150(35-36)**, 1660-1664.

[262] AS Hamed, IA Ali, ME Ghazaly, M Al-Abyad and HE Hassan. Nanocomposites of ZnO mixed with different Ni-ferrite contents: Structural and magnetic properties. *Physica B: Condensed Matter* 2021; **607**, 412861.

[263] R Elshypany, H Selim, K Zakaria, AH Moustafa, SA Sadeek, SI Sharaa, P Raynaud and AA Nada. Elaboration of Fe_3O_4/ZnO nanocomposite with highly performance photocatalytic activity for degradation methylene blue under visible light irradiation. *Environmental Technology & Innovation* 2021; **23**, 101710.

[264] A Varadi, C Leostean, M Stefan, A Popa, D Toloman, S Pruneanu, S Tripon and S Macavei. Fe_3O_4-ZnO:V nanocomposites with modulable properties as magnetic recoverable photocatalysts. *Inorganics* 2024; **12(4)**, 119.

[265] B Janani, SS Al-amri, MK Okla, A Mohebaldin, W Soufan, B Almunqedhi, MA Abdel-Maksoud, H Abd Elgawad, AM Thomas, LL Raju and SS Khan. High performing p-n system of $CaFe_2O_4$ coupled ZnO for synergetic degradation of Rhodamine B with white-light photocatalysis and bactericidal action. *Journal of the Taiwan Institute of Chemical Engineers* 2022; **133**, 104271.

[266] M Ahmadi, M Moslemzadeh, A Naderi, M Zehtab Salmasi, M Harati, RR Kalantary and B Kakavandi. Intensified photodegradation of nitrobenzene using ZnO-anchored spinel cobalt

ferrite: Environmental application, mechanism, and degradation pathway. *Journal of Water Process Engineering* 2022; **49**, 103064.

[267] E Suharyadi, A Muzakki, A Nofrianti, NI Istiqomah, T Kato and S Iwata. Photocatalytic activity of magnetic core-shell $CoFe_2O_4$ @ZnO nanoparticles for purification of methylene blue. *Materials Research Express* 2020; **7(8)**, 085013.

[268] T Agustina, Y Yuniar, M Faizal and P Hariani. Synthesis and characterization of $ZnO/MnFe_2O_4$ nanocomposites for degrading cationic dyes. *Journal of Ecological Engineering* 2023; **24(4)**, 252-263.

[269] FS Duarte, ALMS Melo, AB Ferro, CLPS Zanta, JLS Duarte and RMPB Oliveira. Magnetic zinc oxide/manganese ferrite composite for photodegradation of the antibiotic rifampicin. *Materials* 2022; **15(22)**, 8185.

[270] FE Yeganeh, M Yousefi, M Hekmati and M Bikhof. Photocatalytic degradation of coomassie blue G-250 by magnetic $NiFe_2O_4$/ZnO nanocomposite. *Comptes Rendus. Chimie* 2020; **23(6-7)**, 385-393.

[271] HY Zhu, R Jiang, YQ Fu, RR Li, J Yao and ST Jiang. Novel multifunctional $NiFe_2O_4$/ZnO hybrids for dye removal by adsorption, photocatalysis and magnetic separation. *Applied Surface Science* 2016; **369**, 1-10.

[272] Y Yuniar, T Mawarni, PL Hariani, M Faizal and TE Agustina. Degradation of methylene blue dye using ZnO/$NiFe_2O_4$ photocatalyst under visible light. *In*: Proceedings of the 5th FIRST T1 T2 2021 International Conference, Palembang, Indonesia. 2022.

[273] R Rahmayeni, Z Zulhadjri, Y Stiadi, A Harry and S Arief. Synthesis of ZnO/$ZnFe_2O_4$ nanocomposites in organic-free media and their photocatalytic activity under natural sunlight. *Journal of Mechanical Engineering and Sciences* 2020; **14(2)**, 6801-6810.

[274] W Wang, N Li, K Hong, H Guo, R Ding and Z Xia. Z-scheme recyclable photocatalysts based on flower-like nickel zinc ferrite nanoparticles/ZnO nanorods: Enhanced activity under UV and visible irradiation. *Journal of Alloys and Compounds* 2019; **777**, 1108-1114.

[275] M Naguib, M Kurtoglu, V Presser, J Lu, J Niu, M Heon, L Hultman, Y Gogotsi and MW Barsoum. Two-dimensional nanocrystals produced by exfoliation of Ti_3AlC_2. *Advanced Materials* 2011; **23(37)**, 4248-4253.

[276] BC Wyatt, A Rosenkranz and B Anasori. 2D MXenes: Tunable mechanical and tribological properties. *Advanced Materials* 2021; **33(17)**, 2007973.

[277] JK Im, EJ Sohn, S Kim, M Jang, A Son, KD Zoh and Y Yoon. Review of MXene-based nanocomposites for photocatalysis. *Chemosphere* 2021; **270**, 129478.

[278] SS Emmanuel, AA Adesibikan, SM Tichapondwa, MP Rayaroth, F Bosca, ML Marin, BA Samejo and G Boczkaj. MXenes as sustainable functional nanomaterials for photocatalytic degradation of dye pollutants: Performance, effect of process parameters, stability and re-useability evaluation - a critical review. *Sustainable Materials and Technologies* 2025; **46**, e01683.

[279] S Iravani and RS Varma. MXene-based photocatalysts in degradation of organic and pharmaceutical pollutants. *Molecules* 2022; **27(20)**, 6939.

[280] NH Solangi, RR Karri, SA Mazari, NM Mubarak, AS Jatoi, G Malafaia and AK Azad. MXene as emerging material for photocatalytic degradation of environmental pollutants. *Coordination Chemistry Reviews* 2023; **477**, 214965.

[281] SD Chakraborty, U Kumar, P Bhattacharya and T Mishra. Tailoring of visible to near-infrared Active 2D MXene with defect-enriched titania-based heterojunction photocatalyst for green H_2 generation. *ACS Applied Materials & Interfaces* 2024; **16(2)**, 2204-2215.

[282] J Li, Z Li, X Liu, C Li, Y Zheng, KWK Yeung, Z Cui, Y Liang, S Zhu, W Hu, Y Qi, T Zhang, X Wang and S Wu. Interfacial engineering of $Bi_2S_3/Ti_3C_2T_x$ MXene based on work function for rapid photo-excited bacteria-killing. *Nature Communications* 2021; **12(1)**, 1224.

[283] I A Alsafari, S Munir, S Zulfiqar, MS Saif, MF Warsi and M Shahid. Synthesis, characterization, photocatalytic and antibacterial properties of copper Ferrite/MXene ($CuFe_2O_4/Ti_3C_2$)

nanohybrids. *Ceramics International* 2021; **47(20)**, 28874-28883.

[284] Y Cao, Y Fang, X Lei, B Tan, X Hu, B Liu and Q Chen. Fabrication of novel $CuFe_2O_4$/MXene hierarchical heterostructures for enhanced photocatalytic degradation of sulfonamides under visible light. *Journal of Hazardous Materials* 2020; **387**, 122021.

[285] MF Taleb, T Rasheed, H A Albalwi, FIA El Fadl, MF Warsi and MM Ibrahim. Binary metal doped spinel ferrite nanoparticles and their Nano hybrid with MXene matrix to enhance catalytic properties. *Optical Materials* 2023; **145**, 114485.

[286] MA Iqbal, A Tariq, A Zaheer, S Gul, SI Ali, MZ Iqbal, D Akinwande and S Rizwan. Ti_3 C_2 - MXene/bismuth ferrite nanohybrids for efficient degradation of organic dyes and colorless pollutants. *ACS Omega* 2019; **4(24)**, 20530-20539.

[287] W Shi, Y Fu, C Hao, F Guo and Y Tang. Heterogeneous photo-Fenton process over magnetically recoverable $MnFe_2O_4$/MXene hierarchical heterostructure for boosted degradation of tetracycline. *Materials Today Communications* 2022; **33**, 104449.

[288] A Grzegórska, JC Ofoegbu, L Cervera-Gabalda, C Gómez-Polo, D Sannino and A Zielińska-Jurek. Magnetically recyclable TiO_2/MXene/$MnFe_2O_4$ photocatalyst for enhanced peroxymonosulphate-assisted photocatalytic degradation of carbamazepine and ibuprofen under simulated solar light. *Journal of Environmental Chemical Engineering* 2023; **11(5)**, 110660.

[289] T Rasheed, A Rasheed, S Munir, S Ajmal, ZM Shahzad, IA Alsafari, SA Ragab, PO Agboola and I Shakir. A cost-effective approach to synthesize $NiFe_2O_4$/MXene heterostructures for enhanced photodegradation performance and anti-bacterial activity. *Advanced Powder Technology* 2021; **32(7)**, 2248-2257.

[290] SM Lam, MK Choong, JC Sin, H Zeng, L Huang, L Hua, H Li, ZH Jaffari and KH Cho. Construction of delaminated Ti_3C_2 MXene/$NiFe_2O_4$/V_2O_5 ternary composites for expeditious pollutant degradation and bactericidal property. *Journal of Environmental Chemical Engineering* 2022; **10(5)**, 108284.

[291] FS Tehrani, R Ayoubi, M Moayedi, R Jamehbozorg, M Pourjafarabadi, M Rezavand and Y Abdi. TiO_2@$Ti_3C_2T_x$@$ZnFe_2O_4$-based long-lasting filter with photocatalytic activity. *Ceramics International* 2024; **50(15)**, 27202-27215.

[292] Q Wang, F Zhu, H Cheng, S Komarneni and J Ma. Efficient activation of persulfate by Ti_3C_2 MXene QDs modified $ZnFe_2O_4$ for the rapid degradation of tetracycline. *Chemosphere* 2023; **328**, 138546.

[293] A Enesca and L Andronic. The influence of photoactive heterostructures on the photocatalytic removal of dyes and pharmaceutical active compounds: A mini-review. *Nanomaterials* 2020; **10(9)**, 1766.

[294] X Li, Y Meng, J Li, L Zhang, B Xie, Z Ni and S Xia. The performance and mechanism of persulfate activation boosted MoO_2@LDHs Z-scheme heterojunction for efficient photocatalytic degradation of tetracycline. *Journal of Environmental Chemical Engineering* 2023; **11(3)**, 110257.

[295] L Wang, X Huang, M Han, L Lyu, T Li, Y Gao, Q Zeng and C Hu. Efficient inhibition of photogenerated electron-hole recombination through persulfate activation and dual-pathway degradation of micropollutants over iron molybdate. *Applied Catalysis B: Environmental* 2019; **257**, 117904.

[296] Y Deng, Q Che, Y Li, J Luo, X Gao, Y He, Y Liu, T Liu, X Zhao, X Hu and W Zhao. Non-radical activation of persulfate with Bi_2O_3/$BiO_{1.3}I_{0.4}$ for efficient degradation of propranolol under visible light. *Journal of Environmental Sciences* 2024; **142**, 57-68.

[297] T Fidan, R Arat and MK Bayazit. A handbook for graphitic carbon nitrides: revisiting the thermal synthesis and characterization towards experimental standardization. *Materials Research Express* 2023; **10(9)**, 095905.

[298] N Luhakhra, D Sharma, V Abbot and V Karol. *Polymers and their composites as renewable and flexible materials for boosting energy storage*. *In*: SS Kumar, P Sharma, T Kumar and V Kumar (Eds.). ACS symposium series. American Chemical Society, Washington, D. C., 2024, p. 199-221.

[299] J Joy, S Anas and S Thomas. *Graphitic carbon nitride: An uprising carbonaceous material*. *In*: S Thomas, S Anas and J Joy (Eds.). Synthesis, characterization, and applications of graphitic carbon nitride. Elsevier, Amsterdam, Netherlands, 2023, p. 1-14.

[300] P Kyriakos, E Hristoforou and GV Belessiotis. Graphitic carbon nitride (g-C3N4) in photocatalytic hydrogen production: Critical overview and recent advances. *Energies* 2024; **17(13)**, 3159.

[301] T Muhmood, I Ahmad, Z Haider, SK Haider, N Shahzadi, A Aftab, S Ahmed and F Ahmad. Graphene-like graphitic carbon nitride (g-C3N4) as a semiconductor photocatalyst: Properties, classification, and defects engineering approaches. *Materials Today Sustainability* 2024; **25**, 100633.

[302] MA Khan, S Mutahir, I Shaheen, Y Qunhui, M Bououdina and M Humayun. Recent advances over the doped g-C3N4 in photocatalysis: A review. *Coordination Chemistry Reviews* 2025; **522**, 216227.

[303] A Ajami, S Sheibani and A Ataie. S-scheme $CoFe_2O_4$/g-C_3N_4 nanocomposite with high photocatalytic activity and antibacterial capability under visible light irradiation. *Journal of Materials Research and Technology* 2024; **30**, 2168-2185.

[304] S Shenoy, C Chuaicham, T Okumura, K Sekar and K Sasaki. Simple tactic polycondensation synthesis of Z-scheme quasi-polymeric g-C_3N_4/$CaFe_2O_4$ composite for enhanced photocatalytic water depollution via p-n heterojunction. *Chemical Engineering Journal* 2023; **453**, 139758.

[305] A Ahmed, R Alabada, M Usman, AA Alothman, MK Tufail, S Mohammad and Z Ahmad. Synthesis of visible-light-responsive lanthanum-doped copper ferrite/graphitic carbon nitride composites for the photocatalytic degradation of toxic organic pollutants. *Diamond and Related Materials* 2024; **141**, 110630.

[306] J Bhatt, S Vyas, A Kumar Rai, N Madan and R Ameta. *Graphene-based photocatalysts*. *In*: PB Punjabi (Ed.). Graphene-based carbocatalysts: synthesi, properties and applications. Bentham Science Publishers, Sharjah, United Arab Emirates, 2023, p. 1-49.

[307] M Farhang, AM Ghadiri, P Hassani and AR Akbarzadeh. Highly efficient $ZnFe_2O_4$ decorated g-C_3N_4/GO with biomedical and photocatalytic activities. *Ceramics International* 2024; **50(7)**, 11716-11729.

[308] W Dai, J Mu, Z Chen, J Zhang, X Pei, W Luo and BJ Ni. Design of few-layer carbon nitride/$BiFeO_3$ composites for efficient organic pollutant photodegradation. *Environmental Research* 2022; **215**, 114190.

[309] HD Weldekirstos, T Mengist, N Belachew and M L Mekonnen. Enhanced photocatalytic degradation of methylene blue dye using fascily synthesized g-C_3N_4/$CoFe_2O_4$ composite under sun light irradiation. *Results in Chemistry* 2024; **7**, 101306.

[310] A Ali, A Ahmed, M Usman, T Raza, MS Ali, A Al-Nahari, C Liu, D Li and C Li. Synthesis of visible light responsive $Ce_{0.2}Co_{0.8}Fe_2O_4$/g-C_3N_4 composites for efficient photocatalytic degradation of rhodamine B. *Diamond and Related Materials* 2023; **133**, 109721.

[311] SS Hassan, M Javed, MN Akhtar, MA Qamar, N Ahmed, M Saeed, K Aroosh, S Khan and S Asif. The photocatalytic and antibacterial potential of highly efficient S-scheme binary S-gC_3N_4@Co-zinc ferrite nanocomposite. *Optical Materials* 2023; **142**, 114046.

[312] J Arshad, FMA Alzahrani, MF Warsi, U Younis, M Anwar, ZA Alrowaili, MS Al-Buriahi and A Manzoor. Copper substituted spinel Co-Cr spinel Ferrites@Graphitic carbon nitride nanocomposite as a visible light active photocatalytic material. *Optical Materials* 2024; **148**, 114906.

[313] L Wang, X Ma, G Huang, R Lian, J Huang, H She and Q Wang. Construction of ternary CuO/$CuFe_2O_4$/g-C_3N_4 composite and its enhanced photocatalytic degradation of tetracycline hydrochloride with persulfate under simulated sunlight. *Journal of Environmental Sciences* 2022; **112**, 59-70.

[314] B Basha, A Murtaza, SI Shamsah, MS Alqahtani, A Manzoor, ZA Alrowaili, S Munir, MI Din and MS Al-Buriahi. The impact of cu-doping on $Ni_{0.5}$-$Co_{0.5}Fe_2O_4$ @graphitic carbon nitride for the

degradation of organic pollutants. *FlatChem* 2023; **41**, 100546.

[315] S Ziaalmolki, B Aslibeiki, M Zarei, R Torkamani and T Sarkar. Enhanced visible-light-driven photocatalysis via magnetic nanocomposites: A comparative study of g-C_3N_4, g-C_3N_4/Fe_3O_4, and g-C_3N_4/Fe_3O_4/ZnO. *Materials Today Communications* 2023; **37**, 107340.

[316] N Masunga, BB Mamba and KK Kefeni. Magnetically separable samarium doped copper ferrite-graphitic carbon nitride nanocomposite for photodegradation of dyes and pharmaceuticals under visible light irradiation. *Journal of Water Process Engineering* 2022; **48**, 102898.

[317] Q Hou, M Wang, T Li, Y Hou, K Xuan and Y Hao. Peroxymonosulfate-assisted photocatalysis by a novel Ti_3C_2-based heterojunction catalyst (g-C_3N_4/Ti_3C_2/$MnFe_2O_4$) for enhanced degradation of naphthalene. *Chemical Engineering Journal* 2023; **464**, 142566.

[318] F Wen, Y Li, X Huang, L Pang, T Zhang and Y Xu. Utilizing three-dimensional ordered macroporous $NiFe_2O_4$ loaded with g-C3N4 as a heterogeneous photo-Fenton catalyst for tetracycline degradation. *Journal of Alloys and Compounds* 2023; **958**, 170403.

[319] A Adewuyi and RA Oderinde. Photocatalytic removal of some selected antibiotics in polluted water system by graphitic carbon nitride-enhanced vanadium ferrite (VFe_2O_4@g-C_3N_4). *Chemosphere* 2024; **362**, 142733.

[320] R Kumar, A Sudhaik, Sonu, P Raizada, VH Nguyen, QV Le, T Ahamad, S Thakur, CM Hussain and P Singh. Integrating K and P co-doped g-C3N4 with ZnFe2O4 and graphene oxide for S-scheme-based enhanced adsorption coupled photocatalytic real wastewater treatment. *Chemosphere* 2023; **337**, 139267.